Surface Studies of Porous Materials Using Solid-state NMR and DNP-SENS

Bharti Kumari

Darmstadt 2019

TECHNISCHE
UNIVERSITÄT
DARMSTADT

Surface Studies of Porous Materials Using Solid-state NMR and DNP-SENS

vom Fachbereich Chemie
der Technischen Universität Darmstadt

zur Erlangung des Grades

Doctor rerum naturalium
(Dr. rer. nat.)

Dissertation

von

Bharti Kumari

Erstgutachter : Prof. Dr. Gerd Buntkowsky
Zweitgutachter : PD Dr. Torsten Gutmann

Darmstadt 2019

Tag der Einreichnung :10.10.2019

Tag der mündlichen Prüfung :25.11.2019

Surface Studies of Porous Materials Using Solid-state NMR and DNP-SENS

by

Bharti Kumari

A dissertation submitted to the
Department of chemistry to obtain the academic degree of

Doctor rerum naturalium
(Dr. rer. nat.)

Technische Universität Darmstadt
Darmstadt, Germany
Oct 2019

Declaration

The work presented in this dissertation has been carried out by me under the guidance of Prof. Dr. Gerd Buntkowsky, PD Dr. Torsten Gutmann and Dr. Hergen Breitzke during the period from May 2016 to October 2019 at Technische Universität Darmstadt, Germany.
This work has not been submitted in part or in full for a degree, a diploma, or a fellowship to any other university or institute. Whenever contributions of collaborators are involved, every effort is made to indicate this clearly. This thesis is a bonafide record of original work done by me and all sources listed within have been detailed in the bibliography. The research conducted during this thesis resulted in four published articles in peer-reviewed international journals (the order is maintained according to chapters). Chapters 4, 5, 6 and 7 of this thesis, summarize the following articles.

1. **B. Kumari**, M. Brodrecht, H. Breitzke, M. Werner, B. Grünberg, H.-H. Limbach, S. Forg, E. P. Sanjon, B. Drossel, T. Gutmann and G. Buntkowsky, *The Journal of Physical Chemistry C*, **2018**, 122, 19540-19550.

2. **B. Kumari**, M. Brodrecht, T. Gutmann, H. Breitzke and G. Buntkowsky, *Appl. Magn. Reson.*, **2019**, DOI: 10.1007/s00723-019-01156-2

3. **B. Kumari**, D. John, P. Hoffmann, A. Spende, E. Toimil-Molares Maria, C. Trautmann, C. Hess, P. Ruff, M. Schulze, R. Stark, G. Buntkowsky, A. Andrieu-Brunsen and T. Gutmann, Zeitschrift für Physikalische Chemie, **2018**, 232, 1173.

4. T. Gutmann, **B. Kumari**, L. Zhao, H. Breitzke, S. Schöttner, C. Rüttiger and M. Gallei, *The Journal of Physical Chemistry C*, **2017**, **121**, 3896-3903.

Acknowledgment

I owe my sincere gratitude to my PhD supervisor, Prof. Dr. Gerd Buntkowsky, who gave me the opportunity to work in his group, which has a well-equipped laboratory with various NMR spectrometers. I would like to thank him for his unconditional support, motivational leadership and immense knowledge of NMR topics that steered me in the right direction throughout my PhD. His kind and understanding attitude towards my flexible working hours always kept me motivated to give my best not only on research front but also in my personal life.

Secondly, I would like to thank my thesis co-supervisor, PD Dr. Torsten Gutmann. He provided me with the necessary training on DNP-NMR, acquainted me with scientific software such as MNova, Origin and taught me the easily overlooked subtleties of writing an impactful research paper. Apart from helping me professionally, he has also graciously offered his assistance on personal front. One such incidence is when he generously came with me to visa office and helped me with the paperwork. He has supported me and bolstered my confidence in hard times. He is an energetic and dedicated person to work with and I find myself short on words to describe his helpful and encouraging behavior at the workplace. So, thank you Torsten, this thesis would not have been possible without you.

Now, I would like to thank Dr. Hergen Breitzke, for his unconditional tech-support to deal with technical difficulties, his patience to teach me how to use vacuum pump equipment on multiple occasions. I acknowledge and appreciate his innovative idea of referencing the 2D FSLG CPMAS HETCOR experiments; the project wouldn't have concluded without him. His theoretical knowledge on solid-state NMR always gave me a clear-cut solution to my conceptual queries related to the pulse programming and quantum mechanics. And lastly, I would like to thank him for his after-office-hours guitar lessons to relieve stress and for understanding the underlying humor when I correlated the magnetic resonance with guitar's tuning resonance.

I would like to thank our collaborators to conduct various measurements and provide valuable information. I am thankful to Dr. Elvira Pfong, a former PhD student from Prof. Dr. Barbara Drossel's group, who performed the molecular dynamics simulations for one of our leading projects. A sincere thanks to Dr. Marcus Gallei's and his group, Prof. Dr. Annette Andrieu-Brunsen and her group, Prof. Dr. Christina Trautmann and her group and Prof. Dr. Robert Stark and his group to provide us full assistance for sample and various data while working on the side projects on ion etched PC membrane and cellulose paper substrate.

I thank the Buntkowsky group for their scientific, technical and personal support. I would like to thank Monica, Lorentz and Nadia for making the office friendlier, to Dr. Martin Brodrecht

and Dr. Mayke Werner for providing me with silica material SBA-15 and to Sarah Bothe for her co-operative nature while working on DNP. I thank Sara Hadjiali and Dr. Vytautas Klimavičius for helping me at multiple occasions and lastly Dr. Jiquan Li, a former post-doc in the group, who helped me with the on-boarding in May 2016.

Many thanks to my friends in Germany and in India, they made my journey enjoyable even in hard and frustrating phases, to Kranti, Shweta and Muskan who was just a call away for any sort of consultations and for their encouragement and the appreciation.

I reserve my special thanks to Dr. Sampat Kumar Sharma, for his efforts and moral support. It would have been difficult for me to arrive at this stage; his enthusiasm did not let me lose the hope. Any amount I appreciate his motivation and dedication, it is not enough. Thank you for everything.

I would like to express my gratitude towards my family and my fiancé's family. It would have not been possible without their support and understanding. I thank to my parents and my mother-in-law for their strong support and blessings and to my dear sister Sarita, who never stopped believing in me and kept me motivated.

Finally, I thank Puneet Arora, my fiancé, for filling my life with positive momentum, for teaching me a great deal of patience and for being a constant support in my life. Thank for so much love and care.

There are many people who helped me to arrive at this milestone, I may have forgotten some names, but they always have place in my heart.

Zussamenfassung

In dieser Arbeit wurden Festkörper-NMR-Techniken, die teilweise mit DNP kombiniert wurden, genutzt, um Oberflächenwechselwirkungen mit Gastmolekülen sowie die Oberflächenfunktionalisierung verschiedener poröser Materialien zu untersuchen. Dazu standen drei Arten von Materialien: (i) mesoporöses Siliciumdioxid SBA-15, (ii) ionengeätzte Polycarbonatmembranen und (iii) komplexe Cellulosepapiersubstrate, zur Verfügung.

Für mesoporöses Siliciumdioxid wird die detaillierte Untersuchung der Wechselwirkungen von Wasser und Octanol-1-Molekülen mit der Porenoberfläche von Siliciumdioxid SBA-15 vorgestellt. Hierzu wurden 1D- und 2D-Festkörper-NMR-Techniken bei Raumtemperatur verwendet. Die lokalen Wechselwirkungen zwischen Oberfläche und Gastmolekülen (Octanol-1 und Wasser) wurden mittels ^{1}H-^{29}Si FSLG-CPMAS-HETCOR-Experimenten untersucht. Während der Arbeit an FSLG-CPMAS-HETCOR-Experimenten ergab sich ein Referenzierungsproblem für die indirekte Protonendimension. Zur Lösung dieses Problems wurde eine neue Referenzierungstechnik unter Verwendung einer 2D ^{1}H-^{1}H MAS FSLG-Pulssequenz entwickelt, welche eine eindeutige Referenzierung der indirekten Dimension der FSLG-HETCOR-Spektren ermöglicht.

Desweiteren wurden auch komplexe Materialien untersucht, z. B. geätzte Ionenkanälen enthaltende Polycarbonatfolien sowie Cellulosepapiersubstrate. Da diese Materialien eine geringe spezifische Oberfläche aufweisen, war es erforderlich DNP-Techniken zu verwenden. Die Charakterisierung der Porenoberfläche einer Siliciumdioxid beschichteten, ionengeätzten PC-Membran erfolgte entsprechend mittels der DNP-SENS-Technik.

Desweiteren wurden funktionalisierte Papiersubstrate mit DNP-SENS-Techniken und unterschiedlichen Arten von Radikalmatrizen untersucht, um einen Zusammenhang zwischen Polarisationsmatrix und erreichbarer Signalverstärkung in den Spektren zu bestimmen

Table of Content

1. Introduction

1.1. Motivation

For several decades, porous materials are known for applications in industrial use, for example in catalysis, filtration processes, gas and heat storage, gas sensing, ion exchange, oil recovery and drug delivery [1-5]. Furthermore, porous materials have gathered significant attention in scientific communities due to their unique property of possessing high surface areas, which makes them high index performance materials in electrical usage, heat insulation, thermal conductivity and sound absorption [6-9]. In recent years, porous materials have been also utilized as model systems to investigate the effect of confinement on small molecules or as model systems for nanochannels in membranes [10-12]. For the practical applications of such materials, it is important to understand their physical and chemical properties, which are hidden in their molecular geometry and can be understood by detailed investigation at a molecular level. Understanding these properties help in tailoring a rational design for industrial applications and also give information about the optimization of such systems to be used in the fields of advanced technologies, such as printed electronics, capacitor design, and sensors [13-17]. In the past, various methods have been proposed for structure determination (X-ray, electron microscopy to name a few) and surface sensitive techniques (Atomic Force Microscopy and Scanning Electron Microscopy) [18-20] are known, however, they only led to partial information and the key questions like, local interactions, dynamics and molecular alignment remain unanswered. Therefore, in this thesis, we focus on Solid-state NMR spectroscopy, which provides detailed information on the molecular structure and surface morphology of porous materials [21-23]. In addition, NMR spectroscopy also sheds light on dynamics and interactions of molecules in confinement, which is utilized in this work to study guest-host systems consisting of porous silica filled with mixtures of alcohol and water [24]. However, solid-state NMR suffers from intrinsically low sensitivity, which is significantly important in case of materials containing small surface areas. One possibility to overcome sensitivity issues in solid-state NMR experiments is the combination with Dynamic Nuclear Polarisation (DNP), which has emerged as a robust method to analyse surface species on porous materials [25-29]. This technique is utilized in this work to study materials having low surface area such as polycarbonate foil [30] and cellulose paper [31].

1.2. Contribution

In this thesis, three types of porous materials (i) mesoporous silica, (ii) ion etched polycarbonate foils and (iii) complex cellulose substrates (shown in Figure 1.1 a, b and c respectively) are investigated by solid-state NMR and DNP combined solid-state NMR, as each of these materials has a different application background.

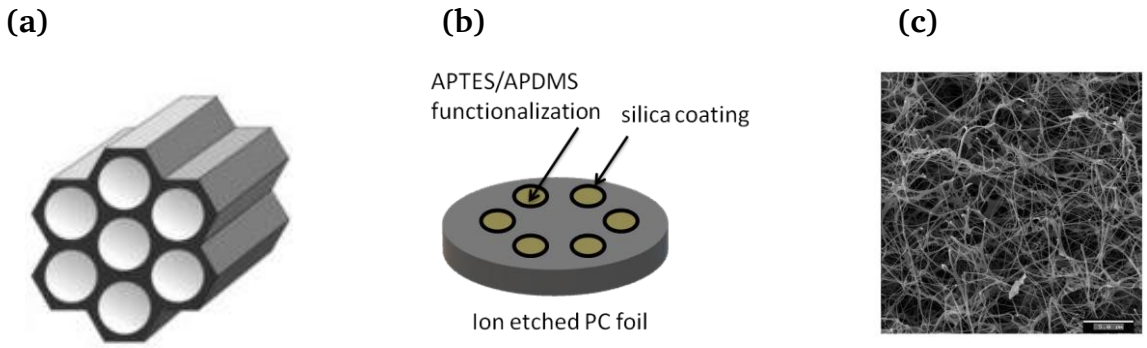

Figure 1.1 Porous materials investigated in this thesis: (a) mesoporous SBA-15, reprinted (adapted) with permission from ref [32], (b) ion etched Poly carbonate foil functionalized with linker, (c) complex cellulose substrate, reprinted (adapted) with permission from ref [33].

The core contributions of this thesis can be assessed as following:

i) For mesoporous silica:
   a. Understanding the interactions of water and octanol molecules with the pore surface of the silica.
   b. Inspecting the orientation/assembly of octanol-1 and water molecules in the confinement of mesoporous silica.
   c. Validating that interactions between alcohol-water and mesoporous silica depend on liquid-liquid or liquid-surface interactions, finding out if they are driven by the hydrophobic/hydrophilic nature of molecules in the system.
   d. Highlighting the problem in referencing the indirect dimension of FSLG CPMAS HETCOR spectra and proposing a novel solution to overcome this problem.

ii) For ion-etched poly carbonate foils:
   a. Demonstrating the feasibility of DNP-SENS technique for SiO_2 coated polycarbonate membranes to characterize the pore surface.
   b. Verifying the functionalization on the inner surface of ion etched poly carbonate foils having small specific surface area. ($<<30\ m^2/g$).

iii) For cellulose paper substrate:

a. Asserting the possibility to detect the surface functionalization on cellulose paper substrate that contain small surface area (<<30 m^2/g).
b. Exploiting the dependence of the signal enhancement on the employed polarization source (radical/solvent mixture)

Several smaller contributions of this thesis include (i) identifying sensitivity of the ^{1}H and ^{29}Si chemical shift of mesoporous silica on addition of water and explaining the reason behind, (ii) understanding the impact of varying the ratio of water and three different alcohols on our experiments with mesoporous silica, (iii) discussing the role of hydrogen bonds for molecular interactions in alcohol-mesoporous silica environment.

1.3. Structure of this Thesis

This thesis consists of nine chapters. The first chapter proposes the motivation for this work along with the criteria for evaluation of this thesis. The second and third chapters explain the fundamentals of solid-state NMR and DNP. Chapter four discusses in detail about advanced solid-state NMR studies on octanol-1/water in mesoporous silica material and presents the findings from 2D FSLG CPMAS HETCOR experiments. Chapter five gives a detailed analysis of the referencing issue obtained in FSLG CPMAS HETCOR experiments and provides a novel solution for this problem. Chapter six focuses on surface enhanced DNP solid-state NMR studies of the functionalization of etched ion-track polycarbonate membranes. Chapter seven discusses the study of surface functionalized paper materials using DNP-NMR. Chapter eight concludes this thesis by providing the summary and discussing the points from check list, which are set as thesis goals in section 1.2 along with future perspectives of this work. Finally, the appendix provides ll supporting data (spectra, experimental data etc.) used in this thesis.

2. Nuclear Magnetic Resonance

It is imperative for a reader of this thesis to have basic knowledge of Nuclear Magnetic Resonance (NMR) for understanding the fundamental concepts and methodologies employed in this thesis. Hence, this chapter provides a selective introduction to the NMR concepts. However, detailed quantum mechanical description of the NMR spectroscopy is consciously left out of this explanation. Interested readers are encouraged to go through the excellent text books by Levitt and Keeler [34, 35].

2.1. Introduction

The magnetic resonance phenomenon was first described by Isidor Rabi in 1938 using a Stern-Gerlach experiment [36] in molecular beams, for which Isidor Rabi was later awarded the Nobel Prize in physics [37]. During the World War II, Edward Mills Purcell, working on the development of the radar in radiation laboratory at Massachusetts Institute of Technology (MIT), discovered the absorption of radio frequency waves by matter, which was the basis for NMR in bulk matter [38]. In 1946, Edward Mills Purcell and Felix Bloch independently used this idea to demonstrate NMR on solids and liquids. For their work they received the Nobel prize in physics in 1952 [39]. Starting from these pioneering works, NMR evolved into an extremely powerful technique which is nowadays used in biomolecular studies, materials characterization and magnetic resonance imaging (MRI) in medical diagnostics.

NMR spectroscopy is a technique to determine the structure of materials, bio-molecules, and to investigate the physical and chemical properties in solids and solutions. In detail, NMR is based on the spin, a very intrinsic property of the nuclei, which by convention is denoted as I. The spin of the nucleus indicates that the atomic nucleus 'behaves' like a tiny, magnetic gyroscope. The spin of the nucleus also decides if the nucleus is NMR active (I= integer or half-integer) or NMR inactive (I=0). The value of I can be empirically deduced according to the method described in Figure 2.1. The concept of NMR is about the absorption of radio-frequency waves by nuclei spins in the presence of an external magnetic field. When a nucleus with spin $I \neq 0$ is placed in a magnetic field, it is able to absorb at a specific radio frequency (RF) and responds by creating an electromagnetic signal. This phenomenon is called resonance, since the radio frequency has to match the frequency of the precision of the nuclear spin (also known as Larmor frequency) in the external magnetic field. Different nuclei exhibit different resonance frequencies.

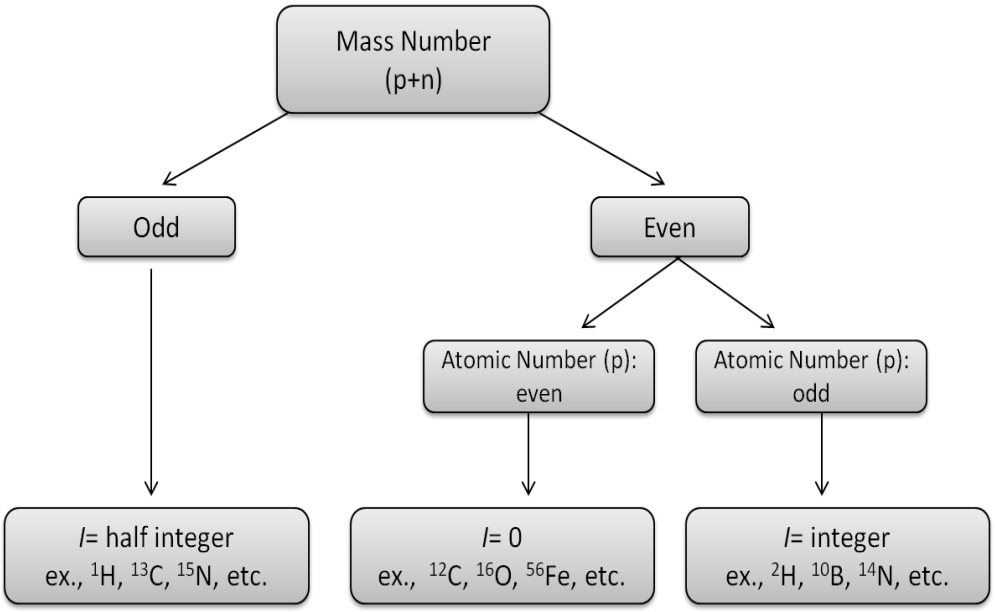

Figure 2.1 Method to deduce the spin quantum number *I* of the various atoms. Adapted from ref [40].

2.2. The Electromagnetic Field

As described above, the spin of NMR active nuclei behaves as a tiny, magnetic gyroscope. This means, when NMR active nuclei are placed in a magnetic field, the spin has the intrinsic capability to interact with the field. The interaction between the nuclear spin and the magnetic field is called Zeeman-effect. The Zeeman-effect degenerates the energy levels in an external magnetic, which decides the sensitivity of the NMR signal. The Zeeman-effect is explained in the next section. The sensitivity of a NMR experiment significantly depends on the gyromagnetic ratio and natural abundance of the nuclei of interest, namely as higher the gyromagnetic ratio and natural abundance, the higher the sensitivity. In Table 2.1, the spin quantum number, the gyromagnetic ratio and natural abundance of some commonly used nuclei are given.

Table 2.1 List of some common nuclei used in NMR and their spin quantum number, gyromagnetic ratio and natural abundances. For comparison, the electron spin is also listed in the last row of this table. The values in the table are collected from various sources [34, 35] and combined together for convenience of the reader.

Nucleus	**Spin (*I*)**	**Gyromagnetic Ratio (γ) [10^6 rad.s^{-1}.T^{-1}]**	**Natural Abundance [%]**
^{1}H	1/2	267.513	99.98
^{2}H	1	41.065	0.02
^{13}C	1/2	67.262	1.10
^{14}N	1	19.34	99.63
^{15}N	1/2	-27.116	0.37
^{17}O	5/2	-36.28	0.037
^{19}F	1/2	251.8	100
^{23}Na	3/2	70.81	100
^{31}P	1/2	108.39	100
^{113}Cd	1/2	-59.61	12.22
e-	1/2	176086	[-]

2.3. Nuclear Zeeman Splitting

In an external magnetic field B_0, depending on the spin I, the energy level of a nucleus is split into different energy levels as per $(2I+1)$ rule. This effect is illustrated in Figure 2.2, which shows the degeneracy of energy levels in the absence of an external magnetic field ($B_0=0$) for a spin $I=1/2$ system, which splits up in two different energy levels in presence of an external magnetic field ($B_0 \neq 0$). Such phenomenon obtained for nuclear spins is called Nuclear Zeeman splitting. The splitting is directly proportional to the external magnetic field B_0, where the proportionality constant is the magnetic moment (μ).

$$E_{mag} = -\mu B_0 \tag{2.1}$$

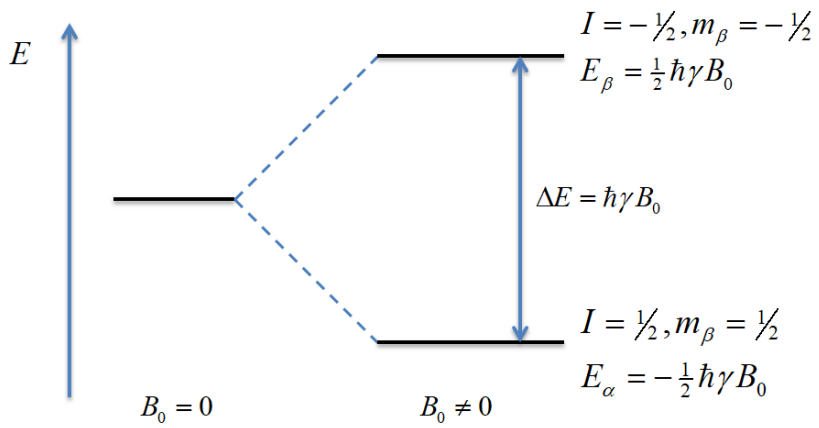

Figure 2.2 The energy level diagram to demonstrate the nuclear Zeeman splitting of a spin ½ nucleus, which in the presence of a magnetic field splits up in two energy levels.

The energy required for a spin to flip from one energy state to another is the energy difference between the two states and can be calculated from equation (2.2) .

$$\begin{aligned}\Delta E &= E_\beta - E_\alpha \\ &= \tfrac{1}{2}\hbar\gamma B_0 - (-\tfrac{1}{2}\hbar\gamma B_0) \\ &= \hbar\gamma \mathrm{B}_0\end{aligned} \tag{2.2}$$

Using Planck's equation,

$$\Delta E = h\omega_0 = \frac{h}{2\pi}\gamma B_0$$

$$\Rightarrow \omega_0 = \frac{\gamma B_0}{2\pi} \tag{2.3}$$

.

Here, ω_0 defines the Larmor frequency, h is the Planck's constant and $\hbar$ is the reduced Planck's constant.

2.4. Spin Precession or Larmor Frequency

The Larmor frequency of the nuclear spin around a magnetic field B_0 is given by the Larmor equation (2.4).

$$\omega = \gamma B_0 \tag{2.4}$$

All NMR active nuclei possess a magnetic moment and when they are placed in a magnetic field, they are aligned with the magnetic field at a certain angle. This alignment of the

magnetic moment vector with the external magnetic field produces a spinning, commonly known as precession of the spin around the main (static) magnetic field. In classical physics, this precession of the spin is analogous to the spinning of a magnetic gyroscope but in reality, the concept of spin precession has to be explained by quantum mechanics which is beyond the scope of this work.

2.5. Boltzmann Distribution

According to the Boltzmann distribution, the population of the spin states can be described by equation (2.5).

$$\frac{N_\alpha}{N_\beta} = e^{-\left(\frac{\Delta E}{k_b T}\right)} \tag{2.5}$$

The population difference between the two states α and β depends on the strength of the external magnetic field and the temperature, which are determining factors for the sensitivity of NMR. The sensitivity of NMR is related to the polarization P of spin states which is defined by equation (2.6).

$$P = \frac{n_\alpha - n_\beta}{n_\alpha + n_\beta} = \tanh\left(\frac{\gamma \hbar B_0}{2 k_b T}\right) \tag{2.6}$$

From this equation it is obtained, that sensitivity enhancement can be achieved by either increasing the magnetic field B_0, by lowering the temperature T or by increasing the number of spins in the sample. Other than these three parameters, the polarization can also be improved by employing a system having higher gyromagnetic ratio γ. The latter one is discussed more in detail in the chapter on Dynamic Nuclear Polarization (DNP), which can be used as a powerful method to achieve higher sensitivity in NMR experiments.

2.6. Solid-state NMR

Solid-state NMR in comparison to solution-state NMR is more complex due to the fact that it comprises of orientation-dependent interactions, which are not averaged out by the rapid molecular tumbling motions like in solution-state NMR. Therefore, the signals in spectra of nuclei with spin $I = 1/2$ are broadened by dipolar couplings and chemical shift anisotropy

(CSA). Due to this broadening effect the valuable information from the solid-state NMR spectra is obscured. In order to achieve high resolution solid-state NMR spectra, various techniques have been invented, for example, Magic Angle Spinning (MAS), high power decoupling schemes, and various 1D and 2D experiments. In the following, we will explain each of these techniques to understand how they improve the resolution of solid-state spectra.

2.6.1. Magic Angle Spinning

As discussed above, the sharp resonance peaks in solution-state NMR are the result of the molecules rapid tumbling motion, which averages the anisotropic interactions and successfully removes them from the spectrum. However, solid-state NMR on comparison with solution-state NMR provided a broad spectrum, hence; it became necessary to come up with an idea to avoid the effects from anisotropic interactions and dipolar couplings in solids. The considerable difference between solid and solution NMR spectra led to fast development in the direction of solid-state high-resolution NMR. In 1958-59 E. R. Andrew and I. J. Lowe, experimentally and theoretically figured out the way to remove the dipolar couplings in solids, by coming up with the idea of MAS [41-44]. The effect of MAS on solid is shown in Figure 2.3.

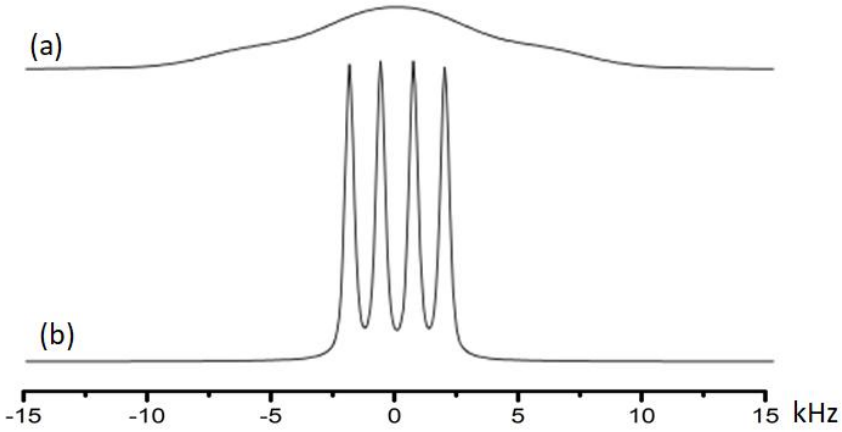

Figure 2.3 Comparison of ^{19}F spectra of polycrystalline $KAsF_6$: (a) static NMR, (b) MAS under 5.5 kHz. Adapted from ref [44].

To understand the MAS in details, it is better to look on the quantum mechanical expression by nuclear-spin Hamiltonians used in solid-state NMR, which is shown in equation (2.7).

$$\hat{H} = \hat{H}_{ext} + \hat{H}_{\text{int}} \tag{2.7}$$

Here, $\hat{H}_{ext}$ can be expressed in terms of a Hamiltonian for Zeeman interactions and a Hamiltonian for the interaction with the time dependent radio frequency field B_1.

$$\hat{H}_{ext} = \hat{H}_Z + \hat{H}_{RF} \tag{2.8}$$

The expression for $\hat{H}_{\text{int}}$ is given by the sum of the chemical shift anisotropy Hamiltonian ($\hat{H}_{CS}$), direct spin-spin interactions (known as dipolar coupling, $\hat{H}_D$), indirect spin-spin interactions ($\hat{H}_J$) and quadrupolar interactions ($\hat{H}_Q$) and is shown in equation (2.8).

$$\hat{H}_{\text{int}} = \hat{H}_{CS} + \hat{H}_D + \hat{H}_J + \hat{H}_Q \tag{2.9}$$

To simplify $\hat{H}_{\text{int}}$ only the chemical shift anisotropy Hamiltonian ($\hat{H}_{CS}$) and the dipolar coupling Hamiltonian ($\hat{H}_D$) are considered in the following.

$$\begin{aligned} \hat{H}_{\text{int}} &= \hat{H}_{CS} + \hat{H}_D \\ &= \hat{H}_{CS} + \hat{H}_{II} + \hat{H}_{IS} \end{aligned} \tag{2.10}$$

The Hamiltonian for dipolar coupling can be split into two separate Hamiltonians; one for homonuclear coupling ($\hat{H}_{II}$) and another for Heteronuclear couplings ($\hat{H}_{IS}$) where I is used for ^{1}H and S is used for X nuclei like ^{13}C or ^{15}N. The expressions of these Hamiltonians are described in equation (2.11).

$$\begin{aligned} \hat{H}_{CS} &= \gamma B_0 \hat{I}_Z [\frac{1}{2}(3cos^2\theta - 1)\delta_{CSA}] \\ \hat{H}_{II} &= -D\frac{1}{2}(3cos^2\theta - 1)[3\hat{I}_Z\hat{S}_Z - \hat{I}\cdot\hat{S}] \\ \hat{H}_{IS} &= -D\frac{1}{2}(3cos^2\theta - 1)[2\hat{I}_Z\hat{S}_Z] \end{aligned} \tag{2.11}$$

The D in equation (2.11) is known as dipolar coupling constant, which can be expressed as $\frac{-\mu_0\gamma_1\gamma_2 h^2}{16\pi^3 r^3}$ in units of Hz. According to the expression given in equation (2.11), it can be

concluded that if the rotor is spun at an angle of $\theta = 54.74$ with respect to the static magnetic field B_0, then on average the term $(3cos^2\theta - 1)$ will turn to 0, which leads to averaging out of the dipolar couplings. Since, the CSA possess the same angular dependency, it will be also reduced to zero, on average. This technique is called magic angle spinning (MAS), which results into narrower peaks, hence improving the spectral resolution.

Despite the fact that MAS averages the dipolar interactions, the averaging is not very effective at low spinning rate (5-8 kHz) compared to very strong dipolar interactions (100 kHz) in case of ^{1}H-^{1}H or ^{19}F-^{19}F. As a result, the signals are broadened by dipolar coupling even in the presence of MAS, thus additional decoupling sources are required in order to achieve the narrower peak. For homonuclear dipolar couplings, it is overcome by employing the Frequency Switched Lee Goldberg (FSLG) [45] decoupling scheme. Heteronuclear dipolar interactions can be addressed by applying high power decoupling schemes, such as TPPM [46], SPINAL [47], etc. In addition, the high-power decoupling also averages out the J-couplings, which are not averaged out by MAS. Thus, the combination of MAS and decoupling schemes averages the dipolar interactions and thus provide a higher resolved spectrum.

2.7. Routinely used Solid-state NMR experiments

In the past, plenty of solid-state NMR techniques have been introduced specifically to address different requirements of systems under study. In this thesis, for determination of structure and interactions, we used 1D Cross Polarization Magic Angle Spinning (CPMAS) and 2D Frequency Switched Lee Goldberg Cross Polarization Magic Angle Spinning Heteronuclear Correlation (FSLG CPMAS HETCOR). Both of these techniques are explained in detail in the subsequent sections.

2.7.1. Cross Polarization

In 1962, S. R. Hartmann and E. L. Hahn described nuclear double resonance in rotating frame [48] in the case of static NMR, which later named as Cross Polarization (CP). Cross polarization is helpful to measure nuclei having low natural abundance and low gyromagnetic ratio (γ) such as ^{13}C or ^{15}N or ^{29}Si. The idea of cross polarization is based on polarization transfer from sensitive nuclei such as ^{1}H or ^{19}F to comparatively low sensitive nuclei (X) such as ^{13}C, ^{15}N or ^{29}Si through dipolar interactions between ^{1}H and X. The original idea of cross polarization can be described by the scheme shown in Figure 2.4.

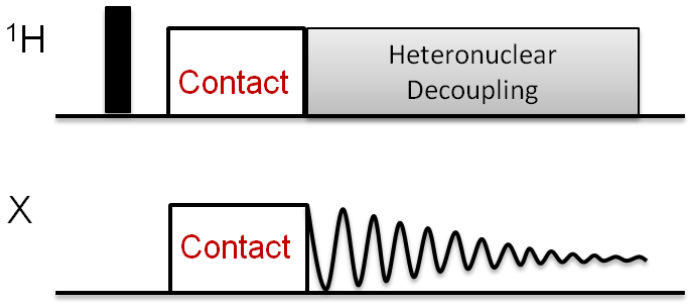

Figure 2.4 The cross-polarization pulse sequence to transfer magnetization from the abundant nuclei ^{1}H to dilute spins X via dipolar coupling. Adapted from ref [48].

In the first step, a 90° pulse is applied to ^{1}H which flips the ^{1}H magnetization in the xy plane, afterwards, a contact pulse is applied to transfer the magnetization from ^{1}H to X. The field on ^{1}H is known as spin-lock field and can be denoted as $B_1(^1H)$. At the same time, a contact pulse on channel X is applied in a similar manner to build up the X-magnetization in the xy plane. The field on X nuclei is denoted by $B_1(X)$. In order to achieve the cross polarization, the condition given in equation (2.12) must be matched. This condition is practically achieved by setting the amplitude value for one channel (^{1}H) and optimizing the value for the amplitude of the second channel (X) until the maximum signal is achieved.

$$\gamma_H B_1(^1H) = \gamma_X B_1(X) \quad (2.12)$$
$$\Rightarrow \omega_H = \omega_X$$

2.7.2.Cross Polarization under Magic Angle Spinning (CPMAS)

In our thesis we use a variant of cross polarization technique, which is also widely used in NMR community called cross polarization under MAS [49]. The combination of cross polarization and MAS techniques, prima facie, contradicts our previous discussion and hence, cross polarization when combined with MAS should not efficiently work since MAS averages out the dipolar coupling. However, a more detailed look on the time dependency of the dipolar interactions under MAS reveals an oscillatory modulation of the dipolar interactions with the spinning frequency, leading to an amplitude and frequency modulation of the polarization transfer process, splitting the Hartmann-Hahn condition into sidebands with center band suppression. The matching condition for cross polarization under MAS can be given by a modified Hartmann-Hahn equation[48], where the sum/difference between the Larmor frequency of two nuclei is equal to a multiple of the magic angle spinning rate, as shown in equation (2.13).

$$\omega_I \pm \omega_S = n\omega_r \tag{2.13}$$

Here, ω_I is the Larmor frequency of ^{1}H, ω_S is the Larmor frequency of the heteronucleus (X) and ω_r is the magic angle spinning rate. This means that a recalibration of the Hartmann-Hahn condition after changing the spinning frequency is required. Furthermore, there exist a set of Hartmann-Hahn conditions for each MAS spinning frequency. In order to avoid it, a new pulse sequence called ramped-CP was derived [50], which is depicted in Figure 2.5.

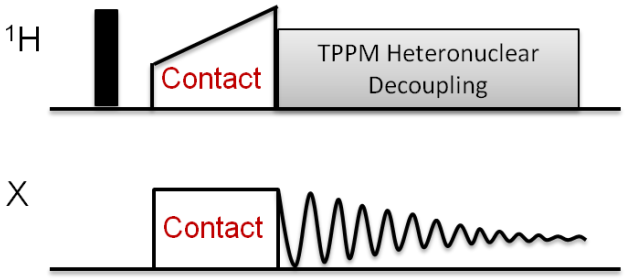

Figure 2.5 The pulse sequence of the ^{1}H-X Cross Polarization experiment under Magic Angle Spinning (CPMAS) used in solid-state NMR or DNP-NMR. Adapted from ref [50].

The first 90° turn the ^{1}H magnetization in xy plane as described in the previous section for cross polarization under static conditions. The contact pulse for either ^{1}H or X, however, is made variable in amplitude, in practice about 50 %. When the Hartmann-Hahn conditions are achieved, the contact pulse allows the polarization transfer from ^{1}H to X (^{13}C/^{15}N/^{29}Si) via dipolar coupling. Since, the variable B_1 field will run through the split Hartmann-Hahn matching conditions under MAS, the variable amplitude CPMAS sequence is insensitive to spinning rate changes in a wide range. In the final step, heteronuclear decoupling is applied to decouple protons, which provides high resolved spectra. Further details on the theory of CPMAS can be found in books on solid-state NMR as for example by Melinda J. Duer[51].

2.7.3.FSLG CPMAS HETCOR

HETCOR experiments play an important role in determining the interactions of small molecules with the surface of porous materials by providing for example the correlation between ^{1}H and a nucleus X [52, 53]. The pulse program of a FSLG CPMAS HETCOR [45, 54, 55] experiment is shown in Figure 2.6, which is similar to the CPMAS experiment except the FSLG part, therefore to understand the FSLG CPMAS HETCOR experiment, it is needed to understand FSLG (Frequency Switched Lee Goldberg) and CPMAS. The CPMAS has already

been explained in the previous section. The FSLG part is the key step of this experiment as it is accountable for the resolution in the spectra. As we discussed in section 2.6.1, the MAS averages out the dipolar coupling, but at moderate spinning rate (in case of proton homonuclear coupling, the spinning rate (8-10 kHz) is lower than the homonuclear dipolar interaction, 100 kHz), it is not sufficient to average out the couplings. Therefore, a combination of MAS and multiple pulse decoupling scheme (in our case FSLG) is applied to solve the problem. The pulse sequence as shown in Figure 2.6 consists of a 90° pulse to turn the magnetization in xy plane. Afterwards, a 54.7° pulse (pul54) is applied to align the z-component of the ^{1}H spin system in the direction of the magic angle, where it is subjected to FSLG decoupling to precess about an effective field oriented at the magic angle. The combination of MAS and FSLG removes the homonuclear dipolar coupling as described, while the heteronuclear dipolar couplings are averaged out by the combination of MAS and high power decoupling as described in section 2.6.1. During this process, the ^{1}H chemical shifts evolve and in the next step, again the pul54 is applied with opposite phase to return the magnetization into the xy plane and then the cross polarization is used to transfer the proton magnetization to nuclei X. The detection takes place on the X channel, while ^{1}H heteronuclear decoupling is applied.

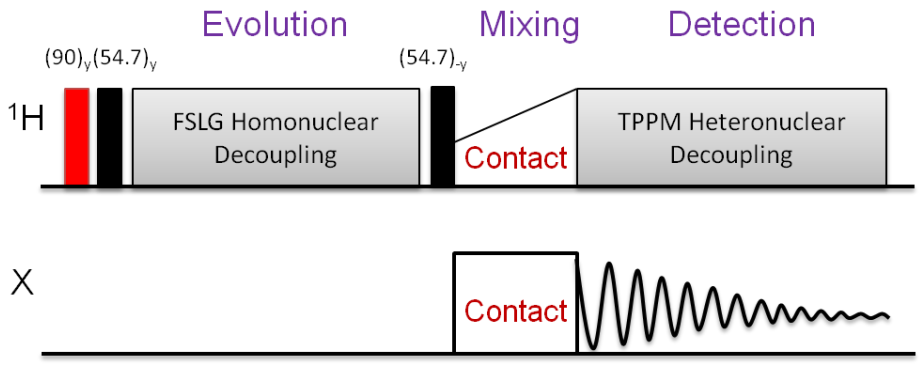

Figure 2.6 The pulse sequence of the ^{1}H-X Frequency Switched Lee Goldberg Cross Polarization Heteronuclear Correlation (FSLG CPMAS HETCOR). Adapted from ref [55].

The time during which the polarization transfer takes place is called contact time, and it is a key factor to observe strong or weak interactions in the system. It is usually taken as 0.2 ms to 5 ms but can be increased up to 10 ms. If short contact times are applied (0.2-2 ms), then short distance correlation between ^{1}H and X are typically observed in the spectrum, while in case of longer contact times (>3 ms), long distance correlations are obtained in the spectra.

3. Dynamic Nuclear Polarization

3.1. Introduction

NMR is a low sensitive technique as compared to other spectroscopic methods. One possibility to overcome sensitivity issues is the use of hyperpolarization, meaning that polarization is generated by shifting the population difference far away from thermal equilibrium (Figure 3.1). There are several hyperpolarisation methods available, such as Dynamic Nuclear Polarization (DNP) [22, 56-58], Para Hydrogen Induced Polarisation (PHIP) [59-64], dissolution DNP (d-DNP) [64, 65], Signal Amplification By Reversible Exchange (SABRE) [64], Chemically Induced Dynamic Nuclear Polarisation (CIDNP) [66] and Spin Exchange Optical Pumping (SEOP)[67-71] etc. Since this thesis focuses on solid-state NMR-DNP, the chapter is limited to DNP and its instrumentation and working principle. An excellent review on DNP with detailed theoretical and technical aspects, including mechanisms is given by Thankamony et. al.[72] and Akbey et. al. [73]. The basic principle of DNP is based on polarization transfer from an electron to a nucleus. Since the gyromagnetic ratio of the electron is 660 times the gyromagnetic ratio of the ^{1}H nucleus, the polarization achieved for electrons is much higher than that of ^{1}H according to the Boltzmann distribution.

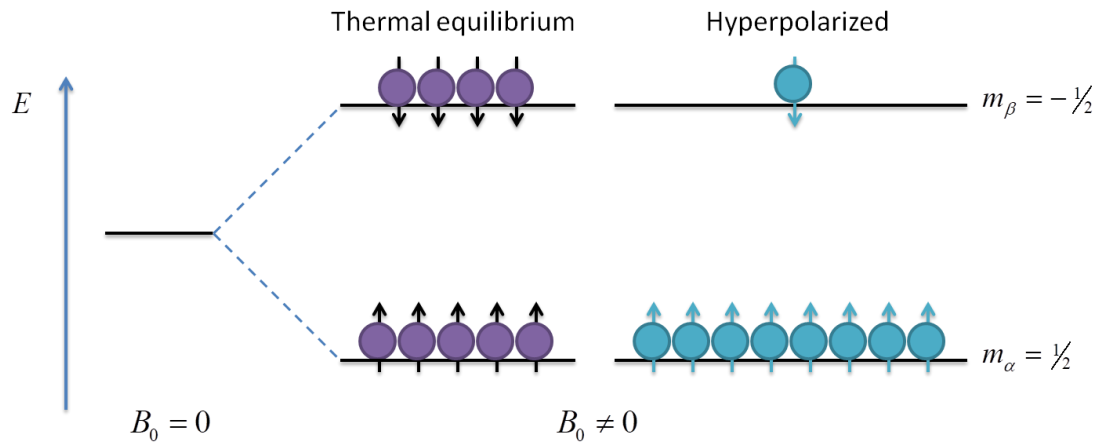

Figure 3.1 Spin population in the presence of a magnetic field B_o for thermal equilibrium (purple) and hyperpolarization (cyan).

The basic idea of DNP was first theoretically proposed in 1953 by Albert Overhauser [74] and experimentally verified by Carver and Slichter [75], which later was named as Overhauser Effect (OE). In OE, the transitions of the electrons are saturated by microwave irradiation in order to achieve the enhancement. Initially it was demonstrated on ^{7}Li NMR signal enhancement using conducting electrons in Lithium metal, which resulted in an enhancement

factor of up to ~100 [75, 76]. Soon after, in 1957, DNP was demonstrated on non-conducting solids by Jeffries [77], and experimentally and theoretically verified by Abragam and Proctor [76] in 1958, later known as solid-effect [76]. Likewise, in subsequent years, the different mechanisms on DNP, for example cross effect [78] (1967) and thermal mixing [79, 80] (1978) were discovered. As the DNP effect at high magnetic fields requires a high power and high frequency microwave sources, which were not available at that time, DNP was not considered as relevant in NMR and was long forgotten. In the 90's, the field of DNP was further developed by the innovative work of Robert G. Griffin at MIT, who developed high frequency and high power microwave devices to make DNP applicable for high magnetic fields [81, 82]. Furthermore, Low Temperature (LT) DNP Magic Angle Spinning (MAS) probes were designed for solid-state applications [81, 83, 84]. Thus in the past few years, solid-state DNP-NMR techniques have evolved into a powerful analysis tool with widespread applications ranging from structure determination of bio-molecules over nanoparticles to surface analysis of porous catalysts [72, 85-90]. In this thesis, we will utilize solid-state DNP-NMR to study the surfaces of porous materials [91, 92].

3.2. Enhancement in DNP Experiments

The sensitivity enhancement factor (ε) in DNP NMR experiments can be determined by recording two spectra, one with microwave irradiation (MW on) and another one without microwave irradiation (MW off) and comparing the signal intensity, which can be done by overlapping the two spectra. In general, the maximum achievable theoretical enhancement factor for ^{1}H is 660, which is determined by γ_e / γ_H, the ratio of gyromagnetic ratio of electron relative to ^{1}H. Since the signal to noise ratio is directly proportional to the square root of the measurement time (SNR $\propto \sqrt{t}$), this implies that a ^{1}H spectrum can be recorded ε^2=435600 times faster using DNP-NMR compared to standard NMR to achieve the same signal to noise ratio.

3.3. Instrumentation for DNP-NMR

Modern solid-state DNP spectrometers [93, 94] consist of three main devices as shown in Figure 3.2, (i) the NMR magnet system, (ii) the gyrotron system and (iii) the cooling cabinet. The gyrotron in the Darmstadt lab generates high power microwaves irradiation (9.7 T, 263 GHz). It is controlled by a console and computer system that allows to turn on/off the microwave. Microwaves produced by the gyrotron are then transferred through a waveguide (transmission line) to the DNP probe placed in the NMR magnet system. In addition, a

separate cooling unit containing heat exchangers is connected with the probe to keep the probe cool at the required temperature (100K)

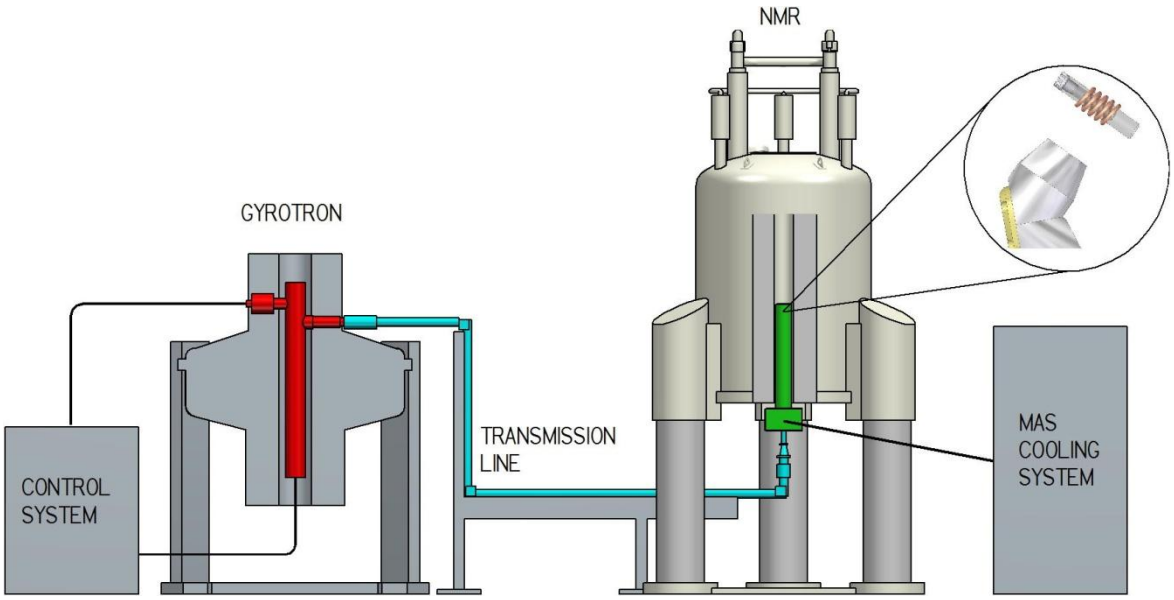

Figure 3.2 Schematic diagram of the commercial MAS DNP NMR employed with Gyrotron (Red), a waveguide (Cyan) and low temperature NMR probe (Green). Reprinted with permission from ref [94]. Copyright 2016 Elsevier Inc.

3.3.1. Sample for DNP Measurements

As most DNP mechanisms are based on the presence of an unpaired electron, it is common to have an unpaired electron as polarization source in the system. In most cases, the sample of interest does not have an unpaired electron by itself. Thus, the sample has to be impregnated with a stable free radical in aqueous (water/glycerol) or organic (TCE) solvent depending on the wetting properties of the system. The most commonly used radicals are AMUPol[88], TEKPol[95], TOTAPOL[96] and bTbK[28] and their chemical structures are shown in Figure 3.3. The hydrophilic solvent is typically a mixture of 60% glycerol-d_8, 30% D_2O and 10% H_2O (w/w/w), while as organic solvent typically TCE is utilized. Glycerol promotes the formation of glass like structures upon cooling that are required for efficient polarization transfer from electrons to the nearby protons. The presence of H_2O next to D_2O provides the necessary protons to allow proton spin diffusion that spread up the polarization across the sample[97, 98]. Thus, the signals for the nuclei, which are even farther than 1 μm in space [99] are enhanced, which is not achievable by methods like cross polarization.

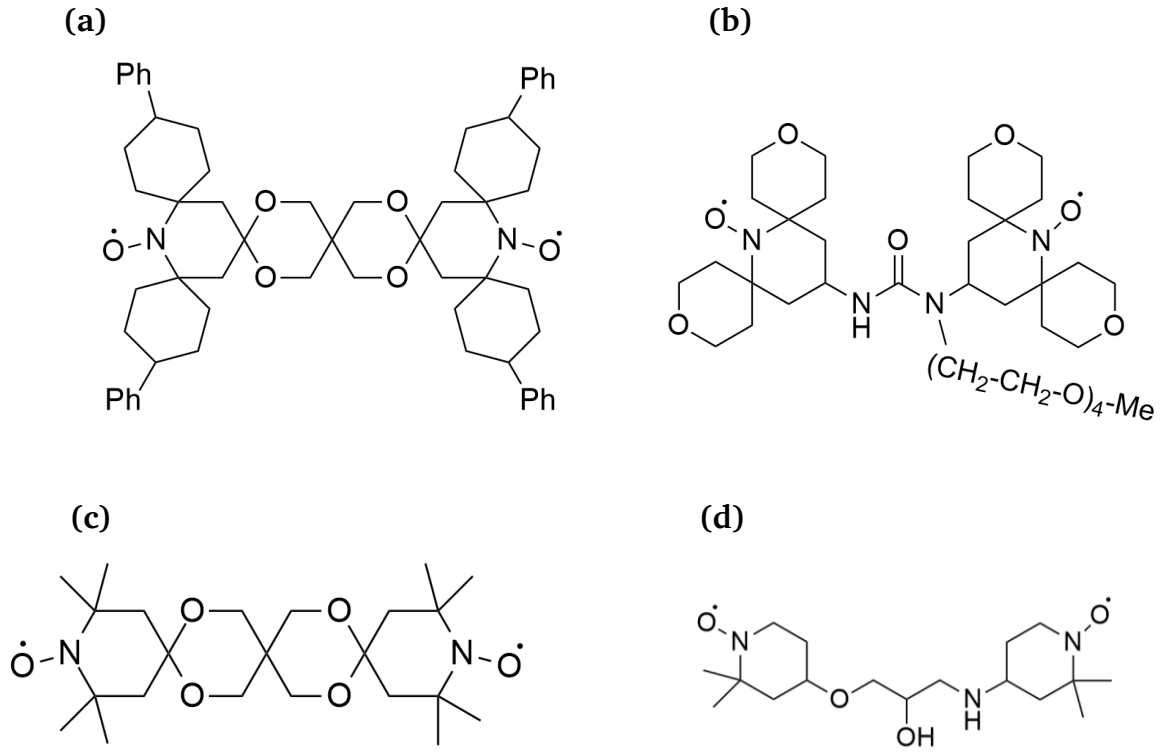

Figure 3.3 Chemical structure of commonly used radicals in DNP: (A) TEKPol, (b)AMUPol, (c) bTbK and (d) TOTAPOL.

3.4. DNP Mechanisms

There are different mechanisms to transfer the polarization from an electron to a nucleus. The most common ones obtained in the solid-state are the Solid Effect (SE), the Cross Effect (CE), Thermal Mixing (TM) and Overhauser effect (OE). Very recently, a NOE type mechanism has been proposed that requires molecule dynamics at low temperature. The description will start with the (OE), as this was the first scenario where the existence of DNP was discovered. Then the SE and CE are described followed by TM. Finally, a short introduction on cross-relaxation (CR) DNP is given.

3.4.1.The Overhauser effect

As mentioned the DNP phenomenon was first recognized by Overhauser effect in 1953 [74] in liquids as it requires fluctuations of the hyperfine coupling close to the Larmor frequency of the electron, which was available in metals with free conducting electrons or in liquids. The fluctuations cause the relaxation process where an electron and nucleus can flip their state simultaneously via the zero quantum and double quantum transitions. In solids, OE requires mobile electrons, as in conduction band of the metal and thus OE in solids was not expected.

However, surprisingly, OE was discovered in insulating solids in 2014 by Can et al.[100] with BDPA radicals and its water soluble derivative sulfonate BDPA (SA-BDPA) in glycerol/water mixture. With these radicals, the efficiency of DNP scales favorably with the magnetic field from 9.4T to 18.8 T [100, 101].

The Overhauser effect can be understood by a coupled spin system containing one electron spin and one nuclear spin, which are involved in a cross relaxation process via zero quantum (ZQ) and double quantum (DQ) transitions. This mechanism is explained by the energy level diagram illustrated in Figure 3.4. W_0, and W_2 are the rates at which zero quantum (ZQ) and double quantum (DQ) transitions occur respectively, whereas W_e and W_n are the rates for the electron and nuclear transitions. W^o is the nuclear relaxation rate in the absence of electrons. In the Overhauser effect the allowed electron transitions (SQ) are saturated at the electron Larmor frequency ω_e, while the zero and double quantum transition enhances the nuclear polarization and results into the DNP effect. The positive or negative enhancement depends on the ratio between W_0 and W_2. If the DQ transition rate (W_2) is higher than the ZQ transition rate (W_0), positive enhancement is observed, and vice versa. For detailed information on the OE effect the interested reader is referred to ref [56, 102].

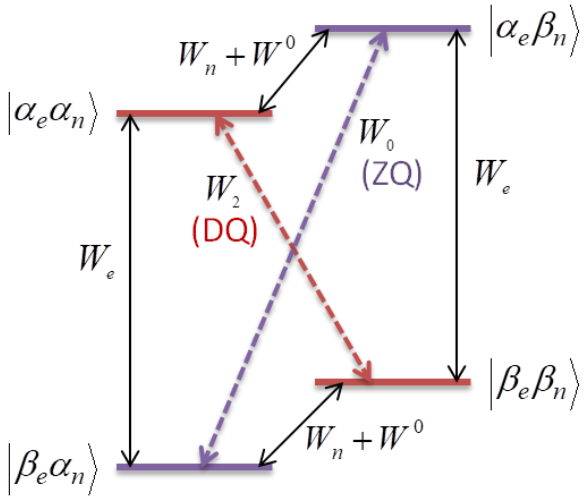

Figure 3.4 Energy level diagram describing the mechanism for OE using a two-spin system containing of an electron spin and a nuclear spin. W_0, and W_2 are the ZQ and DQ transition rates respectively. W^0 is the nuclear relaxation rate in the absence of electrons. Adapted from ref [56].

3.4.1.The Solid effect

In 1957, C. D. Jeffries proposed the phenomenon of electron polarization transfer to nuclei via forbidden ZQ and DQ transitions, which was further experimentally verified by Abragam

and Proctor in 1958 [74, 103]. The solid effect phenomenon can be described similar to the Overhauser via a four-level energy diagram [76, 77, 103]. Such diagram is shown in figure Figure 3.5. The solid effect occurs when the nuclear Larmor frequency (ω_n) is greater than the homogenous (δ) and inhomogeneous (Δ) EPR line width. In such a case, the non-secular coupling between electron and nucleus results into partial mixing of the spin states and thus partially allows the forbidden transitions (ZQ and DQ), which can be induced by microwave irradiation, which drives the polarization from the electron to the nucleus. The solid effect relies on the matching of the microwave irradiation frequency with the difference/sum of the Larmor frequencies of nucleus and electron as follows:

$$\omega_{\mu w} = \omega_e \pm \omega_n \tag{3.1}$$

Here, $\omega_{\mu w}$ is the microwave irradiation frequency while ω_e and ω_n are the Larmor frequencies of the electron spin and nuclear spin, respectively. Signal enhancements with positive or negative amplitude can occur depending on the microwave irradiation frequency. For example, microwave irradiation at the frequency $\omega_{\mu w} = \omega_e + \omega_n$ excites the ZQ transition, which occurs between spin states $|2\rangle$ and $|3\rangle$ that leads to negative enhancement. On the other side, microwave irradiation at frequency $\omega_{\mu w} = \omega_e - \omega_n$ excites the DQ transitions between spin states $|1\rangle$ and $|4\rangle$ that leads to positive enhancement in the system.

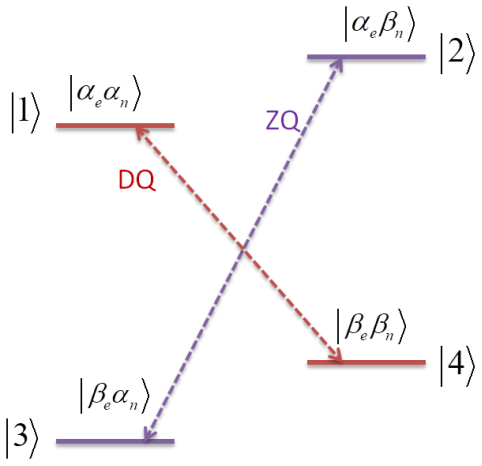

Figure 3.5 Energy level diagram of a two spin system (*I*=*S*=1//2) consisting of an electron and a nucleus to illustrate the mechanism of the solid effect (SE). Saturation of forbidden ZQ and DQ transitions, drawn in purple and red, lead to negative and positive enhancement in the system. Adapted from ref [56, 72].

3.4.2. Cross effect

Few years after the discovery of the solid effect, in 1967, Hawang and Hill presented a second mechanism in DNP, called cross effect (CE) [79, 80]. The cross effect involves a three-spin system consisting of two electrons and one nucleus, with strong electron-electron dipolar interaction and hyperfine coupling between one of the electrons to a nucleus. The cross effect can be understood by an eight-level energy diagram shown in Figure 3.6. For the cross effect to occur, it is required that the difference between the Larmour frequency of the two electrons (ω_{e1}, ω_{e2}) match the nuclear Larmor frequency as per expression shown below:

$$\left|\omega_{e1} - \omega_{e2}\right| = \omega_n \qquad (3.2)$$

The condition for CE is achieved when the energy levels $|\alpha\beta\alpha\rangle$, $|\beta\alpha\beta\rangle$ are degenerate or energy levels $|\alpha\beta\beta\rangle$, $|\beta\alpha\alpha\rangle$ are degenerated. In our case, we consider the degeneracy of energy levels $|\alpha\beta\alpha\rangle$ and $|\beta\alpha\beta\rangle$. When the condition is matched, continuous microwave irradiation induces the allowed electron transition for one of the electrons (e1) at the frequency ω_{e1}, which leads to saturation of all 4 connected energy levels (orange solid lines in Figure 3.6b). This further leads to CE transitions (orange dashed lines), which enhance the polarization and negative enhancement is obtained (Figure 3.6b). In a similar manner, when the transitions of the second electron (e2) are saturated (blue solid lines in Figure 3.6c) at the frequency ω_{e2}, positive enhancement is obtained (Figure 3.6c). As compared to the solid effect, the cross effect becomes the dominating mechanism in systems when the nuclear Larmour frequency (ω_n) is larger than the homogenous EPR line width (δ) and smaller than the inhomogeneous EPR line width (Δ), namely ($\delta < \omega_n < \Delta$).

At the time of discovery of CE in 60s, this mechanism was only investigated for monoradicals. Half a century after the discovery of DNP, in 1990's researchers in the DNP community inclined towards the development of cross effect-based polarizing agents. In 2004, Hu et. al introduced chemically engineered biradicals by linking two TEMPO radicals through a poly-(ethylene glycol) chain as shown in Figure 3.7, which was named as bis-TEMPO-n-ethyleneglycol (BTnE) and the obtained DNP enhancements with such radical was 3-4 times higher than the one achieved by monoradicals [104].

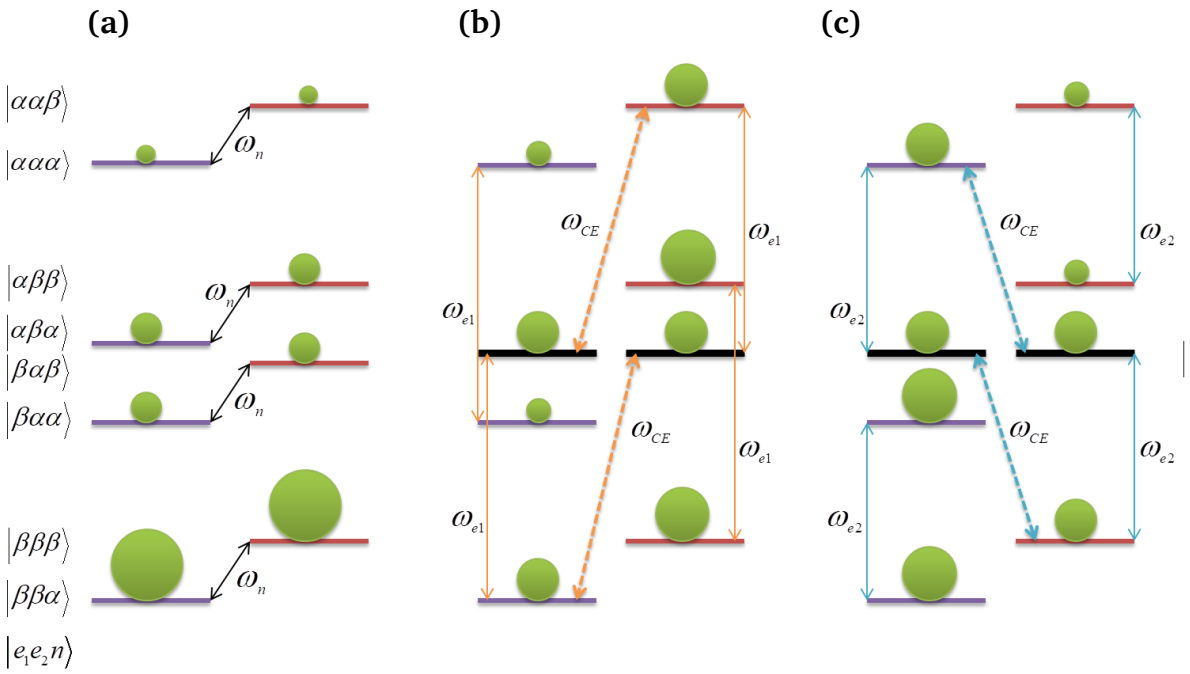

Figure 3.6 The representation of eight energy levels in a three spin system involving electron e1, electron e2 and a nucleus n, describing the mechanism of the cross effect (CE). The energy states are shown by the eigen states given as $|e_1e_2n\rangle$. (a) Population distribution of 3 spin system at thermal equilibrium, (b) Saturation of single quantum electron transitions of electron 1 (e1) leads to negative enhancement, (c) Saturation of single quantum electron transitions of electron 2 (e2) leads to positive enhancement. The black, orange and blue solid arrows show the allowed single quantum transition for the nucleus (n), e1 and e2 respectively, while the dashed orange and blue arrow show the CE transition to enhance the nuclear polarization. The green sphere represents the population distribution in each spin state. Adapted from ref [56].

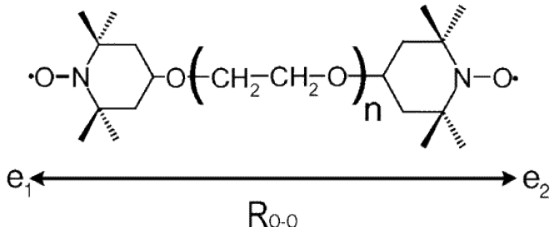

Figure 3.7 The linking of two TEMPO radicals using a poly-(ethylene) chain, where n is the number of ethylene glycol units. $R_{O\text{-}O}$ represents the dipolar distance between the two unpaired electrons. Reprinted (adapted) with permission from ref [105]. Copyright (2004) American Chemical Society.

Later biradicals such as TOTAPOL [96], bTbk [106], TEKPol [95]and AMUPol [88] were introduced for DNP experiments. In these radicals, the dipolar coupling between the electrons is between 20-35 MHz which lead to even higher enhancements. For a more detailed description the reader is referred to references [56, 79, 80, 107-113].

3.4.3. Thermal Mixing

Furthermore, there is a fourth mechanism called TM, which was proposed by Abragam and the theoretical background is described in ref [76, 114]. The mechanism is significantly active in experiments carried out at low temperature (≈10 K) and plays no active role in experiments carried out between 95-200 K. The mechanism of TM is similar to CE [80] but occurs in systems having high radical concentration, where multiple electrons are dipolar coupled to each other and a nucleus hyperfine coupled to an electron. As the name suggests, the TM effect may be understood from the thermodynamic point of view. Here the system containing of electron spins and a nuclear spin is divided in ensemble of three interacting baths, each at particular spin temperature: the electron Zeeman system (EZS), the electron dipolar system (EDS), and the nuclear Zeeman system (NZS). The TM effect can be explained by a many level energy diagram including spin temperature defined for each energy states as described by Hu et. al. [108].

3.4.4. Direct vs Indirect Polarization Transfer

Next to the OE, SE, CE and TM, a fifth mechanism has been introduced in parallel by the Buntkowsky and the Corzilius group [115, 116]. The phenomenon was observed in DNP enhanced ^{13}C direct polarization experiments on surfactant systems like PEG [115]. It was observed that some of the enhanced signals contained positive amplitude while some had negative amplitude. At the same time in an independent research the Corzilius group observed the similar effect while working on amino acids [116]. Since the structure and physical properties of PEG and amino acids are fundamentally different, it was considered that the effect is of general netaure in case of ^{13}C DNP spectra and is based on a different transfer mechanism.

The effect can be explained by the spectra set in Figure 3.8. The black spectrum shows the ^{13}C MAS spectrum measured on a sample containing 20 mmol·kg^{-1} AMUPol dissolved in $C_{10}E_6$ and exhibits an unusual line shape. The sample was than further studied by applying rotor synchronous 180° pulse on proton channel during the ^{13}C build up time. A broad spectrum with positive enhancement (red spectrum) was obtained. This broad signal was investigated in detail by the Hahn echo experiment and it was concluded that the line broadening is happening due to interaction between the nuclei and radicals [117, 118]. The 180° pulse train suppresses all the negative signals in the spectra and only leads to positive signal as shown by red spectrum. This was later called direct channel as this signal refers to^{13}C direct polarization. In addition, it was obtained that the polarization in the ^{13}C MAS (black

spectrum) also occurred through the proton spins, which was called indirect polarization as compared to the direct channel. The ^{13}C MAS spectrum (black) shows the summation of the polarization transfer through e→^{1}H→^{13}C (indirect) and e→^{13}C (direct). This means that the indirect channel polarization can be obtained by the difference spectrum between black (measured without rotor synchronous 180° pulses) and red spectrum (measured with 180° rotor synchronous 180° pulses). The difference spectrum is represented by the purple spectrum in Figure 3.8.

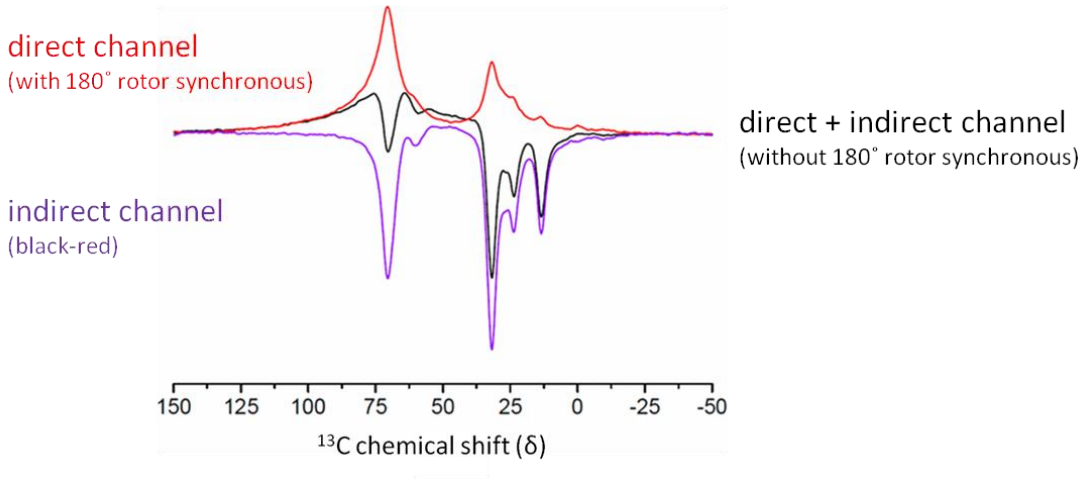

Figure 3.8 ^{13}C MAS spectra of the sample containing 20 mmol·kg^{-1} AMUPOL dissolved in $C_{10}E_6$ obtained with MW on: The black spectrum shows the summation of signals originating from the "direct channel" and "indirect channel". The red spectrum shows the spectrum obtained after applying additional rotor synchronous 180° pulses, which shows signals only originating from the "direct channel". The purple spectrum shows the difference spectrum obtained after subtracting the red spectrum from the black one. This spectrum represents the signal only originating from the "indirect channel". Adapted from ref [115].

The explanation on the polarization transfer from the proton spin reservoir to the ^{13}C nuclei is related to a NOE type mechanism and was suggested by Corzilius and co-workers [116]. It was referred to dynamic effects which originate from rotations of methyl groups [119, 120]. However, the effect was also observed in surfactants like PEG, which have no methyl groups. This encouraged to further study in this direction, involving other solutes, for example cyclohexane. These studies suggested that some other dynamics/motion are present even at 100 K which seem to be preserved during the cooling process while transferring the sample in the spectrometer[118]. In addition, this mechanism was also studied at different magnetic field in order to investigate the field dependency and interested reader can refer to ref [117].

4. Mixture of octanol-1/water confined in Mesoporous Silica SBA-15

4.1. Introduction

Water is probably the most important substance on the Earth since most chemical and biological naturally occurring reactions require water [121]. Water is commonly known as a solvent and special properties of water allows it to behave as solute for some organic molecules such as alcohols [122]. Alcohols, containing the hydrophilic OH group, potentially form hydrogen bonds, which makes them compatible with water. Such compatibility between water and alcohol is modified when the molecules are present in confined environment as for example in the pores of mesoporous materials [123]. These interactions are still poorly understood as surface-surface and surface-liquid interactions take place at the same time. In addition, the mixture contains interactions, namely hydrogen bond formation between alcohol and water in confinement. Thus, the aim of this project is to inspect different types of interaction present in mixtures of alcohol/water and to identify which interactions are dominating in the system.

This is the key concept on which separation techniques, like oil-water separation, lubrication development and environmental studies are based on [124-128]. In addition, alcohol/water interactions play an important role in biological research [129, 130] as it has been demonstrated that octanol-1 [131-136] mimics lipid molecules in cell membrane; hence, it acts as an artificial membrane [137, 138]. Finally, the octanol-1/water partition coefficient is commonly used for determining the pharmacokinetic properties of drug molecules [139-141].

In this project, octanol-1 and octanol-1/water interactions with the surface of porous silica are studied using solid-state NMR spectroscopy. The NMR technique is very powerful to extract details on the local structure and dynamics of guest molecules in confinement as shown by recent reviews [142-145]. CPMAS and FSLG CPMAS HETCOR [55] (Frequency Switched Lee Goldberg Heteronuclear Correlation) experiments, which are based on dipolar interaction, provide a clear picture on interactions of molecules with surfaces. The strength of dipolar coupling for example allows to approximate the distance between ^{1}H nuclei and X nuclei such as ^{29}Si or ^{13}C [31, 146-155]. Molecular Dynamics simulations performed by our collaborators are used to underline the interpretation of solid-state NMR data. Such MD simulations give quantitative data by providing the number density profile of atoms involved in the system, as shown by an MD study on ethylene glycol-water in mesoporous silica [156]. Furthermore, they provide information on structure and dynamics and allow to study the trajectories of involved molecules. In the past, state-of-the-art methods such as MD simulations have been used to study diverse aqueous systems [53, 156-159] in silica pores [160], or

in alumina pores [160]. Very recently, a combination of solid-state NMR and MD simulation was utilized to study the microphase separation in water-isobutyric acid mixtures in confinement. [53] Similar studies can be also found in refs. [161, 162]. In general solid state NMR [121, 163-168] and MD simulations [158-160, 169] studies provide valuable information on confined liquids.

While studies carried out in the past mostly focused on short chain alcohols such as ethanol and isopropanol [142, 156, 170-172], in the present work the long chain alcohol octanol-1 is investigated[173]. For this, SBA-15 is impregnated with octanol-1 or octanol-1/water mixtures and solid state NMR combined with MD simulations techniques are utilized to analyze the interactions between the liquid and surface.

4.2. Experimental section

4.2.1. Synthesis and Characterization of Mesoporous Silica SBA-15 Material

The synthesis of the porous materials and their basic characterization was performed by Dr. Martin Brodrecht in a parallel project at our laboratory in Darmstadt. For synthesis of SBA-15, a method proposed by Zhao et al was followed [64]. Detailed steps about the synthesis are given in the original work [24].

The surface and the pore parameters for SBA-15 were determined using the Brunauer−Emmett−Teller (BET) method. From these measurements (appendix, Figure 9.1a) a pore volume of 1.2 cm^3/g and a specific surface area of 680 m^2/g (BET) was determined. The pore diameter was investigated by the Barrett, Joyner, and Halenda (BJH) method and was found to be 6.4 nm (appendix, Figure 9.1b). For details on BET and BJH, the reader is referred to our original work [24].

4.2.2. Sample Preparation for Solid-state NMR

The octanol-1 used in our experiments was purchased from Sigma Aldrich (>99% purity) and hence was used without any further purification. To remove traces of water from octanol-1, it was treated with 5Å molecular sieves for one week. Further, to achieve its single-phase mixture, the octanol-1/water mixture was prepared at 80:20 mol% ratio of octanol-1 and water according to the phase diagram[174]. The single-phase mixture was necessary to have a complete homogenous mixing of octanol-1 and water in the mixture.

In the first step, the 4 mm ZrO_2 rotor was filled with SBA-15 material and was put under vacuum for overnight at room temperature to dry out the residual moisture. After vacuum

treatment, the rotor was taken out and put into the spectrometer for ^{1}H and ^{29}Si measurements of the pure SBA-15. In the next step, the required amount of octanol-1 was added and immediately the sample was put in the spectrometer and 1D ^{1}H spectra were measured over time. When the 1D ^{1}H spectra were observed to be stable (i.e. when the absorption of liquid to SBA-15 was completed) the data on ^{1}H and ^{29}Si was collected by performing CPMAS and 2D FSLG CPMAS HETCOR experiments.

4.2.3. Solid-state NMR Experiments

All standard solid-state NMR experiments were performed on a Bruker AVANCE III HD spectrometer operating at 14 T magnetic field corresponding to a frequency of 600.12 MHz for ^{1}H and 119.22 MHz for ^{29}Si with 4 mm ZrO_2 rotors using a spinning rate of 8 KHz. $^{1}H-^{29}Si$ CP-MAS and FSLG CPMAS HETCOR experiments were performed with different contact times, which varied from 3 ms to 9 ms to differentiate between short-range and long-range correlations. The experiments were performed with 32 slices and 256 scans for each slice with recycle delay of 4 s. The homonuclear decoupling was conducted employing the Frequency Switched Lee Goldberg (FSLG) scheme with a 96 KHz ^{1}H RF field during the evolution of chemical shifts. The TPPM 15[46] scheme for heteronuclear decoupling was applied during data acquisition.

4.2.4. Molecular Dynamics simulations

To bolster the interpretation of the NMR results, MD simulations were done by the group of Prof. Drossel from TU Darmstadt. MD simulations were conducted for hydrocarbon chain and hydroxyl group of octanol-1using the NAMD simulation package[132] for two different mixture: (a) 90:10 mol% of octanol-1/water, (b) 70:30 mol% of octanol-1/water. The detailed information on the MD simulation can be found in our original work in ref [24].

4.3. Results and Discussion

4.3.1.Wetting Properties of SBA-15

In the first step, the physio-chemical properties of SBA-15 upon addition of water were analysed. In order to achieve this, a rotor filled with SBA-15 was investigated at different level of water content (moist silica, dried silica and wet silica) through ^{1}H solid-state NMR spectroscopy as shown in Figure 4.1. Figure 4.1a shows the ^{1}H chemical shift of moist silica

at about 4.2 ppm. This chemical shift shows the involvement of surface hydroxyl groups interacting with residue water molecules through hydrogen bonds, which can be understood more clearly by the model depicted in Figure 4.1a'. When the same silica is put under vacuum for overnight, the chemical shift is moved to 1.7 ppm (Figure 4.1b), which is attributed to removal of any external water residue. The ^{1}H chemical shift at 1.7 ppm points toward the presence of only silanol groups of dried silica as shown in model (Figure 4.1b'). In the next step, the silica was wetted with a drop of water (0.5 μl) and the chemical shift moved to 4.9 ppm (Figure 4.1c). This is clear as more water molecules start to interact with the silica surface through hydrogen bondings and form an extensive hydrogen bonding network as shown in Figure 4.1c'. These observations imply that the 1H chemical shift of SBA-15 highly depends on the water-content, and it shifts to higher chemical shift values with increasing amount of water.

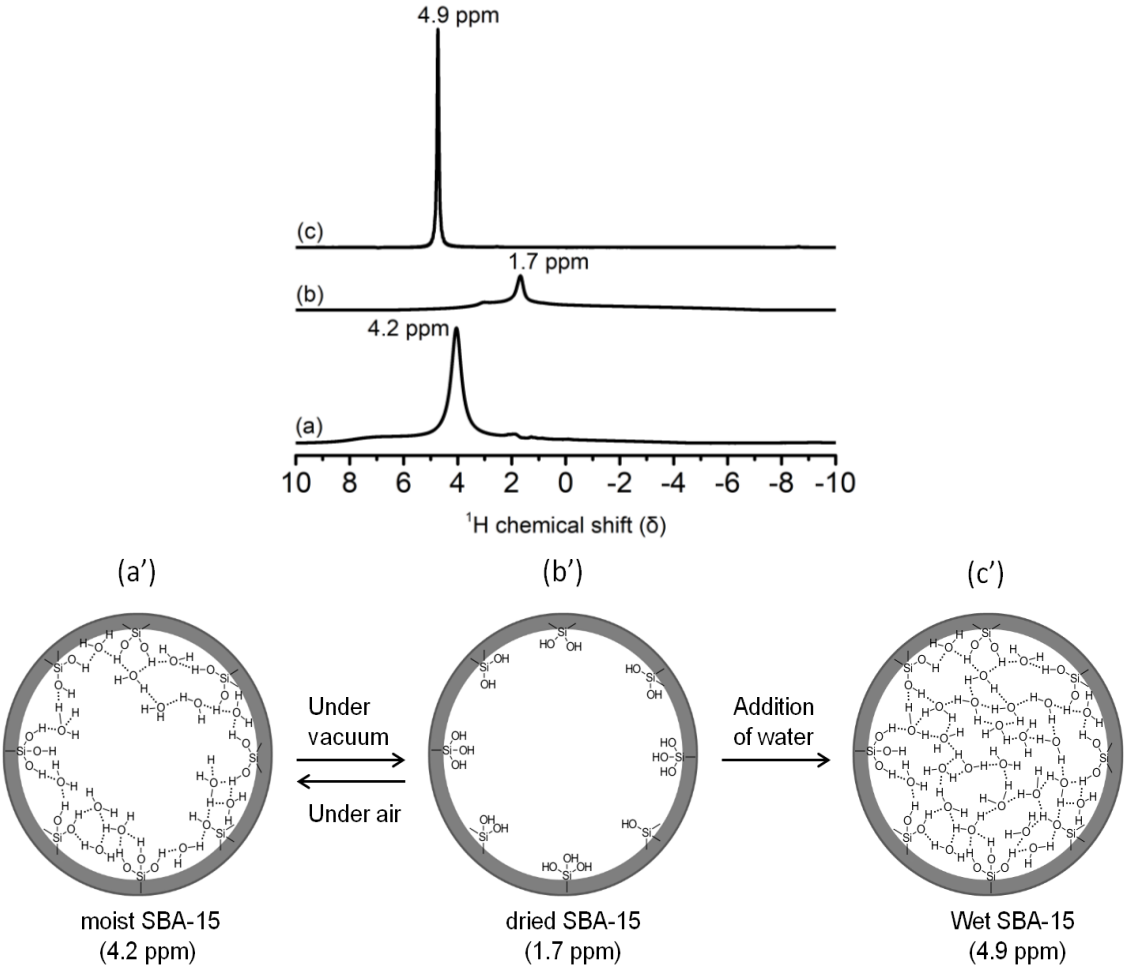

Figure 4.1 Normalized ^{1}H spectra of SBA-15 with different content of water recorded at 8 kHz spinning rate at room temperature and their corresponding exemplary model (a), (a') Moist SBA-15; (b), (b') Dried SBA-15; (c),(c)' wet SBA-15. Adapted from ref [24].

Furthermore, ^{1}H-^{29}Si CPMAS experiments were performed on dried silica and moist silica to investigate the functional groups on silica surface. It was observed that the line shape and chemical shift of both the spectra were exactly same and thus ^{1}H-^{29}Si CPMAS spectra of moist silica is shown in (Figure 4.2). A combined peak at around -100 ppm was obtained, which is attributed to Q_n groups It consists of Q_2, Q_3 and Q_4 groups with chemical shift values of -92.9, -102.8 and -109.9 ppm, respectively [175], which were extracted by performing a multiple Gauss function fit.

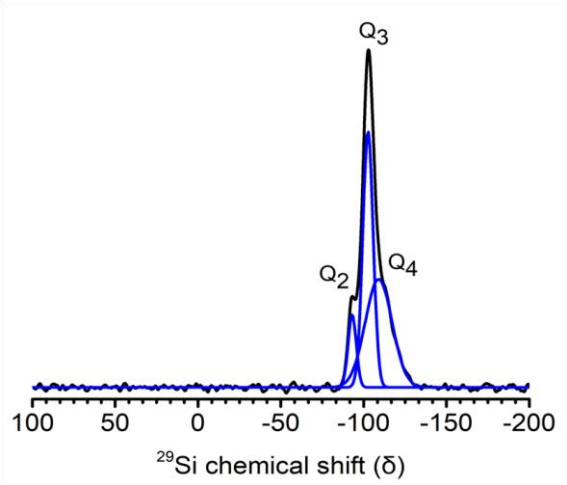

Figure 4.2 ^{1}H- ^{29}Si CPMAS spectrum of moist SBA-15 recorded at 8 kHz spinning rate at room temperature. Adapted from ref [24]. Copyright (2018) American Chemical Society.

4.3.2. ^{1}H-^{29}Si FSLG CPMAS HETCOR investigations on SBA-15

Since the project aims at investigating interactions of octanol-1 or octanol-1/water mixtures with the silica pore, it is required to conduct an experiment which takes account of 2 nuclei. The method of choice here is to correlate the ^{29}Si of the silica surface with the ^{1}H of the octanol-1/water mixture. Therefore ^{1}H-^{29}Si FSLG CPMAS HETCOR experiments were performed on the samples. As it has been discussed in the above paragraph, the proton chemical shift depends significantly on the amount of water. Thus, it is required to have a completely dried SBA-15 sample before impregnation with octanol-1; otherwise, the water which is already present in SBA-15 will prevent guest molecules to interact with the silica surface. In addition, it is important to first record the FSLG CPMAS HETCOR spectrum on the SBA-15 material without any loading of octanol-1 or octanol-1/water mixtures in order to compare the results obtained with/without loading. Thus, the FSLG CPMAS HETCOR experiments were carried out on the dried as well as moist silica material and compared in Figure 4.3. The peak for the dried sample is observed at 1.7 ppm in the ^{1}H dimension, which shows the presence of free silanol hydroxyl groups in the absence of water. On the other

hand, for the moist silica, a peak at around 4.2 ppm is obtained in the ^{1}H dimension which shows the presence of significant amount of water inside the sample. These results are consistent with the ones obtained from 1D ^{1}H spectra in Figure 4.1.

Furthermore, the peak at 0 ppm on ^{1}H dimension as well as 0 ppm on ^{29}Si dimension in Figure 4.3 corresponds to the internal reference sample (TSP). The introduction of TSP in the sample was done in order to reference the ^{1}H indirect dimension, which is difficult in HETCOR spectra. This effect is further discussed in details in the introduction of chapter five, where we come up with a novel solution for the referencing problem of the indirect ^{1}H dimension.

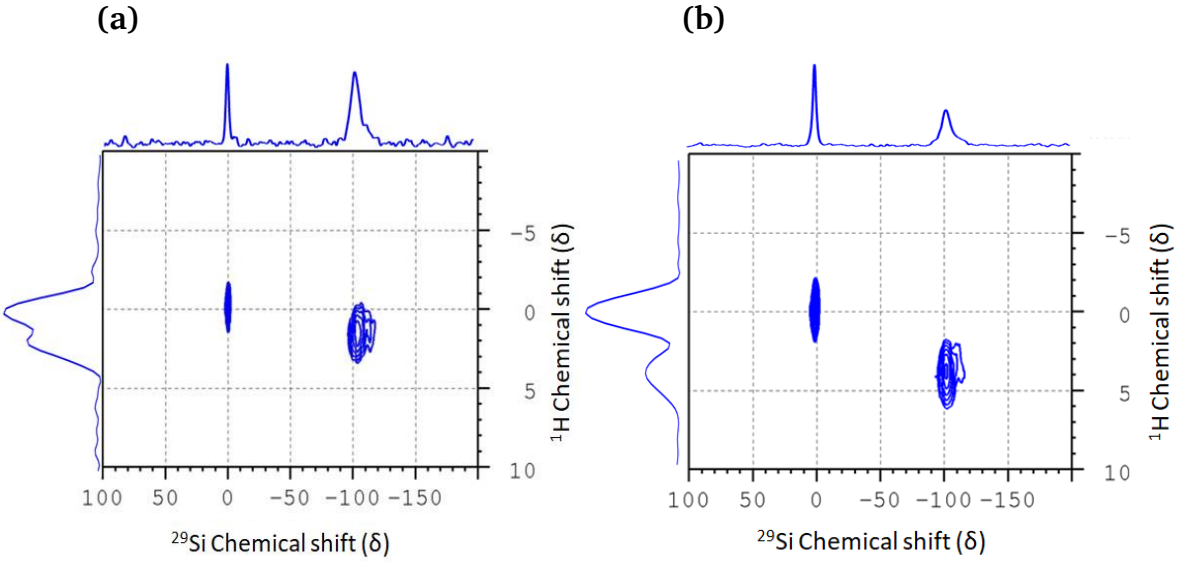

Figure 4.3 Room temperature ^{1}H-^{29}Si FSLG CPMAS HETCOR spectra of: (a) dried silica, which was measured after drying the SBA-15 under vacuum for overnight, (b) moist silica, which was measured of a sample stored at air and room temperature. The sample was mixed with small amount of TSP to reference the proton dimension. Adapted from ref [24].

Since the addition of TSP probably affects the system, the same set of experiment as in Figure 4.1 was performed with TSP and the results were compared between 'with TSP' and 'without TSP' spectra, which is given in Figure 4.4. The comparison between Figure 4.1 (with TSP) and Figure 4.4 (without TSP) provides consistent results, which allowed to assume that addition of TSP does not affect the system.

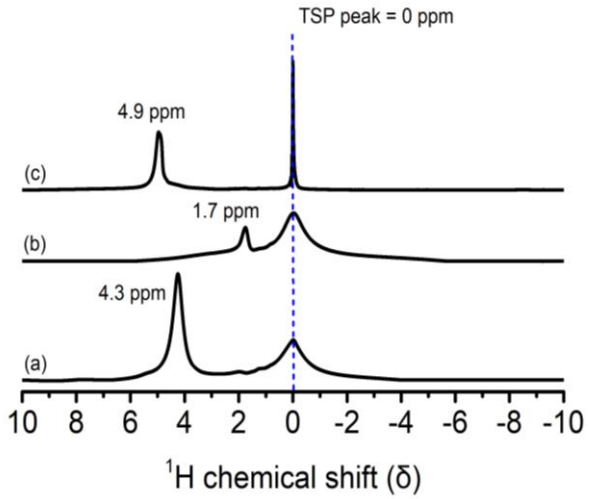

Figure 4.4 Normalized proton spectra of SBA-15 with different content of water recorded at 8KHz spinning rate at room temperature with TSP: (a) Moist SBA-15, (b) Dried SBA-15, (c) wet SBA-15. Adapted from ref [24]

4.3.3. ^{1}H-^{29}Si FSLG CPMAS HETCOR Experiments on SBA-15 with Octanol-1

^{1}H-^{29}Si FSLG CPMAS HETCOR spectra of dried SBA-15+TSP loaded with octanol-1 (80% pore filling) are shown in Figure 4.5. The experiments were performed at room temperature at a spinning rate of 8 kHz with short (3 ms) and long (9 ms) contact time. A signal around 4.9 ppm in the proton dimension and -103.0 ppm in the ^{29}Si dimension is observed in the spectrum obtained with 3 ms contact time (Figure 4.5a), which can be attributed to water saturated silica (Si-OH…OH-H) as discussed in section 4.3.1. Furthermore, such peak also indicates the presence of the –OH group of octanol-1 interacting with water molecules via an exchange process and then interacting with the silica surface. According to ref [176], which presents the study between small chain alcohol (methanol) and MCM, it shows that the hydrogen bonding between methanol and MCM is stable below 200 K. However, the formation and breaking of hydrogen bonds increases with increase in temperature. Thus, it can be assumed that the breakage of the hydrogen bond between octanol-1 and the silica surface at room temperature would be even more preferable. Due to the high probability of breakage at room temperature, more octanol-1 molecules are available in their free state in the system along with the bonded one with the surface. Thus, at the same time, there are two types of octanol present in the system; bound octanol, which is involved in a hydrogen bonding with the silica surface or with water molecules, and free octanol-1 which is far from the surface and supposed to be mobile. In order to detect the nuclei of interest which are far away from surface, the FSLG CPMAS HETCOR experiment was performed with 9 ms contact time. In Figure 4.5b, it can be seen that a signal at around 1 ppm in the ^{1}H dimension has appeared, which is correlating to Q_3 and Q_4 in the ^{29}Si dimension. This signal may indicates

the –OH groups from free-octanol in water-poor environment, however it also indicates the presence of aliphatic protons of octanol-1 molecules, which are far away from surface. This is the reason that the signal was not detectable in short range ^{1}H-^{29}Si FSLG CPMAS HETCOR experiment (3ms) but appeared in long range ^{1}H-^{29}Si FSLG CPMAS HETCOR experiment (9ms).

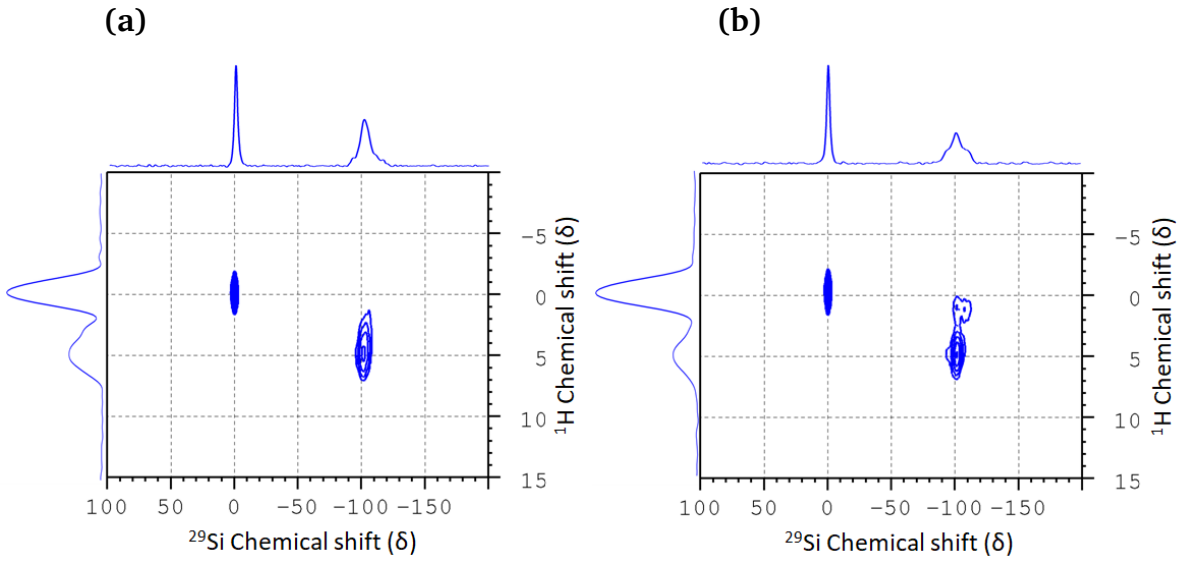

Figure 4.5 Room temperature ^{1}H-^{29}Si FSLG CPMAS HETCOR spectra measured at 8 kHz of dried SBA-15 mixed with neat octanol-1 measured with: (a) 3 ms contact time, (b) 9 ms contact time. Adapted from ref [24]. Copyright (2018) American Chemical Society.

4.3.4. ^{1}H-^{29}Si FSLG CPMAS HETCOR Experiment on SBA-15 with Octanol-1/Water Mixture

The same set of experiments was performed for SBA-15 imbibed with an octanol-1/water mixture (80:20 mol%). When the experiment was performed with 3 ms contact time (Figure 4.6), a peak at around 4.9 ppm was observed. This is comparable with the spectrum obtained for the water saturated silica sample as described in Figure 4.1**c'** in the previous section. This signal at 4.9 ppm is attributed to the silica surface hydrogen bonded with external hydroxyl molecules (Si-OH…OH-H). In a similar manner, the experiment was repeated with 9 ms of contact time to observe long distance correlations. When the experiment was performed with 9 ms contact time an additional signal at approximately 1 ppm in the proton dimension has appeared. As described above, the signal at 1 ppm suggests the presence of interactions between –OH groups of free-octanol-1 molecules and the silica surface, however it also suggests the interactions between the distant aliphatic protons and the silica surface.

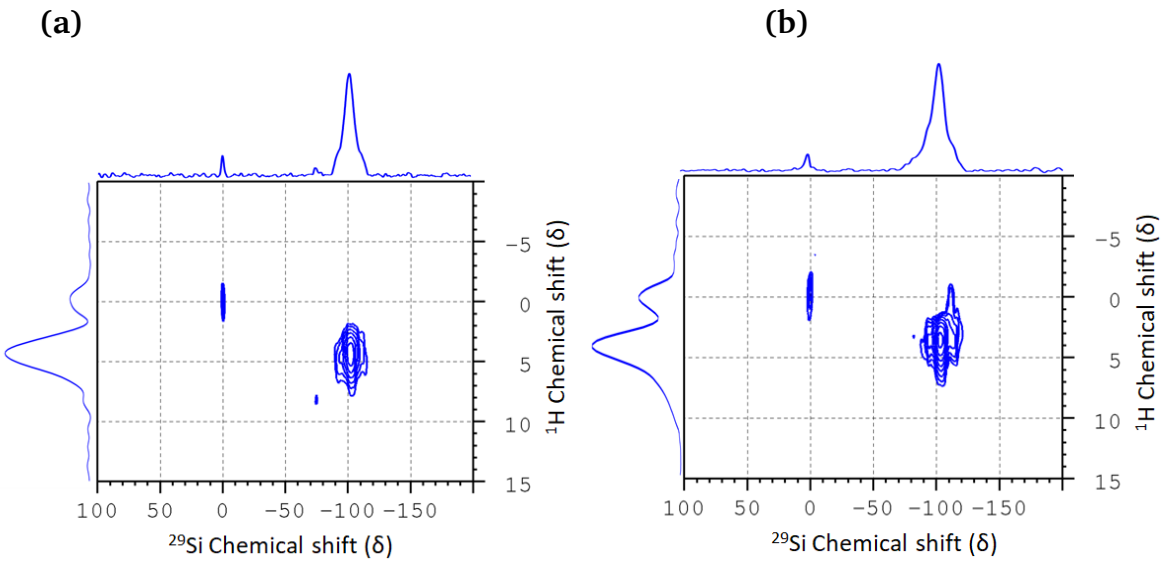

Figure 4.6 Room temperature ^{1}H-^{29}Si FSLG CPMAS HETCOR spectra measured at 8kHz of dried SBA-15 mixed with octanol-1/water mixture (80:20 by mol%) measured with: (a) 3 ms contact time, (b) 9 ms contact time. Adapted with permission from ref [24]. Copyright (2018) American Chemical Society.

From the above observation, it can be concluded that the –OH of octanol-1 is interacting with the silica surface along with –OH from water, which may be understood with the model shown in Figure 4.7, which shows the interactions at the molecular level between the silica surface and octanol-1 through the formation of hydrogen bonds.

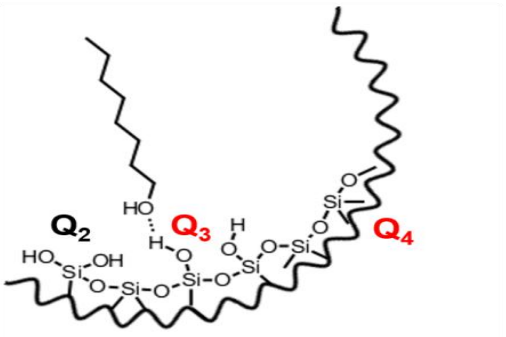

Figure 4.7 Model depicting the possible interactions in the system, hydrogen bonding between the octanol and silica surface. Reprinted (adapted) with permission from ref [24]. Copyright (2018) American Chemical Society.

To underline the interpretation of the solid-state NMR data, MD simulations were performed by the group of Prof. Drossel (TU Darmstadt). These MD simulations provide quantitative data, which are shortly discussed in the next section.

4.3.5. MD Simulations Studies

MD simulations provide quantitative data to support the results from solid-state NMR. The number density curves obtained from simulations (Figure 4.8a) indicate that the oxygen atoms attached to octanol-1 and water are highly concentrated near the pore wall and partially in the pore centre, which support the results obtained from solid-state NMR experiments. In addition, the carbon density profiles (Figure 4.8b) obtained for C1 and C8 of the octanol-1 assist this data, since it depicts that C1 (carbon attached to -OH) is abundant near the pore wall and carbon C8 (carbon of the methyl group of octanol) is found in the region between the pore wall and the pore centre.

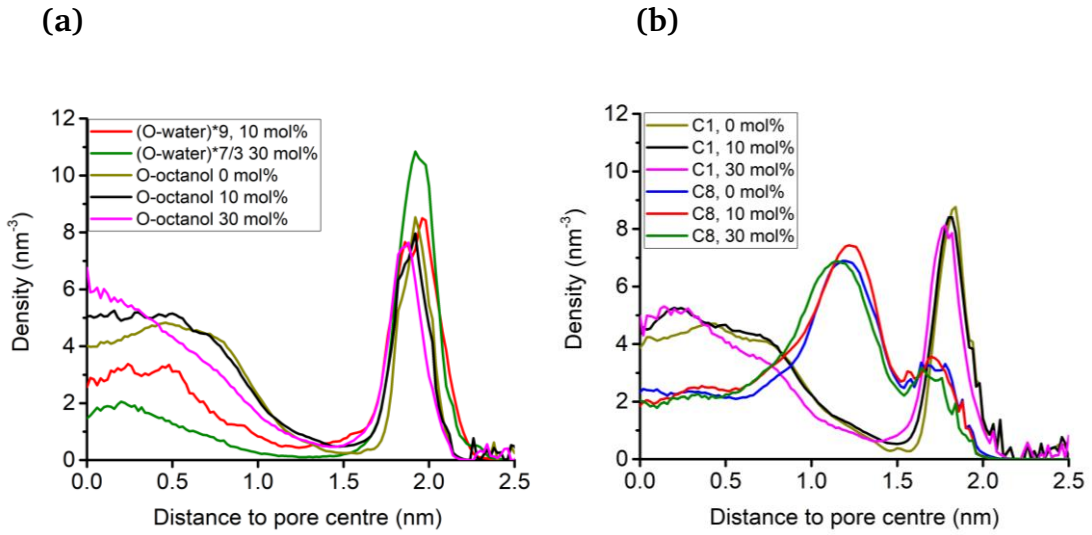

Figure 4.8 (a) Number density profile of oxygen atoms belonging to water and octanol-1 molecules, (b) Number density profile of carbons (first carbon C1 and last carbon C8 of the chain) belonging to octanol-1 molecules. The number density profiles are shown for octanol-water mixtures having 0, 10, 20 mol% of water content (100:0, 90:10, 80:20). Note: In (a) the density of water molecules was multiplied by the indicated factor for a better comparison. The simulation was performed at 425K. Reprinted (adapted) with permission from ref [24]. Copyright (2018) American Chemical Society

On the other side, the profiles also provide information on the different mixture content. For example the density of oxygen atoms of water is increased near the pore wall from 10 mol% to 30 mol%, which is obvious as a larger amount of water leads to accumulation of water near the pore wall due to preferable hydrophilic-hydrophilic interactions of water with the silica surface (Figure 4.8a), while the carbon density profile obtained for C1 and C8 signifies negligible changes upon addition of water from 10 mol% to 30 mol% (Figure 4.8b). These results are consistent with our interpretation of NMR data.

Moreover, the MD simulations also revealed the orientation of water/octanol-1 molecules in the silica pore region, which suggest the formation of a bilayer like structure from octanol molecules within the pore (validated from carbon density profile shown in Figure 9.2, in appendix), as shown by a model in Figure 4.9, which also fit quantitatively as the octanol length is 0.9 nm and pore radius is 2 nm.

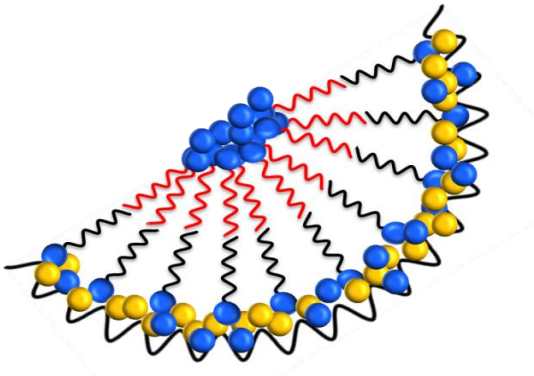

Figure 4.9 Graphical Model for the understanding of bilayer formation by water/octanol-1 inside the silica pore (black and red are aliphatic chains, blue and yellow circles represent the –OH groups attached to octanol-1 and Si respectively). Reprinted (adapted) with permission from ref [24]. Copyright (2018) American Chemical Society.

4.3.6. Conclusion

In this chapter, the behaviour of alcohol and alcohol-water mixture (octanol-1, octanol-1/water) confined in mesoporous silica SBA-15 have been thoroughly studied with state-of-the-art solid-state NMR techniques. The interpretation of the NMR data is supported by MD simulations. It can be inferred from the results that the interactions between the silica surface and octanol-1 or octanol-1/water occur entirely through hydrogen bonding. Our experimental results also showed that –OH group (from octanol-1/water) have a high tendency to be found near the silica surface. The silica surface preferable interact with the water molecule -OH compared to the octanol-1 -OH due to strong hydrophilic-hydrophilic interactions. The alignment of octanol was also deduced. The hydrophilic head group (-OH) of the octanol-1 stayed near the pore wall and the hydrophobic tail (aliphatic chains) remained in the intermediate range. It was also observed that this behaviour is independent of the mixing ratios, which elicits that the hydrophilic-hydrophilic interactions are much stronger as compared to hydrophobic-hydrophilic interactions. Finally, it can be concluded that the data provided by solid-state NMR and MD simulations complement each other and reveal a clear picture of the orientation, interactions and behaviour of water/octanol-1 molecules under the confinement of mesoporous silica SBA-15.

5. Efficient Referencing of FSLG CPMAS HETCOR Spectra using 2D ^{1}H-^{1}H MAS FSLG

5.1. Introduction

The Frequency Switched Lee Goldberg CPMAS Heteronuclear correlation (FSLG CPMAS HETCOR) experiment is employed to obtain correlations between a proton and a X nucleus as e.g. ^{29}Si or ^{13}C [55]. The FSLG CPMAS HETCOR experiment provides structural information based on dipolar interactions, which are of utmost importance for NMR crystallographic studies [177-182]. In this technique, ^{1}H chemical shifts are depicted in the indirect dimension (vertical axis) and the chemical shift of the heteronucleus X is depicted in the direct dimension (horizontal axis). The concept of direct dimension is simple as it is directly measured spectra. However, the concept of indirect dimension is based on indirectly obtaining the information from the modulation of the peaks of the directly measured spectra. A special situation arises for FSLG CPMAS HETCOR techniques, since the protons evolve under an effective field, which is aligned in the direction of the magic angle, while the X nucleus is measured under the static magnetic field. Since the protons are measured in the effective field, this causes a scaling which depends very strongly on the experimental parameters. These aberrations in chemical shift information are misleading and may cause a misinterpretation of the obtained data. Such situation can be corrected in cases where more than one peak appears in the proton dimension of FSLG CPMAS HETCOR, which can be rescaled with the chemical shift value obtained from 1D ^{1}H MAS NMR. The situation is complicated when there is only a single peak in the proton dimension of the FSLG CPMAS HETCOR or if the 1D ^{1}H MAS NMR spectrum has a poor resolution. In such cases finding out the exact chemical shift is a big challenge. This scenario is made even more complicated when the system contains different types of functional groups with very similar chemical shifts. In this case, a broad correlation peak is obtained, and due to insufficient resolution, peak assignment is impossible. We encountered such a situation while performing our experiments for chapter four, 'Mixtures of Alcohols and Water confined in Mesoporous Silica' [24], where the internal referencing approach was used to tackle this problem and to reference the ^{1}H and ^{29}Si dimensions in the FSLG CPMAS HETCOR spectra. Since the internal referencing method involves the addition of another compound (in our case TSP) there is a high probability that this compound affects the sample and thus the method of internal referencing is less suitable to the experiments.

To find a better technique, we introduce a new experimental approach to reference FSLG CPMAS HETCOR spectra that does not require any additional standard compound and thus side effects can be avoided. The new approach can be applied to various systems and works

excellent on all kind of spectrometers. This approach involves first acquiring a ^{1}H-^{1}H MAS FSLG spectrum of the sample, which provides proton chemical shifts on both the direct and indirect dimension. With this information the proton indirect dimension can be referenced since the ^{1}H-^{1}H MAS FSLG spectrum shows diagonal peaks between proton-proton. The approach was then applied and tested to a sample investigated in chapter four consisting of octanol-1 in porous SBA-15.

5.2. Methodology

5.2.1. Pulse Sequence of ^{1}H-^{1}H MAS FSLG

To perform a ^{1}H-^{1}H MAS FSLG spectrum a special pulse program was designed, which was derived from the FSLG CPMAS HETCOR pulse sequence. In this sequence the X channel and the heteronuclear decoupling was removed to obtain a proton spectrum that has evolved under homonuclear FSLG decoupling as shown in Figure 5.1a. In this pulse scheme, first the proton magnetization is aligned in the xy plane through a 90° pulse followed by a 54.7° pulse (pul54) which aligns the ^{1}H magnetization perpendicular to the magic angle. Afterwards, the ^{1}H magnetization is subjected to effective field (FSLG decoupling), which makes the z-component of magnetization aligned at the magic angle. The combined effect is required to average out the proton homonuclear interactions to zero. In the next step, a 35.3° pulse (pul35) is applied to get back the magnetization in the -z direction followed by a z-filter delay (D6). The z-filter was utilized to suppress unwanted coherences and is helpful to study exchange dynamics, which is a different topic and non-relevant for this thesis. The final step involved an application of a 90° pulse in the y-direction to align the magnetic field from the –z direction to the xy plane. The magnetization vector after each pulse in pulse sequence is shown by Figure 5.1b.

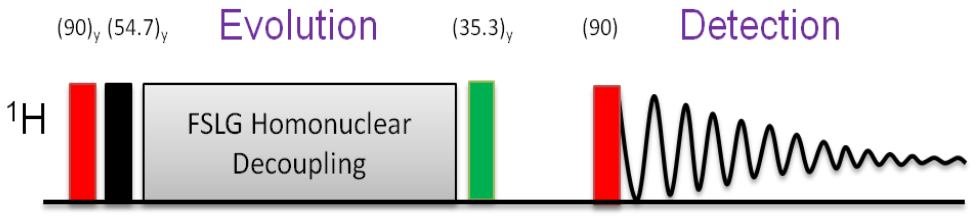

Figure 5.1 (a)The pulse program for the ^{1}H-^{1}H MAS FSLG experiment consisting of a 90° pulse (red), a 54.7° pulse (black) followed by FSLG homonuclear decoupling and a 35.3° pulse (green). The pulse sequence is explained in the text. Reprinted (Adapted) with permission from [183]. Copyright (2019) Springer Nature.

5.3. Experimental section

5.3.1. Sample Preparation

Octanol-1 was purchased from Sigma-Aldrich (>99%) and used without any further purification. The SBA-15 was prepared according to Zhao et al. [173] and characterized using the Brunauer−Emmett−Teller (BET) method as described in our original work [24].

5.3.2. Solid-state NMR Experiments

The 4 mm ZrO_2 rotor was first filled with SBA-15, which was put then under vacuum for overnight to obtain dried SBA-15. In the next step, the dried SBA-15 was mixed with octanol-1 and the sample was put to the spectrometer. All experiments were carried out at room temperature on a Bruker AVANCE III HD spectrometer operating at 14 T corresponding to a frequency of 600.12 MHz for ^{1}H and 119.22 MHz for ^{29}Si. A list of detailed parameters for ^{1}H-^{1}H MAS FSLG and ^{1}H-^{29}Si FSLG PMAS HETCOR experiments is shown below in Table 5.1.

Table 5.1 Table showing the list of experimental parameters employed in ^{1}H-^{1}H MAS FSLG and ^{1}H-^{29}Si FSLG CPMAS HETCOR experiments. Reprinted (adapted) with permission from ref [183]. Copyright (2019) Springer Nature.

Parameters Details	**^{1}H-^{1}H MAS FSLG**	**^{1}H-^{29}Si FSLG CPMAS HETCOR**
Pulse program	Fslg_he	Lghetfq
MAS rate (kHz)	8	8
Number of scans	4	416
Recycle delay D1 (s)	2	2
1H offset frequency (Hz)	-13000	-13000
90˚(1H) pulse length (μs)	3.78	2.5
90˚(1H) pulse power level (kHz)	66	100
Pulse length of 54.7˚	2.17	1.52
Pulse length of 35.3˚	1.40	-
FSLG Homonuclear pulse length-one block (μs)	11.7	11.7
FSLG power level (kHz)	66	66
Proton offset under LG evolution	-4000	-4000
TPPM Heteronuclear pulse length (μs)	-	5.5
TPPM power level (kHz)	-	121
Mixing time (μs)	26.35	26.35
Positive LG offset frequency (CNST 22)	45497.47	45497.47
Negative LG offset frequency (CNST 23)	-53497.47	-53497.47
P15 contact pulse (μs)	-	5000
Z-filter delay (μs)	2000	-

5.4. Results and Discussion

5.4.1. ^{1}H MAS Experiments on SBA-15 with Octanol-1

In the first step, 1D proton spectra at different times were measured to monitor the adsorption of octanol-1 on SBA-15. Different line shapes at different time after preparation of the sample were obtained. This change in line shapes infer that the homogenous spreading of the octanol-1 takes time. Figure 5.2 shows the comparison between the spectrum obtained immediately after sample preparation (Figure 5.2a) vs. the spectrum obtained 18 hours after sample preparation. The difference in line shape of these two spectra points out the dynamic within the system before equilibration. The spectra clearly show aliphatic groups in the range between 0.8 ppm to 3.5 ppm with different kinds of protons, while the small broad signal at 5.0 ppm is probably due to –OH groups of residual water. As discussed in section 4.3.3., it also indicates the presence of an –OH group of octanol-1, which is bonded to the silica surface through hydrogen bonding.

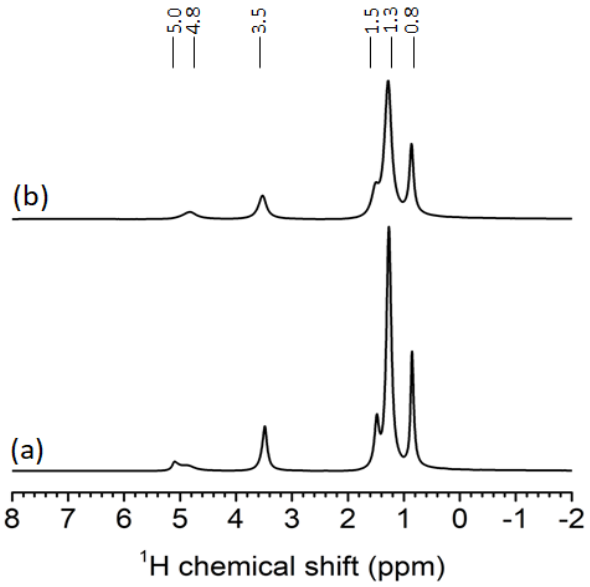

^{1}H attached to carbon (1-8)	^{1}H chemical shift (ppm)
C1:H_2	3.5
C2-C3:H_2	1.5
C4-C7: H_2	1.3
C8: H_3	0.8
-OH from water	5.0

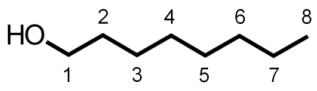

Figure 5.2 ^{1}H MAS single pulse spectra of dried SBA-15 mixed with octanol-1 at 8 kHz spinning rate (a) when measurement was performed immediately after adding the octanol-1 to dried SBA-15, (b) when measurement was performed after a waiting time of 18 hours.

5.4.2. ^{1}H-^{1}H MAS FSLG Experiment on SBA-15 with Octanol-1

In the next step of analysis, the ^{1}H-^{1}H MAS FSLG spectrum of the sample containing SBA-15 with octanol-1 was measured using the pulse program described in Figure 5.1a. The obtained spectrum is shown below in Figure 5.3, which provides very high-resolution spectra of the

system able to detect various types of protons. The spectrum shows diagonal peaks centered at 1.3 ppm, 3.5 ppm and 5.0 ppm together with cross peaks. For 1D data it can be deduced that the peak at 5.0 ppm is related to the presence of hydroxyl groups associated with residual water molecules present in the sample. The peaks centered at 1.3-1.5 ppm and 3.5 ppm are associated with aliphatic protons. The peak at 3.5 ppm is caused by the methylene protons of $–CH_2$-OH groups. The broad peak that appeared at 1.3-1.5 ppm can be assigned to protons attached to C2-C7 (theoretically C2-C3: 1.5 ppm and C4-C7: 1.3 ppm). Since the resolution in our spectrum does not allow us to distinguish at the scale of 0.1 ppm a combined broad peak at 1.3-1.5 ppm is observed instead. The peak at 0.8 ppm corresponds to protons of the methyl group ($-CH_3$) as shown in the 1D proton spectrum (Figure 5.2). About the cross peaks present in the spectrum, we assume that they can be explained by exchange processes between various types of protons present in the system. Detailed analysis of exchange processes is beyond the scope of this thesis. Some preliminary insights are provided in the outlook section in chapter eight.

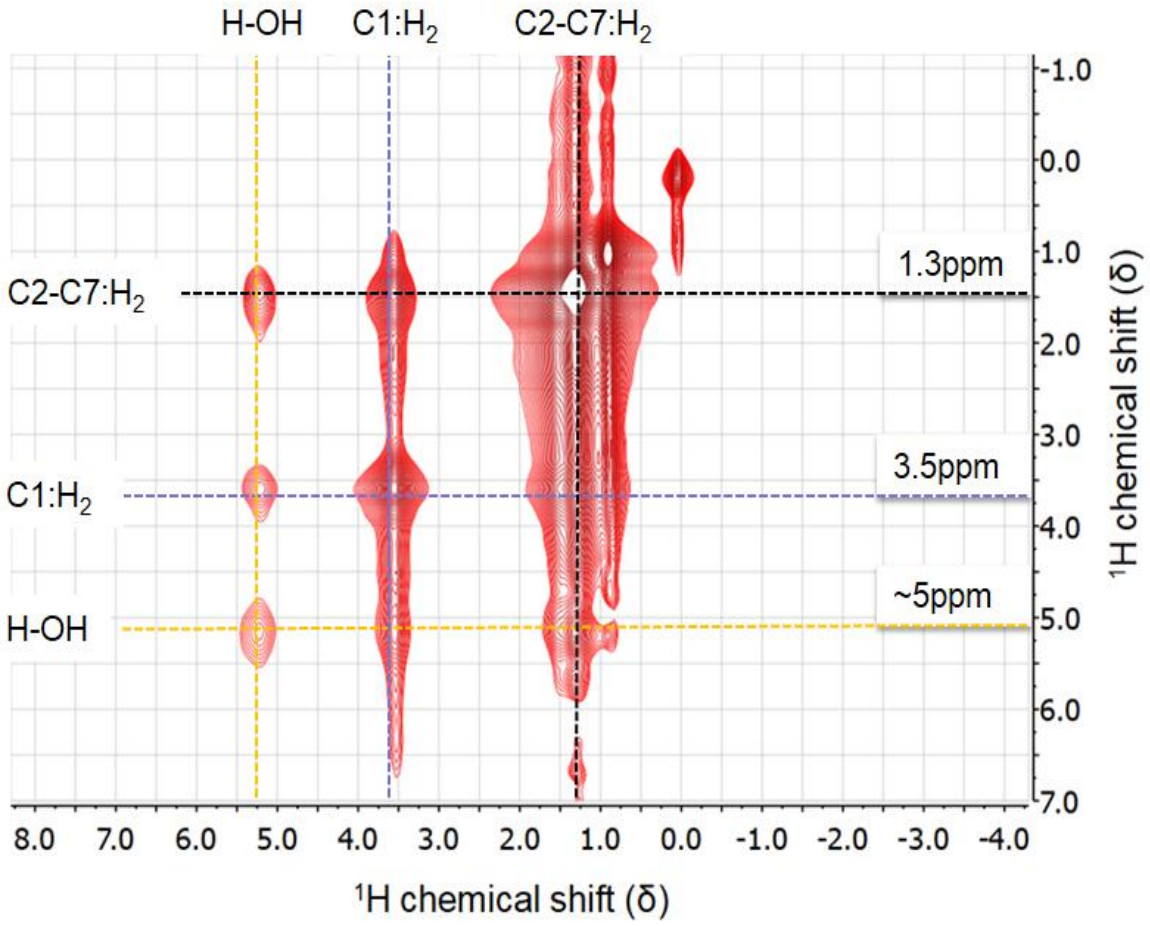

Figure 5.3 ^{1}H-^{1}H MAS FSLG spectrum of SBA-15 with octanol-1 measured at a spinning rate of 8 kHz with z-filter delay of 20 ms.

5.4.3. Referencing the ^{1}H-^{29}Si FSLG CPMAS HETCOR spectrum of SBA-15 with Octanol-1

With the help of the ^{1}H-^{1}H MAS FSLG data, it is now possible to reference the proton dimension (indirect) in the ^{1}H-^{29}Si FSLG HETCOR spectrum (Figure 5.4). This method works excellent when both experiments ^{1}H-^{1}H FSLG and ^{1}H-^{29}Si FSLG CPMAS HETCOR are performed under the same conditions including the use of the same acquisition parameters (as shown in Table 5.1) and the same wobbling settings (tuning and matching). A small change in these parameters can change the value of the chemical shift at a significant level and lead to an inconsistent results. Thus, performing the spectra under the same experimental conditions is crucial. This method was tested for various temperatures in the range of 250 K – 320 K (not shown) and it was observed that the approach is independent of temperature and works excellent in a wide temperature range.

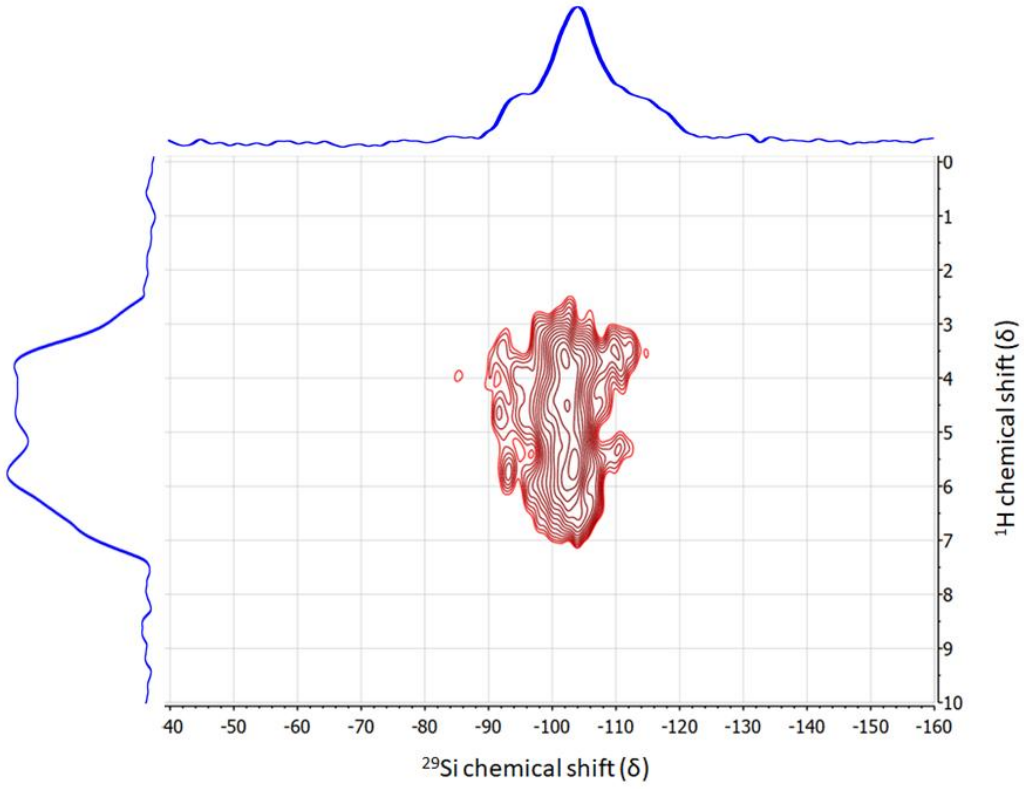

Figure 5.4 ^{1}H-^{29}Si FSLG CPMAS HETCOR spectra of SBA-15 with octanol-1 recorded with the same parameters as the ^{1}H-^{1}H MAS FSLG spectrum in Figure 5.3. The ^{1}H indirect dimension is referenced according to the ^{1}H-^{1}H MAS FSLG spectrum.

5.4.4. General Procedure for Referencing ^{1}H-X FSLG CPMAS HETCOR Spectra

The procedure for referencing the indirect dimension of ^{1}H-X FSLG CPMAS HETCOR is explained as follows.

(i) In the first step, the one dimensional ^{1}H MAS and ^{1}H-X CPMAS spectra of standard samples ^{1}H (TSP), ^{29}Si (TSP), ^{13}C (adamantane) etc. are measured and referenced according to their chemical shift values. The corresponding SR values are noted as SR(^{1}H) and SR(X).

(ii) In the second step, the ^{1}H-^{1}H MAS FSLG of the sample of interest is measured and the ^{1}H direct (horizontal) dimension is referenced according to the SR(^{1}H) value obtained from the ^{1}H MAS spectrum of TSP recorded in (i). The new proton chemical shifts in the direct dimension are denoted by X_1 and X_2 (Figure 5.5).

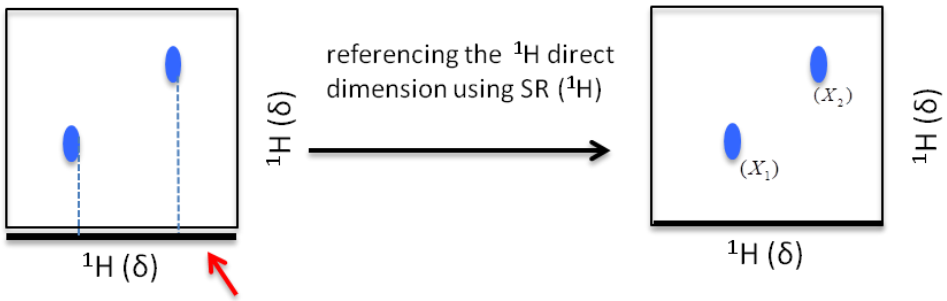

Figure 5.5 Exemplary scheme to reference the proton direct dimension of the ^{1}H-^{1}H MAS FSLG experiment.

(iii) The third step is the referencing of the indirect (vertical) dimension of the ^{1}H-^{1}H MAS FSLG spectrum by selecting a well-resolved diagonal peak and setting the spectrum calibration frequency F2(ppm) = F1(ppm) or X=Y coordinate for the selected peak (Figure 5.6). After setting the correct ppm value of the peak, the SR value of ^{1}H in the indirect dimension is noted as SR(^{1}Hi), which is then helpful to reference the indirect proton dimension of the ^{1}H-X FSLG HETCOR spectrum in the next step.

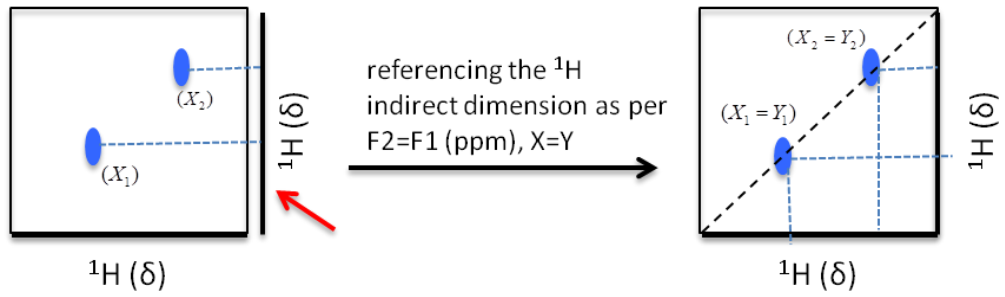

Figure 5.6 Exemplary scheme to reference the proton indirect (vertical) dimension of the ^{1}H-^{1}H MAS FSLG experiment.

Note: The scaling factor of the indirect axis is determined by reading out the shift values of the peak with the lowest and highest chemical shift and by correcting the scaling factor accordingly until all shift values coincide. In our case, the scaling factor was inbuilt within the pulse sequence and thus automatically calculated by the pulse program and within the spectral resolution, we did not find significant deviations from the theoretical scaling factor. The method works perfectly even in case of one peak.

(iv) In the fourth step, the ^{1}H-X FSLG HETCOR spectrum of the sample is measured. The direct dimension (X) is referenced according to the SR(X) value obtained in (i). The indirect proton dimension of the ^{1}H-^{29}Si FSLG HETCOR is referenced according to SR(^{1}Hi) obtained in (iii). The ^{1}H-X FSLG HETCOR spectrum is shown below whose X and ^{1}H indirect dimension both were referenced according to the method described.

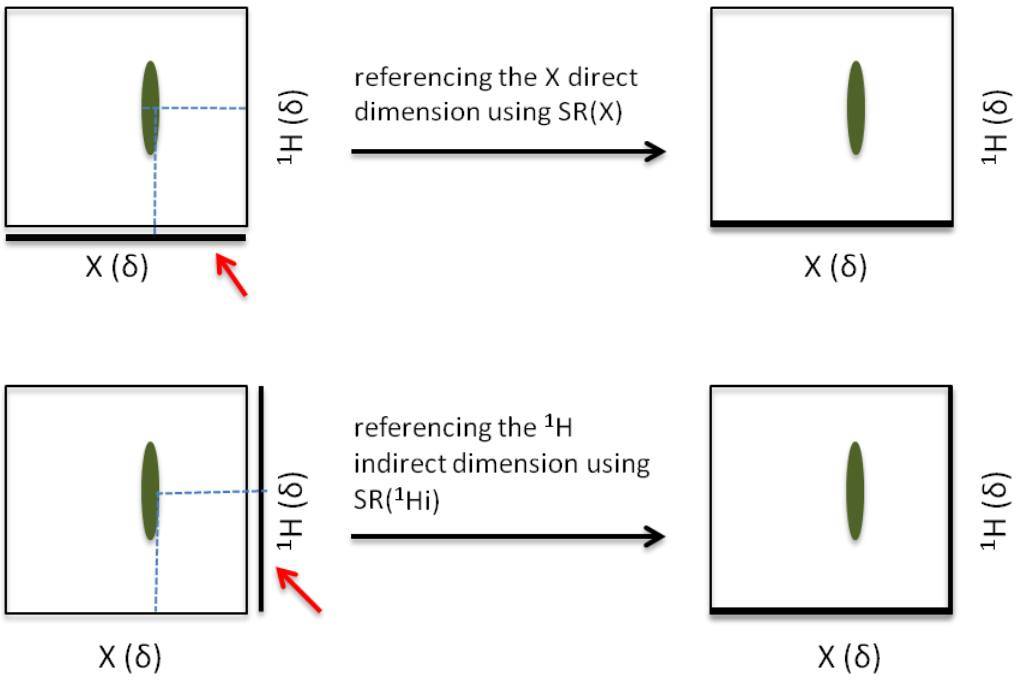

Figure 5.7 Exemplary scheme to reference the ^{1}H and ^{29}Si dimension of ^{1}H-X FLSG HETCOR.

5.5. Conclusions

In this chapter, we highlighted the problem of referencing the proton indirect dimension in case of ^{1}H-X FSLG CPMAS HETCOR and we also provided a novel approach to reference it. The method introduced is easy and also protects the sample under study from being contaminated by an internal reference sample. The approach appears to be independent of the sample type and temperature. The ingenious method not only provides excellent referencing information but also gives high resolution spectra to distinguish various types of protons (-OH).

6. DNP enhanced Solid-state NMR Study to Characterize the Surface of Silica Coated Polycarbonate Membranes

6.1. Introduction

Polycarbonate (PC) and polyethylene terephthalate (PET) are commonly used plastics worldwide. PC has widespread application in electronic components, data storage devices, security devices, medical applications, aircraft and railway components, while PET is widely used in drinking bottles production [184-186]. In academia, porous PC and PET are useful materials for studies in various emerging fields such as nanofluidic or in the development of sensing nanodevices [187]. Porous structures in PC or PET can be created by etching of ion tracks, which results in porous membranes with tuneable pore size [188]. Such membranes exhibit diverse functionalities and have been recently used in nano wire synthesis [189, 190], ion current gating and ion adsorption [191, 192]. Polymer membranes [193] can be further tuned by surface modification. An important approach is the use of Atomic Layer Deposition (ALD), which leads to surface sites on the polymers with flexible compositions, for example, SiO_2, Al_2O_3, TiO_2. This process enables the tuning of pore diameter and aspect ratio [194] and allows to regulate the depth of the layer and thus to control the hydrophilicity of the membrane by adjusting the quantity of ALD cycles [195]. Finally, in the case of thin silica ALD deposition, there is a feasibility to bind organic functional groups to its silanol free sites by using a post grafting approach.

The goals is to find a method which provides the evidence for the functionalization in the pores and to differentiate between a covalent binding or just the solely presence of a functionalization group. In principle, such studies can be done through vibrational spectroscopy, which is usually utilized to determine molecular structures and to identify functional groups. However, the fingerprint region in vibrational spectra of multicomponent materials is often too crowded to distinguish between peaks. Moreover, the analysis of this region cannot be relied on overlapping peaks. Thus, a better technique is required, which enables the separation of peaks, and contains the necessary resolution and sensitivity to detect surface functional groups. Solid-state NMR is one of the techniques, which gives resolved spectra and provides a characteristic chemical shift for different functional groups. Furthermore, it is helpful to analyse multicomponent materials since it is sensitive to individual nuclei. However, solid-state NMR experiences low sensitivity, which makes it limited to the systems having high specific surface areas (>30 m^2/g), such as mesoporous silica like SBA and MCM type materials [196-200].

To overcome this limitation, DNP combined with solid-state NMR has been introduced for such systems by the works of Emsley and Lesage, who obtained significant sensitivity enhancement for nuclei in surface sites of silica materials [84, 91]. This solid-state DNP NMR approach maintains the balance between the resolution and sensitivity and provides a reliable structural information for multicomponent materials, such as silica materials functionalized with inorganic or organic groups which formerly suffered from sensitivity limitations of solid-state NMR[26-28, 86, 92, 155, 201-215]. The aim of this part of the thesis is to apply the DNP enhanced solid-state NMR approach to investigate the surface modification of ion-etched membrane coated with SiO_2 layer, which would not be feasible with traditional solid-state NMR technique because of its limitation to low sensitivity. As discussed, the model system for our experiment consist of SiO_2 coated etched ion-track membranes, which are further modified with amino end functionalized silanes such as APTES (3-aminopropyltriethoxy silane) and APDMS (3-aminopropyldimethyl silane) [216]. Due to the presence of a dense silica coating after ALD, it is expected to observe changes in the ^{1}H-^{29}Si CPMAS spectra depending on the functionalization of the silica layer coated PC membrane.

6.2. Experimental Details

6.2.1. Preparation of ion etched polycarbonate membranes

The ion etched PC membranes were produced by the group of Prof. Trautmann by swift heavy ion irradiation at the UNILAC accelerator of the Helmholtz Center for Heavy Ion Research followed by chemical etching. In their preparation Gold (Au) ions were shot on the bisphenol-A based polycarbonate with energies of approximately 2 GeV, which was done in four sequential irradiation steps under 45 degrees incident angle. Each step was done immediately after another by rotating the foil by 90 degrees which allowed the foil to get irradiation from all directions. The process resulted into pores of 95 nm diameter [217]. Details on the process with explanation of each step are given in the original work [30].

6.2.2. Silica Coating using Atomic Layer Deposition (ALD)

The coating of the PC foil with silica (SiO_2) was performed in a parallel project by the group of Prof. Hess (TU Darmstadt)). They performed the deposition of the silica layer by employing a stainless steel ALD reactor operating at 1.33 torr pressure with the help of $SiCl_4$ and water at a temperature of 60˚C. The detailed procedure on the process can be found in the original work given in ref [30]. In our project, a deposition of 5 nm of silica was applied.

6.2.3.Functionalization with APDMS & APTES

The functionalization of the SiO_2 coated PC foils was performed by the group of Prof. Andrieu-Brunsen (TU Darmstadt). For achieving the APDMS binding, typically they immersed the polycarbonate foil coated with silica in an absolute ethanolic solution of APDMS. This process was carried out in a flame-dried nitrogen flushed Schlenk flask at a temperature of 60˚C for one hour. The unreacted APDMS was later extracted.

For achieving the APTES binding, typically they prepared a 14 nmol ethanol solution by dissolving 3.3 ul APTES in 40 ml of ethanol in a flame dried nitrogen flushed Schlenk flask. The solution was then heated to 70˚C and the PC foil coated with SiO_2 was kept immersed in the solution for 2 hours. The foil was further processed under the thermal treatment for another one hour at 70˚C followed by membrane extraction in ethanol for 15 min and dried at ambient conditions.

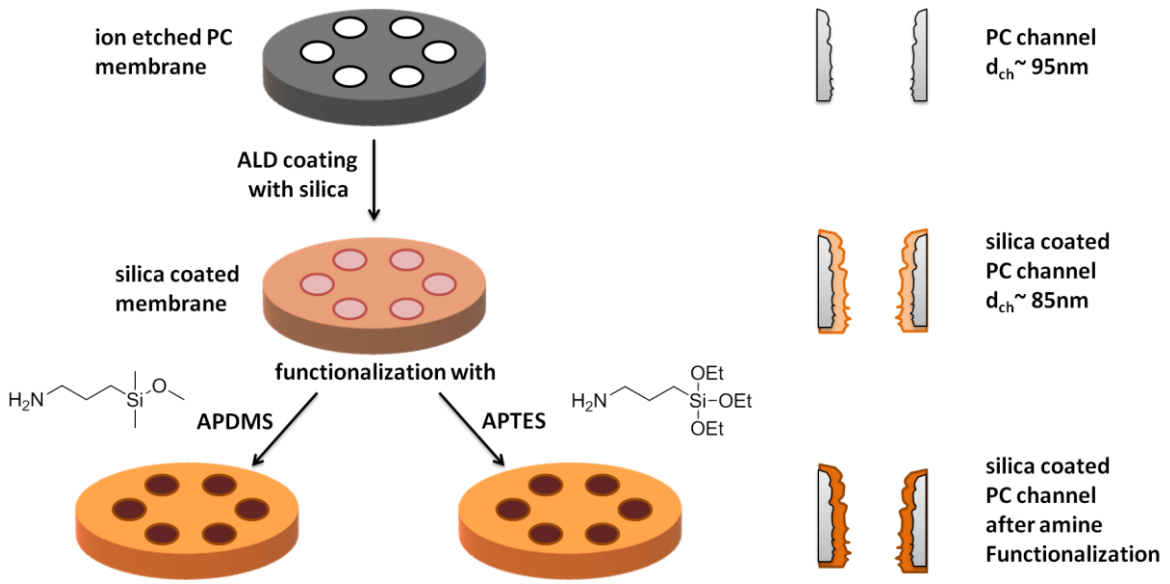

Scheme 6.1 Exemplary model of the steps performed to prepare amine functionalized silica coated porous membranes. Adapted from ref [30] .

6.2.4.Atomic Force Microscopy (AFM) & Scanning Electron Microscopy (SEM)

The AFM measurements were carried out on a Dimension Icon (Brucker, Billerica, MA, USA) by the group of Prof. Stark (TU Darmstadt). They obtained the images in peak force tapping mode having a nominal force constant of 0.7 nN and a nominal resonance frequency of 150 kHz in air with the maximum force 2 nN. The scanning electron micrographs were performed by the group of Prof. Trautmann (TU Darmstadt) who employed a Philips XL30 FEG high

resolution scanning electron microscope. The details on these experiments can be found in our original work in ref [30].

6.2.5. Sample Preparation for DNP SENS Experiments

Since the Polymer foil was a thin circular like disc, it was challenging to put it into the rotor in its original form, thus the film was cut into small pieces. The small pieces were wetted with radical solution and filled into the rotor. For this kind of sample, 15 mM AMUPol in glycerol-d_8/D_2O/H_2O was used which was prepared as follows:

Table 6.1 Sample preparation of the 15mM AMUPol matrix in in glycerol-d_8/D_2O/H_2O.

Radical matrices	**Preparation of radical matrix**
15 mM AMUPol in glycerol-d_8/D_2O/H_2O	AMUPol - 2.72 mg Glycerol- d_8 - 150 μl D_2O - 75 μl H_2O - 25 μl

6.2.6. DNP SENS Experiments

All DNP solid-state NMR experiments were performed on the Bruker Ascend 400 DNP AVANCE III spectrometer connected with a 9.7 T Bruker gyrotron operating at a microwave frequency of 263 GHz. The spectrometer was equipped with a low temperature, 3.2 mm triple resonance probe operating at channels ^{1}H/X/Y. Spectra were recorded at frequencies of 400.25 MHz for ^{1}H, 100.58 MHz for ^{13}C and 79.48 MHz for ^{29}Si, respectively, at nominally 100 K and at a typical spinning rate of 8 kHz. Some of the experiments were performed at 9 or 10 kHz, to check for spinning side bands. The ^{1}H-^{13}C CPMAS and ^{1}H-^{29}Si CPMAS experiments were performed using contact times of 2 and 3 ms, respectively. The recycle delay (D1) was chosen as 1.3 times T_1 where T_1 is the built-up time calculated for the ^{1}H MAS saturation recovery experiment obtained with MW on. During the data acquisition, TPPM 15 [46] and SPINAL64 [47, 121] were employed for ^{1}H-^{13}C CPMAS and ^{1}H-^{29}Si CPMAS, respectively. All spectra were referenced according to standard reference samples. TSP was used to reference ^{1}H and ^{29}Si spectra (0 ppm for both), while ^{13}C-^{15}N glycine in 20 mM TOTAPOL in glycerol-d_8/D_2O/H_2O (60/30/10 w/w/w) was used to reference ^{13}C spectra (176. 5ppm).

6.3. Results and Discussion

6.3.1.Atomic Force Microscopy

The surface of the etched ion track foils was studied by Atomic Force Microscopy (AFM) by the group of Prof. Stark (TU Darmstadt). This technique is very useful to image the surface profile of the system after each modification step, which is depicted in Scheme 6.1. The fresh polycarbonate foil without any treatment is illustrated in Figure 6.1a. The image after further modification by silica coating and binding of linkers are shown in Figure 6.1b, c, respectively. The comparison of these images with the progress of modification shows that the pores and the morphology stay untouched, which points out the stability of the system. However, the comparative analysis of pore diameters based on these images shows a decrease of the pore size after the silica coating, which is also observed after the binding of linker to the surface. These observations provide an evidence for the successful ALD layering as well as an indication of the linker functionalization. The calculated pore diameter values of the polycarbonate foil from AFM images is further subjected to a correction due to the well-known influence of the AFM tip size. The AFM tip size is approximated to be of size 20 nm hence, a value of 20 nm is added to the calculated foil diameter.

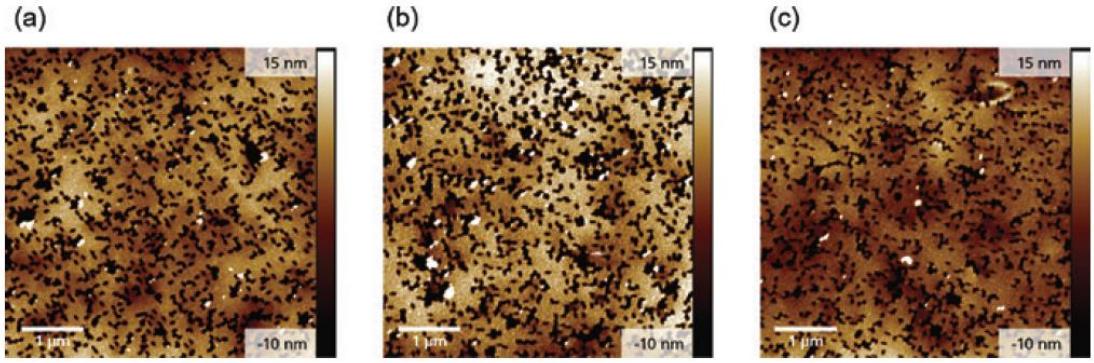

Figure 6.1 AFM recorded images of the PC membranes after each modification step: (a) ion etched polycarbonate membrane, (b) SiO_2 coated membrane and (c) APTES functionalized SiO_2 coated membrane. Reproduced with permission of de Gruyter in the format Thesis/Dissertation via Copyright Clearance Center from ref [30].

6.3.2. ^{1}H-^{29}Si CPMAS DNP SENS

The feasibility of DNP-SENS to enhance the signal sensitivity was tested on the silica coated PC foil after impregnation with 15 mM AMUPol in glycerol-d_8/D_2O/H_2O by performing ^{1}H-^{29}Si CPMAS experiments with MW on and MW off. By comparison of the MW on and the MW off spectrum, an enhancement factor of 7.0±3.3 was calculated from Figure 6.2a, b. In addition,

the MW on spectrum provides high resolution data that allows to analyse surface sites. Figure 6.2b shows a broad signal centred around -105 ppm, which is considered as the range for Q_n groups [218]. After deconvolution of the spectrum, distinguished peaks for Q_2, Q_3 and Q_4 can be seen at -99 ppm, -104 ppm, and -112 ppm in Figure 6.2b', representing the binding sites in the silica layer.

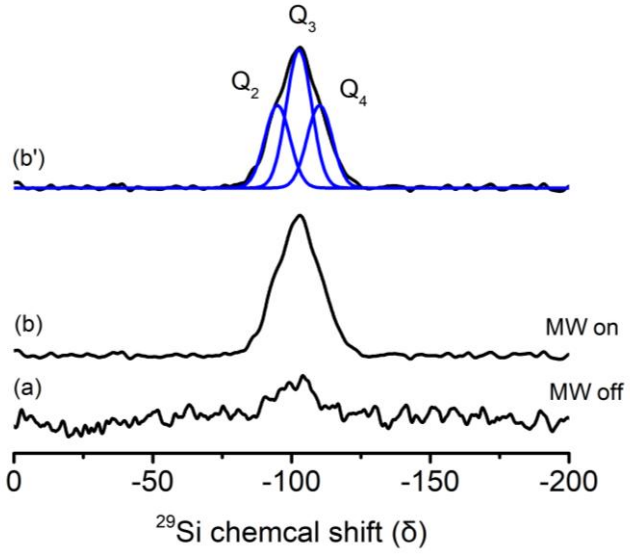

Figure 6.2 ^{1}H-^{29}Si CPMAS spectra measured at 8KHz spinning rate at 110K of the ALD coated polymer foils: (a) with MW off, (b) with MW on to determine the signal enhancement factors. (b') The deconvolution of the spectrum (b) employing Lorentzian-Guassian lines. Adapted from ref [30].

Surprisingly, the enhancement factor of 7.0±3.3 obtained for Q_n groups is less than the enhancement factor achieved for glycerol-d_8 of the solvent matrix as well as the expected signal enhancement (approx. 50) obtained for DNP enhanced ^{1}H-^{29}Si CPMAS of porous materials [202, 208]. This can be understood by a more detailed analysis of the ALD coating process. This process most probably generates silicon containing defect sites in the bulk of the 5 nm silica layer. These defect sites contain –OH groups with them. These sites however are not hyperpolarized but they generate a thermal signal, which contributes to the signal intensity even in the MW off spectrum. This phenomenon is illustrated by the MW off spectrum (Figure 6.2a), which shows significant signals of Q_2 and Q_3. The strong intensity of these signals suggests that they are related to silicon containing defect sites in the bulk and not only to surface near sites, because the amount of Si-OH sites belonging to the surface is assumed to be lower than the detection limit of solid-state NMR in case of small surface areas as present in the membrane system. As a result, the enhancement factor, which is dominated

by surface near sites, calculated from the ^{1}H-^{29}Si CPMAS spectra is lower than the expected signal enhancement factor.

In the next step, the pore wall modification with linker molecules is investigated using ^{1}H-^{29}Si CPMAS (Figure 6.3a- APDMS; 6.2b-APTES). First, the sample modified with the APDMS linker was analysed as it has the capability to form only one bond with the silica layer, which can be detected in the ^{1}H-^{29}Si CPMAS spectra. From (Figure 6.3a'), it can be seen that Q_n groups are present in the expected range around -105 ppm. An additional signal has also appeared between 5 and 20 ppm; which after deconvolution shows two separate signals centered at 7 and 15ppm (Figure 6.3a"). To understand these signals, it is important to perform the same set of experiments on free APDMS to know the chemical shift value of the free linker. Figure 6.3a shows the spectrum of free APDMS, in which a signal has appeared at chemical shifts of 6 and 17 ppm, which are typically known for M_1 groups [219]. The chemical structure of M_1 group is shown in Figure 6.4. The comparison of the spectra of the free APDMS linker Figure 6.3a and of the APDMS functionalized silica layer (Figure 6.3a') indicates small chemical shift difference, however, a significant broadening in the signal linewidth is observed between the two sets of experiments. This difference strongly indicates the possibility that during the chemical reaction, some of the APDMS linker got adsorbed on the silica surface or encapsulated in the pore structure of the SiO_2 coated ion etched polycarbonate membrane. There is also a possibility that some of the free APDMS linkers do not participate in the chemical reaction and stay free, while others are engaged in a covalent bonding with the silica surface.

In the second set of spectra, the modification with the APTES linker was investigated. From Figure 6.3b", it can be seen that an additional signal between -50 and -75 ppm has appeared, which is the characteristic chemical shift range for T_n groups. The chemical structures of T_n groups are shown in Figure 6.4. This indicates the successful functionalization of APTES on the silica layer on the ion etched polycarbonate membrane. This hypothesis is further supported by the chemical shift value, which is shifted to lower ppm value in case of bonded APTES as compared to the free APTES (approx. -47ppm, Figure 6.3b).

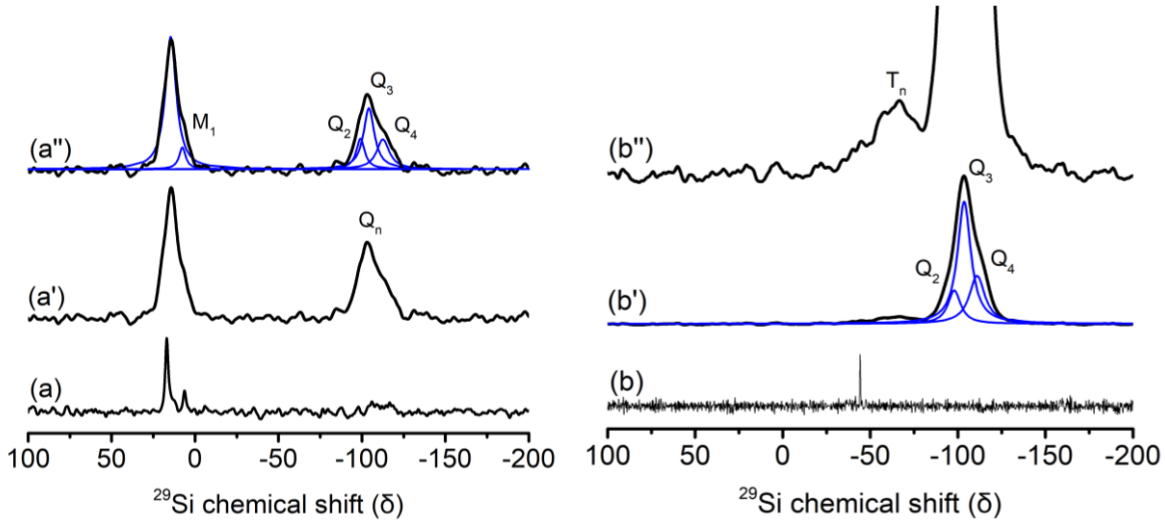

Figure 6.3 Static ^{29}Si NMR spectra of the free linkers (a) APDMS and (b) APTES at room temperature. ^{1}H-^{29}Si CPMAS spectra of the ALD coated PC foil functionalized with: (a') APDMS and (b') APTES measured at 8 kHz spinning rate, nominally at 110 K with MW on. Spectra (a'') and (b'') show the deconvolution of spectra (a') and (b'), respectively. Note: The deconvolution was done using Lorentzian-Gaussian lines. Both samples were impregnated with 15 mM AMUPol in glycerol-d_8/D_2O/H_2O. Adapted from ref [30].

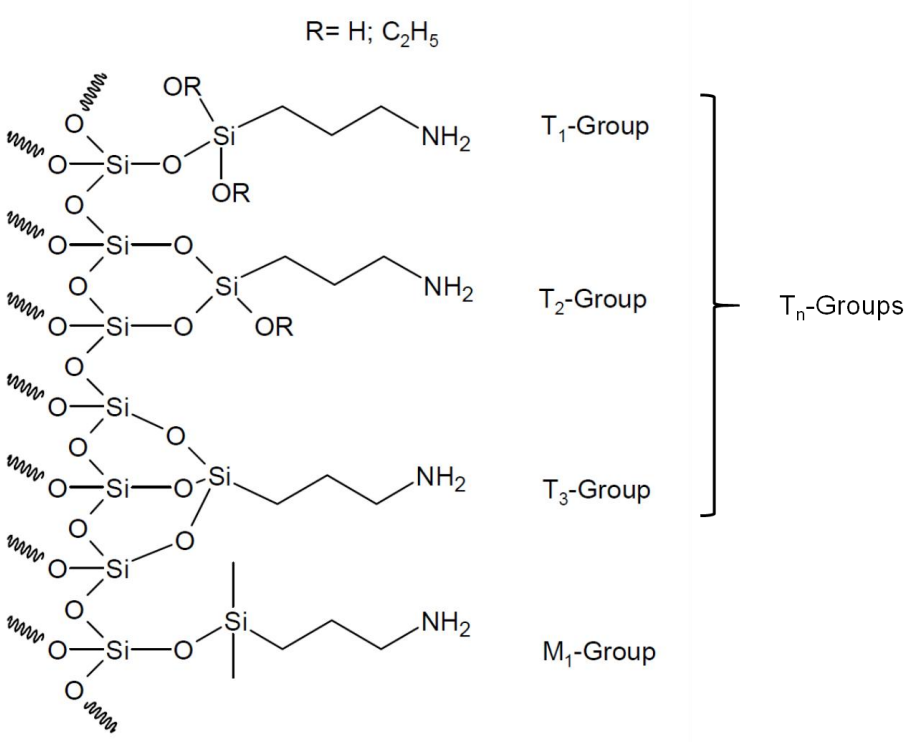

Figure 6.4 The chemical structures of the M_1 and T_n groups when covalently grafted on surfaces. Reproduced with permission of de Gruyter in the format Thesis/Dissertation via Copyright Clearance Center from ref [30].

6.3.3. ^{1}H-^{13}C CPMAS DNP-SENS

The same set of experiments was also repeated for ^{13}C nuclei. Firstly, it was verified that the DNP NMR technique is suitable to measure ^{13}C nuclei in case of ion etched polycarbonate membranes. This was confirmed by comparing the signal intensity in the ^{1}H-^{13}C CPMAS spectra of the silica coated ion etched polycarbonate membrane measured with MW on with MW off (Figure 6.5). This comparison showed that the enhancement factor varies for different functional groups present in the system. The comparison between the ^{1}H-^{13}C CPMAS spectry obtained with MW on and MW off provides a significant signal enhancement for the two signals at ca. 65 ppm and 80 ppm corresponding to glycerol-d_8 of the solvent matrix. Furthermore, a signal at 120-135 ppm is observed with an insignificant enhancement factor of 1.8±0.1, which is attributed to the aromatic groups of the PC foil. The huge difference in the signal enhancement factor for the functional groups of the polymer foil and the solvent is most probably related to the inefficient polarization transfer between solvent matrix and PC foil. This can be understood by the presence of the silica layer, which restricts the proton-proton spin diffusion leading to an inefficient polarization transfer to the PC foil's functional groups. The strong signal enhancement of the glycerol-d_8 is related to the efficient polarization transfer from the radical to the surrounding protons and then via ^{1}H-^{1}H spin diffusion through the whole solvent matrix.

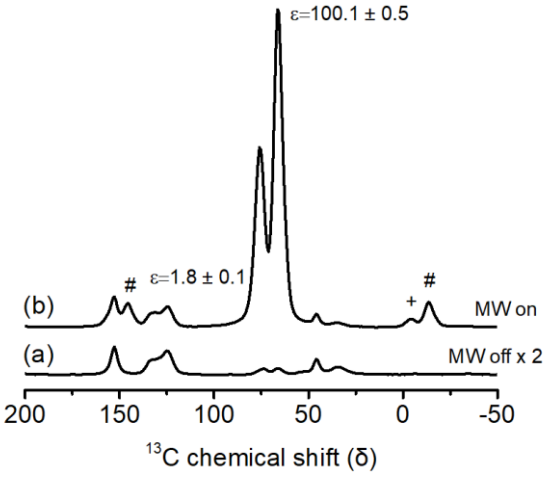

Figure 6.5 ^{1}H-^{13}C CPMAS spectra of the silica coated ion etched polycarbonate membrane, measured at 8 kHz spinning, at nominally 110 K: (a) MW off and (b) MW on spectra to determine the signal enhancement factors. Note: signals marked with + and # represents the sidebands of the signal corresponding to the glycerol. The peak around 160 ppm is a overlapped peak of a signal at 160 ppm with a spinning sideband of glycerol. Signals achieved in the range of 25 and 50 ppm refer to aliphatic groups of the diphenyl-dimethyl-methane molecules, and the signal at 152 ppm corresponds to the carbamate groups occurring in the polycarbonate foil. Adapted from ref[30].

Finally, the ^{13}C CPMAS DNP spectra of the silica coated ion etched polycarbonate membrane were compared before and after the functionalization with APTES and APDMS (Figure 9.3 in appendix). In case of APTES modification, it is surprising to see no additional signals from the APTES linker after surface functionalization, which was expected in region between 0-50 ppm. Hydrolysis of ethoxy groups (18 and 58 ppm) is one of the possible explanations to understand this (Figure 9.3 in appendix), as the hydrolysis of ethoxy groups cause the APTES to bind on the surface of the silica coated membrane. This assumption is supported by the spectrum in Figure 6.3b" where the ^{29}Si signal of the T_n groups shows the maximum at -68 ppm typical for the formation of T_2 or T_3 binding sites. The formation of T_n groups requires the ethoxy hydrolysis, where the degree of hydrolysis grows with increasing n. The signal of the aliphatic chain of the linker molecules on the other hand is not visible. This observation seems to be related to the number of scans (ns) as the ns for the ^{1}H-^{13}C CPMAS DNP-SENS measurement was 16 times less than the ns for the ^{1}H-^{29}Si CPMAS DNP-SENS spectrum and thus, it was beyond the range of detection. In summary, identifying the linker molecule signal in ^{1}H-^{13}C CPMAS is challenging and would require more technical efforts that are beyond the scope of this experiment.

6.3.4. Surface Analysis

With the help of the DNP-SENS technique, the presence of molecular functionalization on the surface of silica coated membrane was confirmed. However, it was also important to confirm that the functionalization with the linker molecules occurs on the pore surface. Thus, a calculation of the ratio of the inner pore surface area to membrane planar area (excluding the inner pore surface) was done based on the AFM data. From this calculation (section 9.1, Appendix), it is observed that the pore surface area is approximately 910 times bigger than the membrane planar area. Taking into account that the overall specific pore surface area of the membrane is 25.16 m^2/g, the membrane planar area is calculated to be 0.027 m^2/g (=25.16/910 m^2/g). This shows that the planar area covers only a negligible amount of the total area, which is not detectable even with DNP. Thus, the obtained signals from the linker functionalization on the surface are believed to arise from functionalization on the inner-pore surface. To support this analysis, SEM micrographs were recorded of the ion etched polycarbonate membrane coated with 20 nm silica layer by ALD (Figure 9.4 in appendix) by the Trautmann group. These SEM images show the significantly larger inner surface area of channels as compared to the planar area, which is in good agreement with the surface analysis discussed above.

6.4. Conclusions

In this chapter, we verified the successful functionalization with linker molecules on the inner pore surface of silica-coated ion etched polycarbonate membranes, which was further validated by quantitative surface analysis together with AFM and SEM data. Hence, we can conclude that the DNP-SENS technique has high potential to study ion etch polycarbonate membrane having low surface area and in future can be very useful to characterise functional ion etched materials.

7. Signal Amplification for Specific Functionalization of Cellulose Paper using DNP-SENS

7.1. Introduction

In recent years, researchers have developed smart surfaces that can alter their physico-chemical properties dynamically [220]. Such "smart surfaces" are the future in material design. An example of a "smart surface" is the combination of paper with functional polymers. Such surfaces are printable, flexible, thin and light-weight. For deeper understanding of the properties and functionalities of such surfaces, it is vital to characterize them on the nanoscale, which is the basic step to optimize such surfaces for their industrial applications. Having a potent control over the properties, for example porosity, chemical stability or thermal endurance, gives them an inherent advantage over regular surfaces for use in the fields of advanced technologies, such as printed electronics, capacitor design, and sensors [13-17]. Alterations in the functionality and wettability of such surfaces can also be achieved making them extremely useful in sensing technology and in the field of microfluidics [221, 222].

The study of functional paper materials using solid-state NMR is challenging due to their (i) complex structure and (ii) low specific surface areas (often below $<<30 m^2/g$). The state-of-the-art solid-state NMR technique can in principle study the complex structures of materials by measuring local interactions, however, in case of functional paper materials the low surface area restricts solid-state NMR to due to its low intrinsic sensitivity. In such cases, DNP enhanced solid-state NMR can be used to overcome this issue as already explained in chapter six for the ion etched membranes. In contrast to IR and Raman spectroscopy, this technique provides information on surface functionalization and various interactions at the molecular scale [221-224]. Although, solid-state NMR is a well-established method to study cellulose materials [223], up to now paper materials are less explored due to their highly complex structure and morphology [224]. Thus there are only few studies in this field where solid-state NMR is used as an analytical tool, for example, to investigate aging processes of historical documents [225-228] or water-paper interactions [229-233]. The extraordinary property of DNP enhanced solid-state NMR allows the selective sensitivity enhancement and provides useful information about the functionalization of surfaces including information about changes occurring at the surface level [202, 205, 234-240]. This technique was demonstrated to be powerful to study expansin proteins and their interactions with cellulose in cell walls [241, 242].

The focus of this chapter is to evaluate DNP enhanced solid-state NMR spectroscopy to study functionalized paper materials. To check the applicability of DNP for characterization of functionalized paper materials, a model system containing cellulose fibers (hydrophilic)

modified with Poly Benzyl Methacrylate (PBEMA) chains was synthesized by the Gallei group (University Saarbrücken). The polymer chain consists of different functionalities such as carbonyl moieties and aromatic groups (hydrophobic), which makes it an interesting candidate for evaluation of DNP experiments. For preparation of the material, the Gallei group employed the "grafting-from" method as it provides dense polymer brushes, whose growing can be controlled by Atom Transfer Radical Polymerization (ATRP).

For DNP studies, the presence of an electron spin source is important to enable the polarization transfer from electron to nuclei. Thus, the model system was impregnated with radical solutions such as AMUPol [88] in aqueous solution. Along with this, the radicals bTbK [28] or TEKPol [95] were also tested by employing TCE as solvent. The different radical solutions vary in their wettability properties (hydrophilic/hydrophobic), which is the key for selective enhancement of different functional groups.

7.2. Experimental Section

7.2.1. Functionalization of Cellulose Fiber

The synthesis of the functionalized paper substrate was performed by Dr. Steffen Vowinkel in the group of Prof. Gallei (University Saarbrücken) following the procedure in literature [243]. According to this procedure, the non-functionalised cellulose fiber was functionalized with 3-(2-bromoisobutyrate)propyl trichlorosilane in argon environment, which acts as initiator for ATRP. In the second step, the cellulose paper featuring the ATRP initiator on the surface was put in a Schlenk tube and dried under vacuum followed by growing BEMA monomers in argon atmosphere. The step by step procedure about the synthesis can be followed from the original work as described in ref [31] and the chemical reaction is provided in Scheme 7.1.

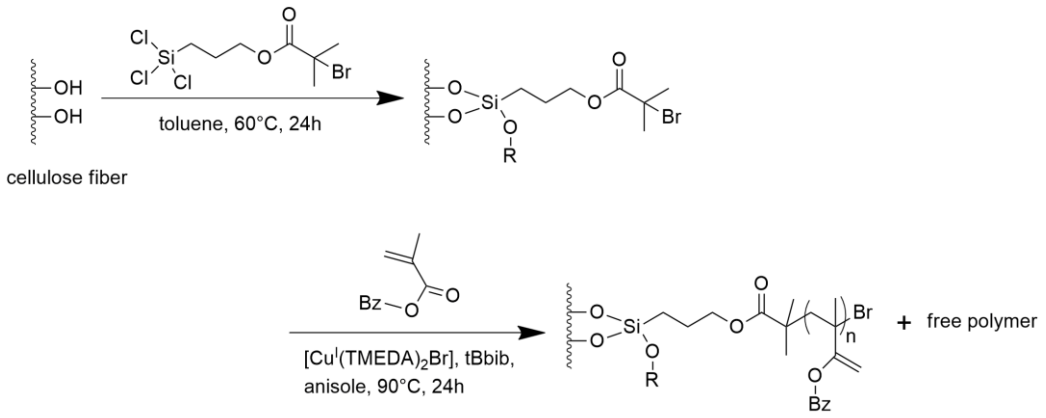

Scheme 7.1 Functionalization of the cellulose with the ATRP initiator followed by grafting of the polymer employing surface-initiated polymerisation of benzyl methacrylate (BEMA). Adapted from ref[31].

7.2.2. Sample Preparation for DNP Measurements

TEKPol, AMUPol and bTbK were purchased from SATT (Aix-Marseille- University). The solvents, D_2O and TCE ($C_2H_2Cl_4$) were purchased from Sigma-Aldrich. All radicals and solvents were utilized without any further modification or purification. The matrix was prepared by dissolving the radicals in the appropriate solvent according to the required molarity as shown in Table 7.1.

Table 7.1 List of radical matrices to be used for DNP sample preparation.

Radical Matrix	**Preparation of radical matrix**
10 mM TEKPol in TCE ($C_2H_2Cl_4$)	TEKpol - 1 mg 1,1,2,2-tetrachloroethane - 176 mg (111 μl)
16 mM bTbK in TCE ($C_2H_2Cl_4$)	bTbK - 1 mg 1,1,2,2-tetrachloroethane - 225 mg (142 μl)
15mM AMUPol in D_2O/H_2O (90:10 v:v %)	AMUpol - 2.72 mg D_2O - 225 μl H_2O - 25 μl

All samples (paper substrate, paper substrate with ATRP linker, and paper substrate functionalized with PBEMA) were cut into small pieces (approximately 20 mg). These pieces of paper were wetted with 15-25 μl of the appropriate radical solutions as given in Table 7.1. Once the solution was fully absorbed by the paper, the wetted pieces were filled into 3.2 mm sapphire rotors with which the DNP experiments were performed.

7.2.3. Solid-state DNP Measurements

All experiments were carried out on a Bruker Avance III 400 spectrometer. The spectrometer is equipped with an Ascend 400 DNP magnet system and a 9.7 T (263 GHz) Bruker gyrotron system. A low temperature ^{1}H/X/Y probe was used and experiments were performed at frequencies of 400.25 MHz for ^{1}H, 100.59 MHz for ^{13}C and 79.48 MHz for ^{29}Si. All spectra were recorded at nominally 110 K and at 8 kHz spinning rate. The CPMAS spectra were obtained for ^{13}C and ^{29}Si with contact times of 2 and 3 ms, respectively. A recycle delay of 1.3 T_1 was used, were T_1 was calculated from ^{1}H MAS saturation recovery experiments performed with microwave irradiation according. The spinal 64 [244] and TPPM 15 [245] decoupling sequences were applied during data acquisition for ^{13}C and ^{29}Si respectively. All spectra were referenced to TMS.

7.3. Results and Discussions

7.3.1. ^{1}H-^{29}Si CPMAS DNP-SENS of Cellulose Fiber with ATRP Initiator

The functionalization of the paper substrate was studied sequentially. A first indication for the successful modification of the paper substrate with ATRP initiator molecules is given by contact angle measurements, which were done by the group of Prof. Gallei. The contact angle determines the hydrophobic and hydrophilic nature of the surface. In general, the larger the contact angle, the stronger the hydrophobicity of the surface and vice versa. The contact angle for the ATRP initiator functionalized paper substrate was measured to be 125±5° (Figure 9.5, in appendix), which suggests its hydrophobic nature. For details on these measurements the reader is referred to the original literature [31].

To further elaborate on structural changes after modification of the paper substrate with the ATRP linker, the system was studied with ^{1}H-^{29}Si CP MAS DNP-NMR. The functionalized paper substrate sample was impregnated with 10 mM TEKPol in TCE. The ^{1}H-^{29}Si CPMAS spectrum of the ATRP functionalised paper substrate is shown in Figure 7.1. In the spectrum, signals between -40 and -70 ppm are clearly visible, which are associated with T_n groups (for chemical structure of T_n, see Figure 9.6, in appendix). After the deconvolution of the spectrum, signals at -40, -55, and -63 ppm can be distinguished which are associated with T_0, T_1 and T_2 respectively [246]. The presence of these signals is attributed to possible binding of the ATRP initiator on the cellulose fiber.

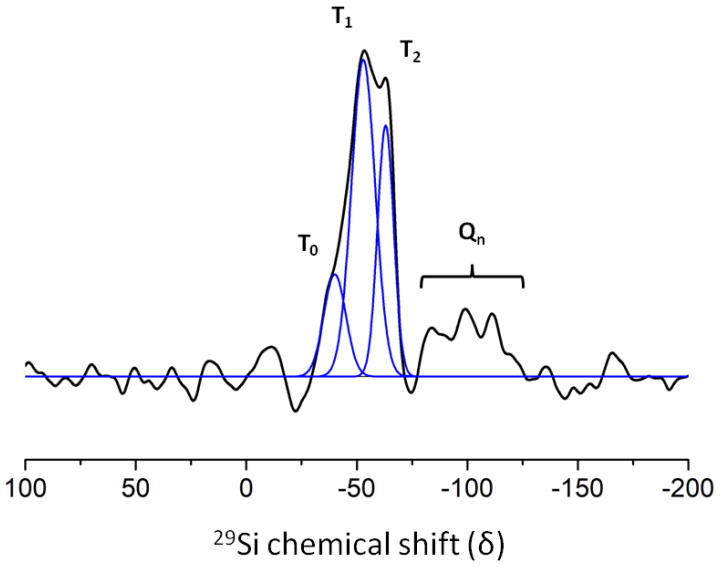

Figure 7.1 ^{1}H-^{29}Si CPMAS spectrum of the paper substrate functionalized with the ATRP initiator measured at 8 kHz spinning rate, with MW on, nominally at 110 K. The sample was impregnated with 10 mM TEKPOL in TCE (hydrophobic matrix). Adapted from ref [31].

Next, it has to be taken into account that hydrolysis of ATRP initiator molecules leads to cross-linking of ATRP molecules, which may also lead to formation of T_n group. Therefore, for comparison the spectrum of the ATRP linker was measured before and after hydrolysis as shown in Figure 7.2. Comparing the spectrum after hydrolysis of the linker (Figure 7.2b) and of the ATRP functionalized paper (Figure 7.1), the lineshape and obtained chemical shift differences in the two spectra show remarkable differences, which evidently illustrates the successful binding of the ATRP linker on the cellulose surface. Interestingly, also Q_n groups (for chemical structure of T_n, see Figure 9.6, in appendix) in the range from -90 to -115 ppm are observed in the two spectra. The presence of Q_n groups indicates $(OH)_{4-n}$-Si-$(O\text{-}Si\text{-})_n$ binding sites. Since such Q_n groups are also present in the spectrum of the free ATRP linker (Figure 7.2a,b), it can be concluded that they are formed during the preparation of the ATRP linker.

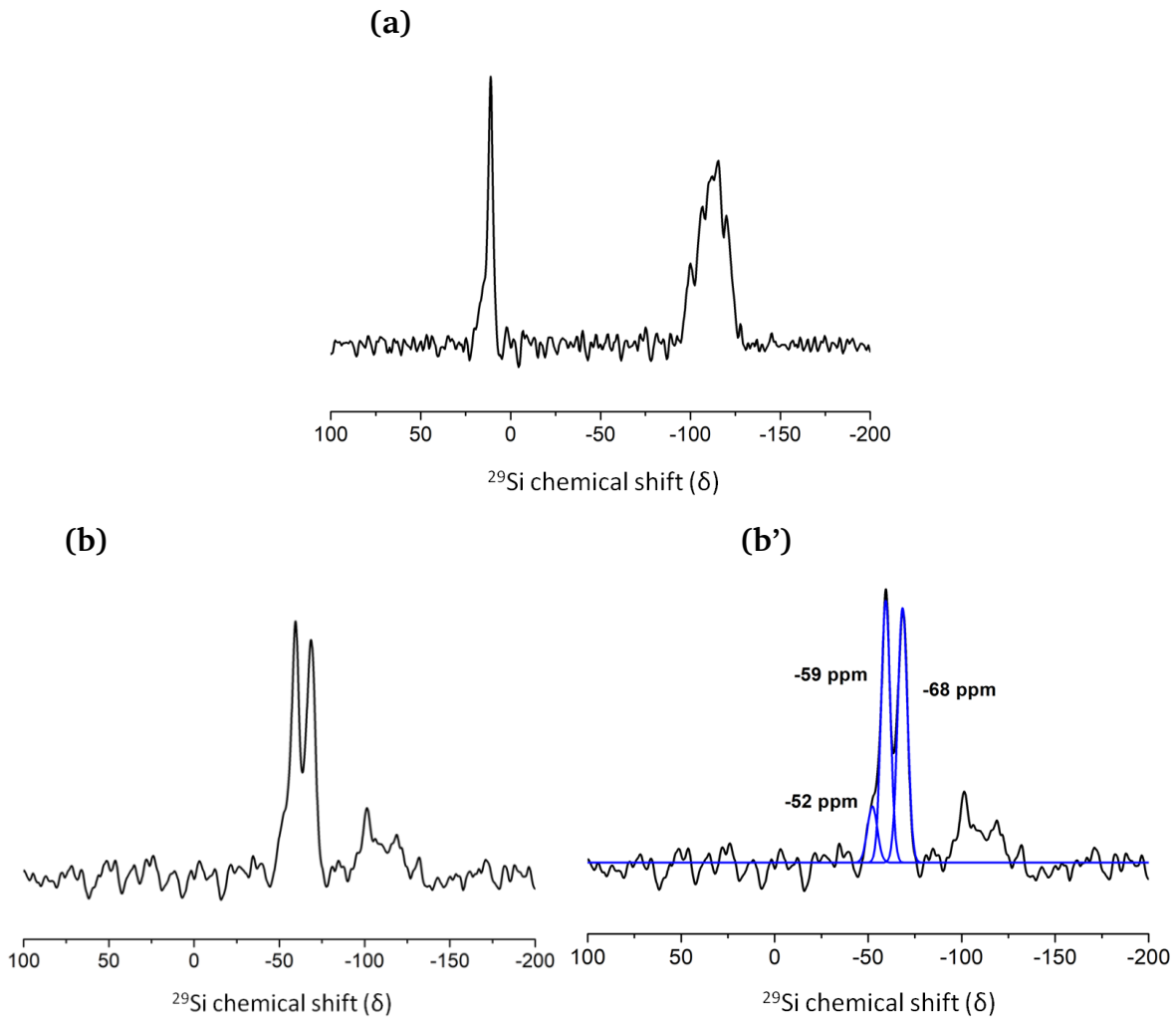

Figure 7.2 (a) ^{1}H-^{29}Si NMR spectrum of the liquid ATRP linker measured under static conditions at 14 T. (b) ^{1}H-^{29}Si CPMAS spectrum of the ATRP linker after the hydrolysis under air, measured at 9.4 T. (b') Deconvolution of the ^{1}H-^{29}Si CPMAS spectrum shown in (b). Adapted from ref [31].

7.3.2. ^{1}H-^{13}C CPMAS DNP-SENS of Cellulose Paper Functionalized with PBEMA

In the second step, benzyl methacrylate (BEMA) was polymerized on the surface of the paper substrate via the ATRP linker using surface initiated polymerization. The evaluation of the hydrophobic or hydrophilic nature of this sample was again performed by the group of Prof. Gallei by measuring the contact angle. The contact angle was found to have changed from 125±5° of the ATRP functionalised paper to 116±8° (Figure 9.5). Since the difference in contact angle is small and is within the error range, no significant change in hydrophobic or hydrophilic properties of the surface can be assumed.

The grafting of PBEMA on the ATRP functionalised paper substrate was then investigated by ^{1}H-^{13}C CPMAS DNP-NMR (Figure 7.3). The PBEMA modified sample was impregnated with a 16 mM bTbK solution in TCE. The spectrum in Figure 7.3a clearly shows one peak at around

132 ppm, which is characteristic to the aromatic group and another peak at around 180 ppm for the carbonyl group, which appeared after the grafting of PBEMA. These signals are not visible in the reference samples (i) cellulose fiber functionalized with ATRP initiator (Figure 7.3b) and Munktell paper (Figure 7.3c), which indicates the successful grafting of PBEMA polymer to cellulose surface.

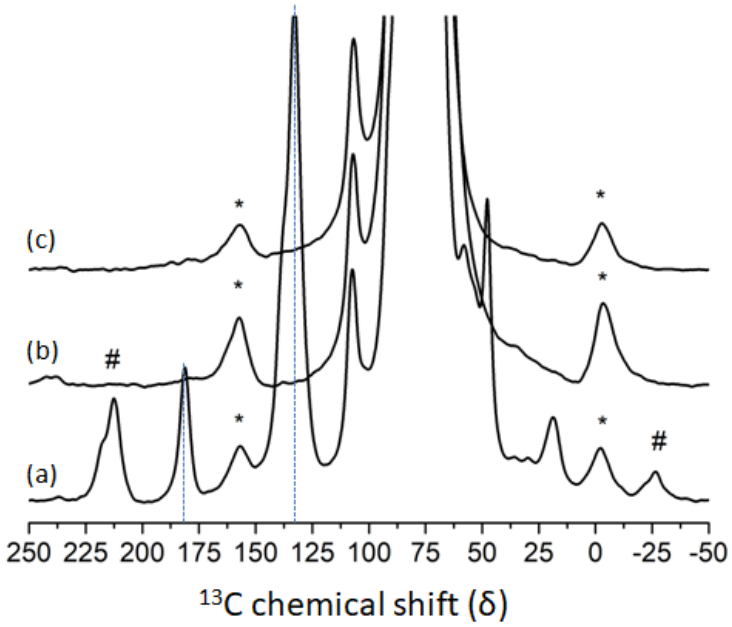

Figure 7.3 1H-^{13}C CPMAS spectra for the materials in different synthesis steps, measured at 8 kHz spinning rate, 110 K and with microwave on: (a) Paper substrate after grafting of the PBEMA polymer, (b) Paper substrate functionalized with ATRP initiator, (c) Non-functionalized Munktell paper. Note: These spectra were recorded after impregnation of the appropriate samples with 16 mM bTbK solution in TCE. The spinning sidebands in the spectra are shown by the symbols # and * above the signals. # are the side bands of the aromatic ring system at 132 ppm included in the PBEMA polymer while * represent the sidebands of the TCE ($C_2H_2Cl_4$). Adapted from ref [31].

7.3.3. Selective Enhancement of Functional Groups

By comparing the enhancement factors obtained for PBEMA functionalised paper in ^{1}H-^{13}C CPMAS DNP experiments impregnated with different radical solutions, important observations were made, which are summarized in the table given below (Table 7.2).

Table 7.2 Signal enhancement factors obtained from DNP enhanced ^{1}H -^{13}C CPMAS spectra depending on the employed solvent/radical matrix (hydrophobic/hydrophilic) for: (a) Paper functionalized with PBEMA polymer, (b) Paper functionalized with ATRP initiator, (c) Non-functionalised Munktell paper. Adapted from ref[31].

	Paper-PBEMA			Paper ATRP	Non-functionalized Munktell paper
	carbonyl (180 ppm)	**aromatic (132 ppm)**	**cellulose C1 (107ppm)**	**cellulose C1 (107ppm)**	**cellulose C1 (107ppm)**
10mM TEKPol/TCE (hydrophobic)	4 ±1	11 ± 1	1.40 ± 0.02	5.0 ± 0.2	3.0 ± 0.4
15mM TEKPol/TCE (hydrophobic)	31 ± 17	60 ± 16	1.70 ± 0.05	-	-
16mM bTbK/TCE (hydrophobic)	16 ±4	18 ± 2	1.30 ± 0.02	2.0 ± 0.1	3.7 ± 0.2
15mM AMUPol/D_2O/H_2O (hydrophilic)	4.2 ± 0.7	3.1 ± 0.2	21.4 ± 0.1	61 ± 1	49 ± 2

The maximum signal enhancement obtained for the signals at 132 and 180 ppm of the polymer is 60±16 and 31 ± 17, respectively, when impregnating the Paper-PBEMA sample with 15 mM TEKPol in TCE. However, the enhancement of the signal at 107 ppm of the C1 carbon is only 1.70±0.05. This observation allows us to assume that chemically different functional groups have different preferences towards the type of radical solutions, depending on their hydrophobic or hydrophilic nature. These results clearly indicate that a distinction between different functional groups is feasible via selective signal enhancement in DNP-NMR experiments, which may play an important role in separating signals when analysing functionalized materials.

Thus, a more detailed study was carried out in this direction, where the signal enhancements of different functional groups were studied as a function of the radical solution. An example is given in Figure 7.4. This figure shows the MW off and MW on spectra of PBEMA functionalized cellulose paper impregnated with two different radical solutions: (a) 15mM

TEKPol in TCE – hydrophobic, (b) 15mM AMUPol in D_2O/H_2O in 90:10 – hydrophilic. It can be seen that with the hydrophobic matrix (a), for the aromatic signal at 132 ppm, an enhancement factor of 60±16 is obtained, while the signal for carbonyl at 180 ppm is enhanced by 31 ± 17. In contrast, when the sample is treated with a hydrophilic matrix (AMUPol), the aromatic signal at 132 ppm is enhanced only by 3.1±0.2, while the carbonyl signal (180 ppm) is enhanced by 4.2±0.7. Such examples confirm that depending on the nature of matrices employed, different functional group on the paper surface can be enhanced selectively. For example, the enhancement of the dominating signals in the range of 55 and 110 ppm, associated to cellulose, has a strong dependency on the employed solvent/radical matrix. For this kind of functional groups, the hydrophobic matrix (TEKPol/TCE) yields an enhancement lower than 5, while significant enhancement of a factor 60 is obtained with the hydrophilic matrix (AMUPol in D_2O/H_2O).

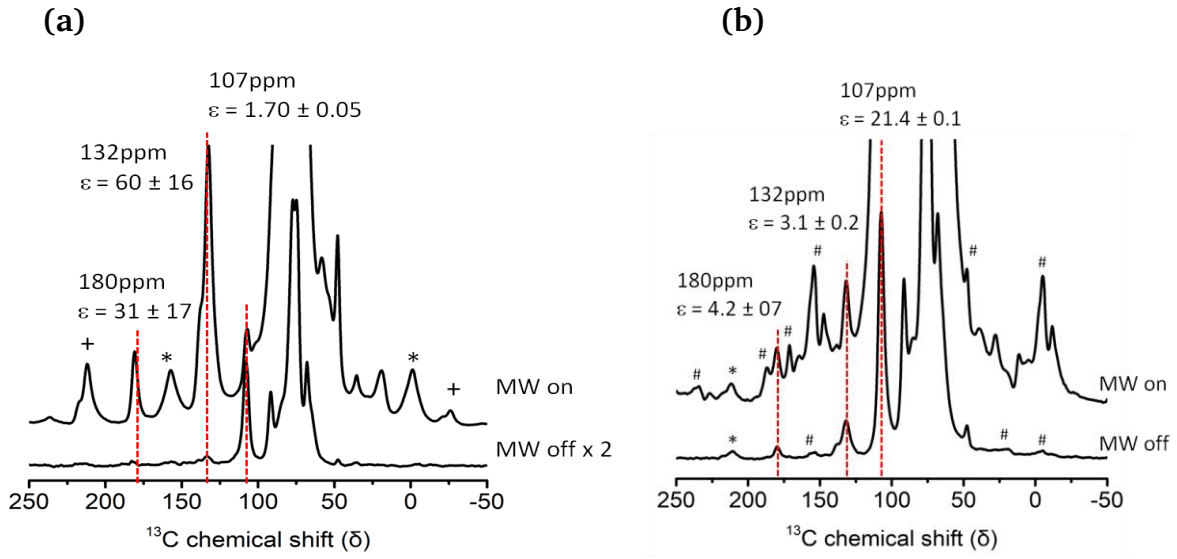

Figure 7.4 ^{1}H-^{13}C CPMAS spectra of the PBEMA functionalized paper substrate measured at a spinning rate of 8 kHz, nominally 110K with MW off and MW on to obtained the signal enhancement. (a) Impregnated with 15 mM TEKPol in TCE (hydrophobic matrix); (b) Impregnated with 15mM AMUPol in D_2O/H_2O 90:10 (hydrophilic matrix). Signals marked with #, * and + are spinning side bands corresponding to the backbone signal of paper material, TCE signal and aromatic groups of the polymer respectively. Adapted from ref [31].

7.4. Conclusions

From our experimental results in this chapter, it can be concluded that DNP-SENS is capable to investigate the successful surface functionalization of complex paper substrate. With this technique, it was possible to verify the binding of the ATRP linker and the grafting of PBEMA polymer. Along with this, the detailed study on utilizing different matrices (hydrophobic or hydrophilic) for functionalized cellulose paper substrate provided selective enhancements for

different functional groups present in the system. This allows an easy separation of the signals of the functional groups of interest from the dominating signal of the paper substrate.

8. Summary and Outlook

8.1. Summary and Conclusions

In this thesis solid-state NMR techniques partially combined with DNP were extensively used to study surface interactions and the surface functionalization of various porous materials. Three types of materials were discussed in the thesis: (i) mesoporous silica SBA-15, (ii) etched ion-track polycarbonate membranes and (iii) complex cellulose paper substrates. In the introduction, a thesis check-list is provided that outlined the aims of this thesis, which were fully or partially reached as summarized in the following.

For mesoporous silica, the detailed investigation of interactions of water and octanol-1 molecules with the pore surface of silica SBA-15 was presented. For this, conventional room temperature 1D and 2D solid-state NMR techniques were utilized. The 1D experiments provided valuable information on the ^{1}H chemical shift dependency of SBA-15 upon addition of water that allowed to confirm the model of pore filling. Local interactions between surface and guest molecules (octanol-1 and water) were studied by ^{1}H-^{29}Si FSLG CPMAS HETCOR experiment and via variation of the contact time, the orientation of octanol-1/water molecules inside the pore was determined. With these observations, the assembling of the octanol-1 and water molecules under the confinement was derived showing that hydroxyl groups from octanol-1 and water molecules have strong tendency to interact with silica surface. However, silica prefers water over the octanol-1 molecules and thus octanol stay little far away from surface with its hydrophilic head towards the surface while aliphatic chain in the intermediate range. Additional MD simulations validated these studies by providing the profile density curve of atoms/molecules present in the system. These studies further suggest the formation of an octanol bilayer in the pores of the SBA material.

While working on FSLG CPMAS HETCOR experiments, a challenging referencing problem on the indirect proton dimension was obtained. This lead the project in a new direction, namely to find a suitable referencing technique. In this context, a new referencing approach was developed using the 2D ^{1}H-^{1}H MAS FSLG pulse sequence. This type of experiment allows the exact referencing of the ^{1}H indirect dimension and has been successfully applied to reference the ^{1}H indirect dimension of ^{1}H-X FSLG CPMAS HETCOR experiments. This is undoubtedly an important finding of this thesis, which allows clear analysis of FSLG HETCOR spectra in future. Interestingly, it was also found that the new referencing approach provides high resolution spectra of the protons present in the system that opens up new pathways to study the complex interplay of protons in alcohol-water systems inside porous silica.

Moving forward in our check-list, we focused on materials comprising low surface areas, e.g., etched ion-track polycarbonate foils and cellulose paper substrate. Since these materials contain low surface areas, it was required to increase the sensitivity of solid-state NMR employing the DNP approach. The characterization of pore surface of silica coated ion etched PC membrane was investigated by DNP-SENS. DNP enhanced ^{1}H-^{29}Si CPMAS together with surface analysis by AFM images and calculation of specific pore surface areas confirmed the covalent binding of linker molecules inside the pore channel. Following this approach, functionalized paper substrates were investigated with DNP-SENS, since they also contain small surface area << 30 m^2/g. Various kinds of radical matrices were tested in these experiments to obtain a correlation between polarization matrix and reachable signal enhancement in the spectra. Interestingly, in the employed cross-polarization experiments selective signal amplification of different functional groups in the system was observed. This selective signal enhancement strongly depends on the compatibility of the sample and radical solution and can be controlled by its choice. The selective enhancement allows a directed suppression of signals of the cellulose/paper while enhancing the signals of the surface functionalization.

8.2. Future Perspectives

While this thesis has answered a number of open questions (see section 8.1.) there are still some aspects that have to be considered more in detail in the future. As described earlier, chapter four focused on studying octanol-1 or octanol-1/water mixtures in porous silica material. Octanol-1 is an eight carbon chain alcohol containing a hydrophilic OH-group and a linear hydrophobic aliphatic chain. This project will be further extended to conduct similar studies on isomers of octanol-1, mainly 2-propyl-1-pentanol and 2,4,4-trimethyl-1-pentanol (Figure 8.1), which were purposely chosen due to their molecular geometry/structure as they contain different branches. Such study will provide valuable information about the molecular alignment inside pores of silica SBA-15 in comparison to octanol-1, which is expected to strongly depend on the branch structure. These investigations are more challenging due to presence of additional branches, which make the system more complex near the silica surface and more difficult to determine which molecules (-OH or $–CH_3$) actively participate in interactions with silica surface. This may help to understand and optimize separation techniques for octanol related isomers employing porous media.

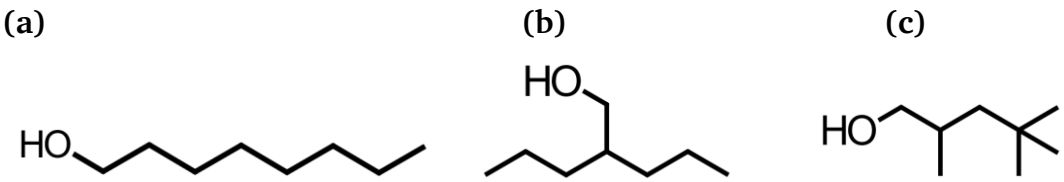

Figure 8.1 The chemical structures of octanol-1 and isomers of octanol: (b) 2-propyl-1-pentanol, (c) 2,4,4-trimethyl-1-pentanol.

Another, very interesting perspective is inspired from chapter five while working on the project to find a better referencing technique for the ^{1}H indirect dimension in FSLG CPMAS HETCOR spectra. In this study, it was found that ^{1}H-^{1}H MAS FSLG provides a highly resolved spectrum of the protons present in the system, which further delivers information to study exchange processes in the system via the cross peaks. The appearance and disappearance of cross peaks seemed strongly dependent on the z-filter delay employed and the temperature at which the experiments were carried out. Therefore, the plan is to perform studies on exchange processes over a wide range of temperature for the guest-host system consisting of alcohol-water in mesoporous silica.

Along with this, the thesis demonstrated the power of DNP-SENS experiments to proof the surface functionalization of materials such as papers or etched ion-track membranes having low surface area. Such approach may be utilized in future to study complex multicomponent biofunctionalized materials as used for sensing devices.

9. Appendix

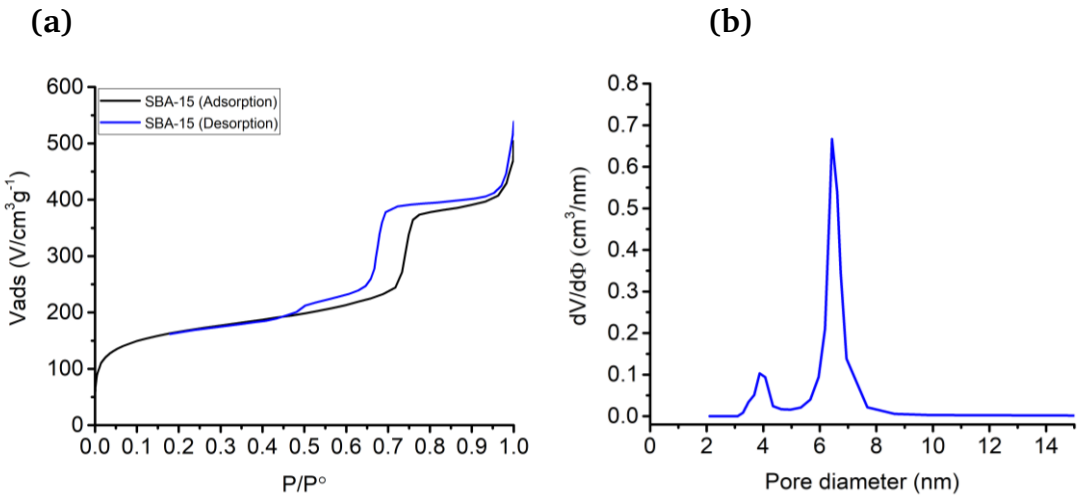

Figure 9.1 (a) Nitrogen adsorption-desorption isotherm plots of synthesized silica material (SBA-15), the isotherm shows the hysteresis at 0.7 P/P°. (b) The BJH plot to determine the pore diameter of synthesized silica material (SBA-15), it shows an artificial peak around 4nm due to the not fully completion of desorption and adsorption in the isotherm. Adapted from ref [24].

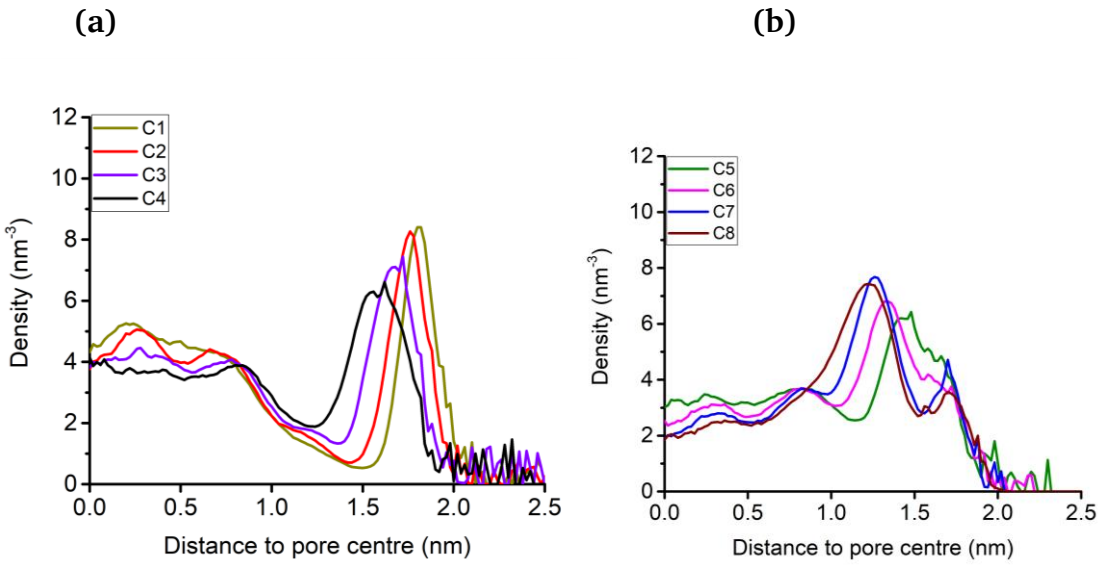

Figure 9.2 Number density profile of carbons of octanol-1 for 10 mol% at T=425K. (a) C1-C4 are more localized in the pore centre or the pore surface region, while (b) C5-C8 accumulates in the intermediate pore region.Reprinted (adapted) with permission from ref [24]. Copyright (2018) American Chemical Society.

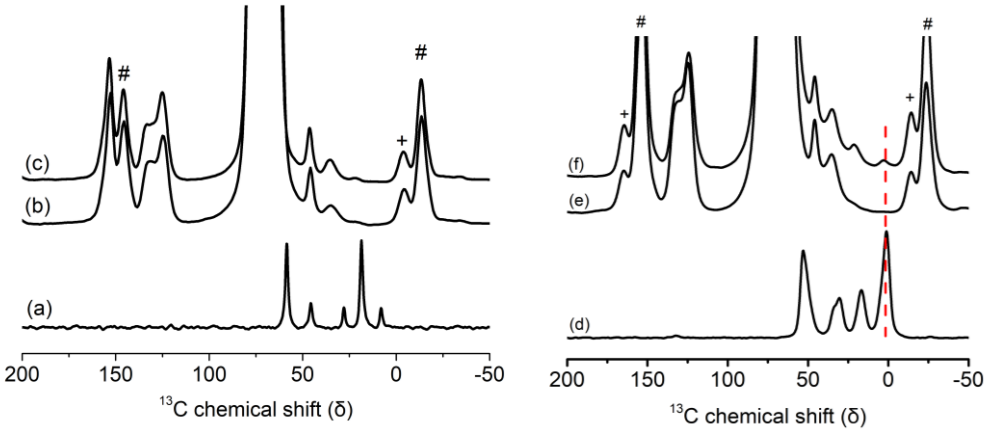

Figure 9.3 Comparison of the pure APTES (left) and APDMS (right) linker with functionalized linker on the cellulose surface to confirm the covalent binding of the linker to the surface molecule. (a) 13C NMR spectrum of the pure APTES linker, (b) ^{13}C CPMAS spectrum of the silica coated PC foil, (c) ^{13}C CPMAS spectrum of the silica coated polymer foil functionalized with APTES linker. (d) ^{13}C CPMAS spectrum of the pure APDMS linker, (e) ^{13}C CPMAS spectrum of the silica coated PC foil, (f) ^{13}C CPMAS spectrum of the silica coated membrane functionalized with APDMS. Note: The spectrum (a) was measured under static conditions at room temperature while spectra (b), (c) and (d) were measured at 8KHz spinning rate, nominally 110K and with MW on. The spectra (e) and (f) were measured at 9KHz spinning, nominally 110K with MW on. The signals marked with + or # are spinning sidebands of the signals corresponding to glycerol. Adapted from ref [31].

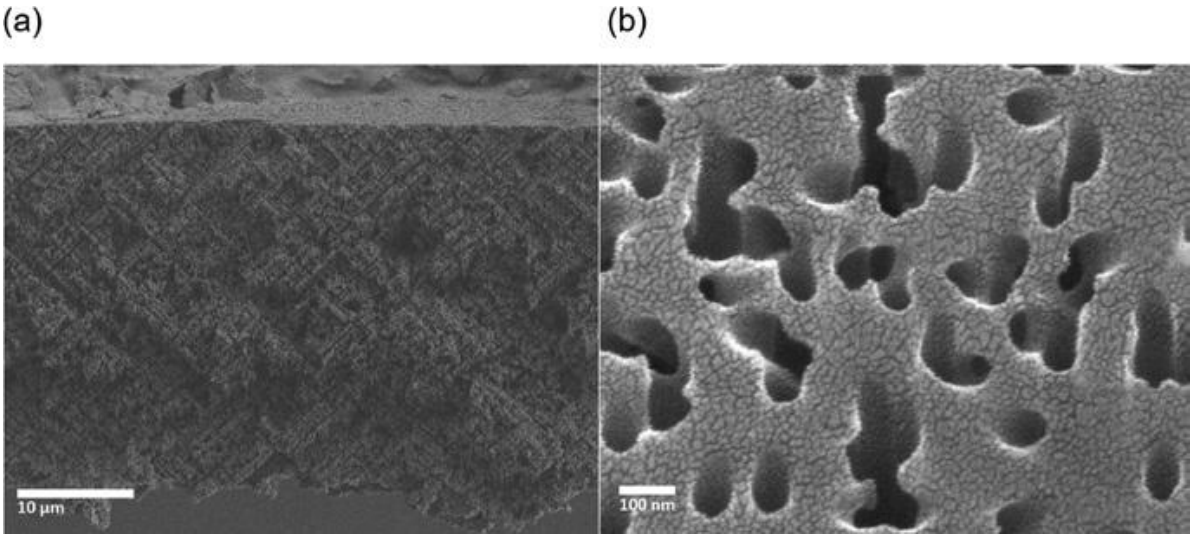

Figure 9.4 Scanning Electron Microscopy (SEM) images of (a) the cross section of the etched ion track PC foil coated with 20nm silica layer, the image reveals the high density of interconnected nano-channels. (b) The top-view of the planar surface of one of the membranes coated with 5nm silica layer. Reproduced with permission of de Gruyter in the format Thesis/Dissertation via Copyright Clearance Center from ref [30].

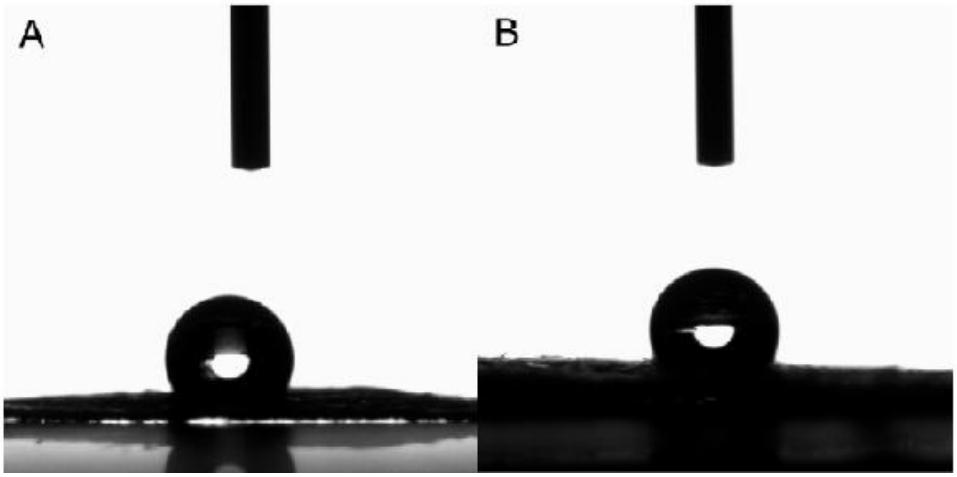

Figure 9.5 The contact angle measurement to determine the hydrophobicity and hydrophilicity of the: (a) ATRP-initiator functionalized paper substrate, (b) PBEMA grafted paper substrate. Reprinted (adapted) with permission from [31]. Copyright (2017) American Chemical Society.

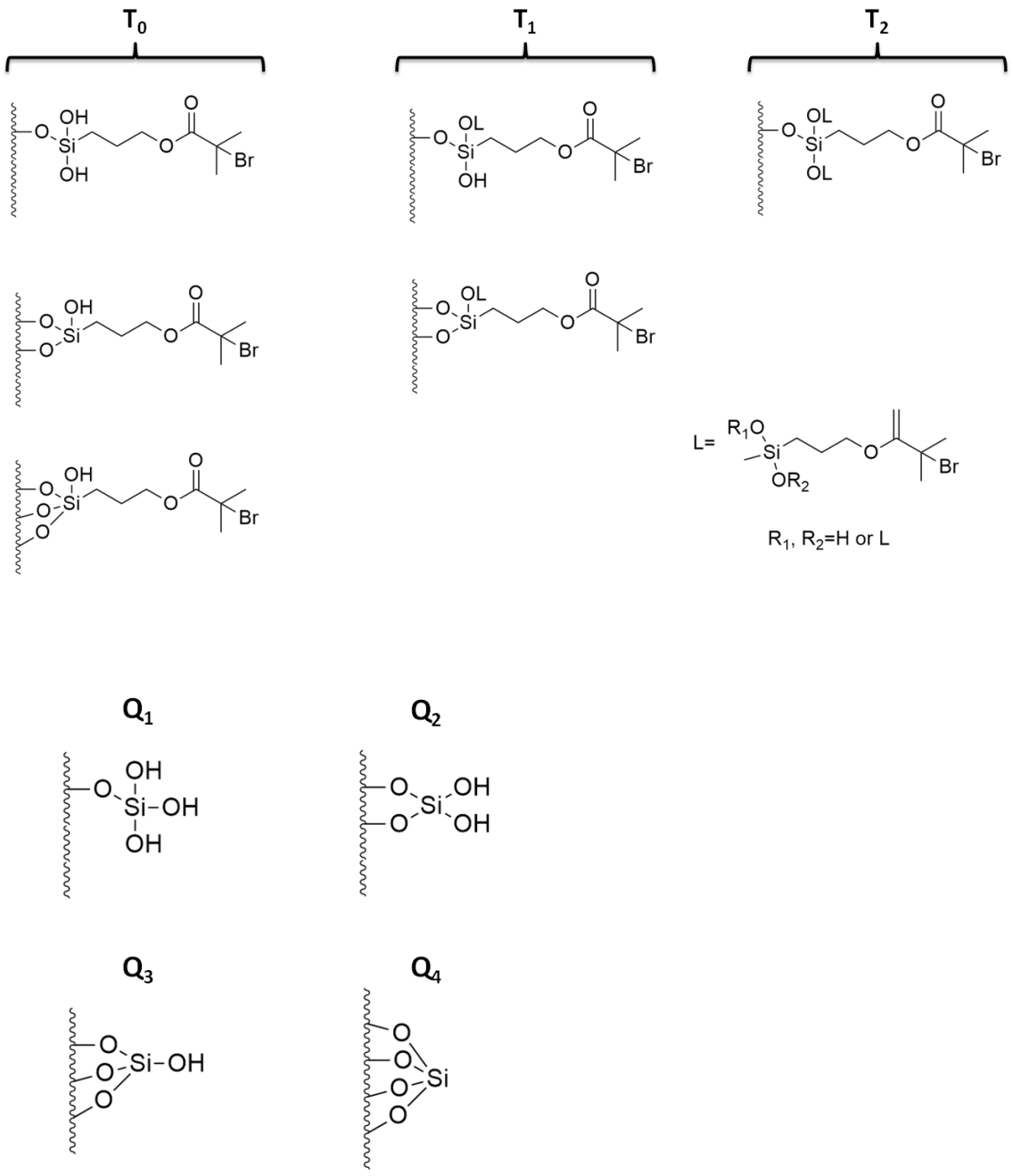

Figure 9.6 The T_n groups and their assignment to binding possibilities with the ATRP initiator on the cellulose surface along with chemical structure of Q_n groups. (Note: L in figure represents an attached linker molecule at the ATRP initiator molecule via Si-O-Si bond.) Adapted from ref[31].

9.1. Quantitative Surface Analysis of PC Foil

The ratio of the inner pore surface with the foil surface and approximation of the surface area:

To calculate the approximate ratio between inner pore surface on the comparison of membrane surface excluding the inner pore surface, a rough calculation was performed as follows. Assuming that the thickness of the PC foil was ($w=2^{1/2}*30\ \mu m$) as the PC foil was irradiated at an angle of 45°, number of channels ($N=4x2x10^{9}cm^{-2}$) and pore diameter ($d=95$ nm).

$A_{pore\ surface}/A_{foil\ surface} = N*\pi r*d*w = 4x2x10^{9}\ cm^{-2}*\pi*9500\ x10^{-9}cm*2^{1/2}*3000x10^{-6}cm$
$=1013.86 \sim 1010$

After ALD coating with a 5 nm SiO2 layer the inner channel diameter is reduced to ~85 nm, therefore:

$A_{pore\ surface}/A_{foil\ surface} = N*\pi r*d*w = 4x2x10^{9}\ cm^{-2}*\pi*8500\ x10^{-9}cm*2^{1/2}*3000x10^{-6}cm$
$=906.53\sim 910$

Furthermore, the specific surface area for the SiO2 coated membrane can be approximated as follows:

(1) The overall volume of a foil containing an area of 1 cm^2 and a thickness of 30 um is 0.003 cm^3.

(2) In this volume, the surface that is given by the inner-pore surface is approximately 906.53 cm^2.

(3) 1 cm^3 of the SiO_2 coated membrane thus contains a surface that is given by 906.53 cm^2 /0.003 cm^3 = ~ 302176.66 cm^2/cm^3 = 30.2 m^2/cm^3

(4) Assuming a density of the polycarbonate of 1.20 g/cm^3 the specific surface area A_{spec} is 30.2/ 1.20 = 25.16 $m^2/g \sim 25\ m^2/g$.

10. References

1. M. S. Morey, A. Davidson and G. D. Stucky, *J. Porous Mater.*, 1998, **5**, 195-204.

2. H.-T. Chen, S. Huh, J. W. Wiench, M. Pruski and V. S. Y. Lin, *J. Am. Chem. Soc.*, 2005, **127**, 13305-13311.

3. A. Vinu, K. Z. Hossain and K. Ariga, *Journal of Nanoscience and Nanotechnology*, 2005, **5**, 347-371.

4. X. G. Wang, K. S. K. Lin, J. C. C. Chan and S. F. Cheng, *J. Phys. Chem. B*, 2005, **109**, 1763-1769.

5. A. Vinu, M. Miyahara and K. Ariga, *Journal of Nanoscience and Nanotechnology*, 2006, **6**, 1510-1532.

6. S. Sim, O. M. Kwon, K. H. Ahn, H. R. Lee, Y. J. Kang and E. B. Cho, *J. Appl. Polym. Sci.*, 2018, **135**.

7. X. B. Huang, X. Chen, A. Li, D. Atinafu, H. Y. Gao, W. J. Dong and G. Wang, *Chem. Eng. J.*, 2019, **356**, 641-661.

8. M. E. Li, S. X. Wang, L. X. Han, W. J. Yuan, J. B. Cheng, A. N. Zhang, H. B. Zhao and Y. Z. Wang, *J. Hazard. Mater.*, 2019, **375**, 61-69.

9. J. Oh, Y. K. Kim, J. S. Lee and J. Jang, *Nanoscale*, 2019, **11**, 6462-6470.

10. S. P. Adiga, C. Jin, L. A. Curtiss, N. A. Monteiro-Riviere and R. J. Narayan, *Wiley Interdiscip Rev Nanomed Nanobiotechnol*, 2009, **1**, 568-581.

11. H. J. G. E. Gardeniers, *Analytical and Bioanalytical Chemistry*, 2009, **394**, 385-397.

12. M. Tagliazucchi and I. Szleifer, *Mater. Today*, 2015, **18**, 131-142.

13. H. Olsson, G. Nyström, M. Strømme, M. Sjödin and L. Nyholm, *Electrochem. Commun.*, 2011, **13**, 869-871.

14. L. Xie, G. Yang, M. Mäntysalo and F. Jonsson, *IEEE Eng. Med. Biol. Soc.*, 2012, 5026–5029.

15. D. Tobjork and R. Osterbacka, *Adv. Mater.*, 2011, **23**, 1935-1961.

16. K. Abe, K. Kotera, K. Suzuki and D. Citterio, *Analytical and Bioanalytical Chemistry*, 2010, **398**, 885-893.

17. V. Leung, A. A. M. Shehata, C. D. M. Filipe and R. Pelton, *Colloids and Surfaces a-Physicochemical and Engineering Aspects*, 2010, **364**, 16-18.

18. M. W. Anderson, T. Ohsuna, Y. Sakamoto, Z. Liu, A. Carlsson and O. Terasaki, *Chem. Commun.*, 2004, DOI: 10.1039/B313208K, 907-916.

19. D. Losic, R. J. Pillar, T. Dilger, J. Mitchell and N. Voelcker, *J. Porous Mater.*, 2007, **14**, 61-69.

20. S. N. Kokorin, E. A. Sosnov and A. A. Malygin, *Journal of Surface Investigation. X-ray, Synchrotron and Neutron Techniques*, 2008, **2**, 696-698.

21. G. Buntkowsky, *Phys. Chem. Chem. Phys.*, 2007, **9**, 4843.

22. A. G. M. Rankin, J. Trebosc, F. Pourpoint, J. P. Amoureux and O. Lafon, *Solid State Nucl. Magn. Reson.*, 2019, **101**, 116-143.

23. H. Koller and M. Weiß, in *Solid State NMR*, ed. J. C. C. Chan, Springer Berlin Heidelberg, Berlin, Heidelberg, 2012, DOI: 10.1007/128_2011_123, pp. 189-227.

24. B. Kumari, M. Brodrecht, H. Breitzke, M. Werner, B. Grünberg, H.-H. Limbach, S. Forg, E. P. Sanjon, B. Drossel, T. Gutmann and G. Buntkowsky, *The Journal of Physical Chemistry C*, 2018, **122**, 19540-19550.

25. A. Lesage, M. Lelli, D. Gajan, M. A. Caporini, V. Vitzthum, P. Miéville, J. Alauzun, A. Roussey, C. Thieuleux, A. Medhi, G. Bodenhausen, C. Copéret and L. Emsley, *J. Am. Chem. Soc.*, 2010, **132**, 15459.

26. M. Lelli, D. Gajan, A. Lesage, M. A. Caporini, V. Vitzthum, P. Miéville, F. Héroguel, F. Rascón, A. Roussey, C. Thieuleux, M. Boualleg, L. Veyre, G. Bodenhausen, C. Coperet and L. Emsley, *J. Am. Chem. Soc.*, 2011, **133**, 2104-2107.

27. A. J. Rossini, A. Zagdoun, M. Lelli, D. Gajan, F. Rascon, M. Rosay, W. E. Maas, C. Coperet, A. Lesage and L. Emsley, *Chemical Science*, 2012, **3**, 108-115.

28. A. Zagdoun, G. Casano, O. Ouari, G. Lapadula, A. J. Rossini, M. Lelli, M. Baffert, D. Gajan, L. Veyre, W. E. Maas, M. Rosay, R. T. Weber, C. Thieuleux, C. Coperet, A. Lesage, P. Tordo and L. Emsley, *J. Am. Chem. Soc.*, 2012, **134**, 2284-2291.

29. W. R. Gruning, A. J. Rossini, A. Zagdoun, D. Gajan, A. Lesage, L. Emsley and C. Coperet, *PCCP*, 2013, **15**, 13270-13274.

30. B. Kumari, D. John, P. Hoffmann, A. Spende, E. Toimil-Molares Maria, C. Trautmann, C. Hess, P. Ruff, M. Schulze, R. Stark, G. Buntkowsky, A. Andrieu-Brunsen and T. Gutmann, *Journal*, **2018**, 232, 1173.

31. T. Gutmann, B. Kumari, L. Zhao, H. Breitzke, S. Schöttner, C. Rüttiger and M. Gallei, *The Journal of Physical Chemistry C*, 2017, **121**, 3896-3903.

32. V. Chaudhary and S. Sharma, *J. Porous Mater.*, 2017, **24**, 741-749.

33. G. F. Torres, S. Commeaux and P. O. Troncoso, *Journal of Functional Biomaterials*, 2012, **3**.

34. M. H. Levitt, *Spin Dynamics: Basics of Nuclear Magnetic Resonance*, Wiley, 2008.

35. J. Keeler, *Understanding NMR Spectroscopy*, Wiley, 2010.

36. J. M. B. Kellogg, I. I. Rabi, N. F. Ramsey and J. R. Zacharias, *Physical Review*, 1939, **56**, 728-743.

37. I. I. Rabi, S. Millman, P. Kusch and J. R. Zacharias, *Physical Review*, 1939, **55**, 526-535.

38. E. M. Purcell, H. C. Torrey and R. V. Pound, *Physical Review*, 1946, **69**, 37-38.

39. F. Bloch, W. W. Hansen and M. Packard, *Physical Review*, 1946, **69**, 127-127.

40. *Fundamentals of Molecular & Spectroscopy*, McGraw-Hill Education (India) Pvt Limited, 2001.

41. E. R. Andrew, A. Bradbury and R. G. Eades, *Nature*, 1958, **182**, 1659-1659.

42. E. R. Andrew, A. Bradbury and R. G. Eades, *Nature*, 1959, **183**, 1802-1803.

43. E. R. Andrew, *Prog. Nucl. Magn. Reson. Spectrosc.*, 1971, **8**, 1-39.

44. E. R. Andrew and E. Szczesniak, *Prog. Nucl. Magn. Reson. Spectrosc.*, 1995, **28**, 11-36.

45. A. Bielecki, A. C. Kolbert and M. H. Levitt, *Chem. Phys. Lett.*, 1989, **155**, 341-346.

46. I. Scholz, P. Hodgkinson, B. H. Meier and M. Ernst, *The Journal of Chemical Physics*, 2009, **130**, 114510.

47. A. E. Bennett, C. M. Rienstra, M. Auger, K. V. Lakshmi and R. G. Griffin, *The Journal of Chemical Physics*, 1995, **103**, 6951-6958.

48. S. R. Hartmann and E. L. Hahn, *Physical Review*, 1962, **128**, 2042-2053.

49. E. O. Stejskal, J. Schaefer and J. S. Waugh, *Journal of Magnetic Resonance (1969)*, 1977, **28**, 105-112.

50. G. Metz, X. L. Wu and S. O. Smith, *Journal of Magnetic Resonance, Series A*, 1994, **110**, 219-227.

51. M. J. Duer, *Introduction to Solid-State NMR Spectroscopy*, Wiley, 2005.

52. M. Brodrecht, B. Kumari, H. Breitzke, T. Gutmann and G. Buntkowsky, *Journal*, **2018**, 232, 1127.

53. M. F. Harrach, B. Drossel, W. Winschel, T. Gutmann and G. Buntkowsky, *The Journal of Physical Chemistry C*, 2015, **119**, 28961-28969.

54. M. Lee and W. I. Goldburg, *Physical Review*, 1965, **140**, A1261-A1271.

55. B. J. van Rossum, H. Förster and H. J. M. de Groot, *J. Magn. Reson.*, 1997, **124**, 516.

56. T. Maly, G. T. Debelouchina, V. S. Bajaj, K.-N. Hu, C.-G. Joo, M. L. Mak–Jurkauskas, J. R. Sirigiri, P. C. A. v. d. Wel, J. Herzfeld, R. J. Temkin and R. G. Griffin, *The Journal of Chemical Physics*, 2008, **128**, 052211.

57. R. G. Griffin and T. F. Prisner, *PCCP*, 2010, **12**, 5737-5740.

58. V. S. Bajaj, C. T. Farrar, M. K. Hornstein, I. Mastovsky, J. Vieregg, J. Bryant, B. Eléna, K. E. Kreischer, R. J. Temkin and R. G. Griffin, *J Magn Reson*, 2003, **160**, 85-90.

59. A. A. Lysova and I. V. Koptyug, *Chem. Soc. Rev.*, 2010, **39**, 4585-4601.

60. S. B. Duckett and R. E. Mewis, *Acc. Chem. Res.*, 2012, **45**, 1247-1257.

61. K. V. Kovtunov, V. V. Zhivonitko, I. V. Skovpin, D. A. Barskiy and I. V. Koptyug, in *Hyperpolarization Methods in NMR Spectroscopy*, Springer, 2012, pp. 123-180.

62. S. S. Arzumanov and A. G. Stepanov, *The Journal of Physical Chemistry C*, 2013, **117**, 2888-2892.

63. H. Henning, M. Dyballa, M. Scheibe, E. Klemm and M. Hunger, *Chem. Phys. Lett.*, 2013, **555**, 258-262.

64. K. V. Kovtunov, E. V. Pokochueva, O. G. Salnikov, S. F. Cousin, D. Kurzbach, B. Vuichoud, S. Jannin, E. Y. Chekmenev, B. M. Goodson, D. A. Barskiy and I. V. Koptyug, *Chem.-Asian J.*, 2018, **13**, 1857-1871.

65. J. H. Ardenkjaer-Larsen, *Journal of Magnetic Resonance*, 2016, **264**, 3-12.

66. R. G. Lawler, *Acc. Chem. Res.*, 1972, **5**, 25-33.

67. W. Happer, E. Miron, S. Schaefer, D. Schreiber, W. A. van Wijngaarden and X. Zeng, *Physical Review A*, 1984, **29**, 3092-3110.

68. J.-L. Bonardet, J. Fraissard, A. Gédéon and M.-A. Springuel-Huet, *Catalysis Reviews*, 1999, **41**, 115-225.

69. E. Brunner, *Concepts in Magnetic Resonance*, 1999, **11**, 313-335.

70. T. G. Walker, *Journal of Physics: Conference Series*, 2011, **294**, 012001.

71. X. Zi, R. Wang, L. Liu, H. Dai, G. Zhang and H. He, *Chinese Journal of Catalysis*, 2011, **32**, 827-835.

72. A. S. Lilly Thankamony, J. J. Wittmann, M. Kaushik and B. Corzilius, *Prog. Nucl. Magn. Reson. Spectrosc.*, 2017, **102-103**, 120-195.

73. U. Akbey, W. T. Franks, A. Linden, M. Orwick-Rydmark, S. Lange and H. Oschkinat, in *Hyperpolarization Methods in Nmr Spectroscopy*, ed. L. T. Kuhn, Springer-Verlag Berlin, Berlin, 2013, vol. 338, pp. 181-228.

74. A. W. Overhauser, *Physical Review*, 1953, **92**, 411-415.

75. T. R. Carver and C. P. Slichter, *Physical Review*, 1953, **92**, 212-213.

76. A. Abragam, *Une nouvelle méthode de polarisation dynamique des noyaux atomiques dans les solides*, Centre d'études nucléaires de Saclay, Gif-sur-Yvette (S.-et-O.), 1958.

77. C. D. Jeffries, *Physical Review*, 1957, **106**, 164-165.

78. A. V. Kessenikh and A. A. Manenkov, *SOVIET PHYSICS-SOLID STATE*, 1963, **5**, 835-837.

79. C. F. Hwang and D. A. Hill, *Phys. Rev. Lett.*, 1967, **19**, 1011-1014.

80. C. F. Hwang and D. A. Hill, *Phys. Rev. Lett.*, 1967, **18**, 110-112.

81. L. R. Becerra, G. J. Gerfen, B. F. Bellew, J. A. Bryant, D. A. Hall, S. J. Inati, R. T. Weber, S. Un, T. F. Prisner, A. E. McDermott, K. W. Fishbein, K. E. Kreischer, R. J. Temkin, D. J. Singel and R. G. Griffin, *Journal of Magnetic Resonance, Series A*, 1995, **117**, 28-40.

82. L. R. Becerra, G. J. Gerfen, R. J. Temkin, D. J. Singel and R. G. Griffin, *Phys. Rev. Lett.*, 1993, **71**, 3561.

83. G. J. Gerfen, L. R. Becerra, D. A. Hall, R. G. Griffin, R. J. Temkin and D. J. Singel, *The Journal of Chemical Physics*, 1995, **102**, 9494-9497.

84. R. G. Griffin, *Nature*, 2010, **468**, 381.

85. Q. Z. Ni, E. Daviso, T. V. Can, E. Markhasin, S. K. Jawla, T. M. Swager, R. J. Temkin, J. Herzfeld and R. G. Griffin, *Acc. Chem. Res.*, 2013, **46**, 1933-1941.

86. U. Akbey, B. Altin, A. Linden, S. Ozcelik, M. Gradzielski and H. Oschkinat, *PCCP*, 2013, **15**, 20706-20716.

87. T. Gutmann and G. Buntkowsky, in *Modern Magnetic Resonance*, ed. G. A. Webb, Springer International Publishing, Cham, 2017, DOI: 10.1007/978-3-319-28275-6_39-1, pp. 1-21.

88. C. Sauvée, M. Rosay, G. Casano, F. Aussenac, R. T. Weber, O. Ouari and P. Tordo, *Angew. Chem. Int. Ed.*, 2013, **52**, 10858-10861.

89. F. A. Perras, J. Viger-Gravel, K. M. N. Burgess and D. L. Bryce, *Solid State Nucl. Magn. Reson.*, 2013, **51-52**, 1-15.

90. K. R. Thurber and R. Tycko, *Isr. J. Chem.*, 2014, **54**, 39-46.

91. A. Lesage, M. Lelli, D. Gajan, M. A. Caporini, V. Vitzthum, P. Mieville, J. Alauzun, A. Roussey, C. Thieuleux, A. Mehdi, G. Bodenhausen, C. Copéret and L. Emsley, *J. Am. Chem. Soc.*, 2010, **132**, 15459.

92. A. J. Rossini, A. Zagdoun, M. Lelli, A. Lesage, C. Copéret and L. Emsley, *Acc. Chem. Res.*, 2013, **46**, 1942-1951.

93. M. Rosay, L. Tometich, S. Pawsey, R. Bader, R. Schauwecker, M. Blank, P. M. Borchard, S. R. Cauffman, K. L. Felch, R. T. Weber, R. J. Temkin, R. G. Griffin and W. E. Maas, *Phys. Chem. Chem. Phys.*, 2010, **12**, 5850.

94. M. Rosay, M. Blank and F. Engelke, *Journal of Magnetic Resonance*, 2016, **264**, 88-98.

95. A. Zagdoun, G. Casano, O. Ouari, M. Schwarzwälder, A. J. Rossini, F. Aussenac, M. Yulikov, G. Jeschke, C. Copéret, A. Lesage, P. Tordo and L. Emsley, *J. Am. Chem. Soc.*, 2013, **135**, 12790-12797.

96. C. S. Song, K. N. Hu, C. G. Joo, T. M. Swager and R. G. Griffin, *J. Am. Chem. Soc.*, 2006, **128**, 11385.

97. P. C. A. van der Wel, K.-N. Hu, J. Lewandowski and R. G. Griffin, *J. Am. Chem. Soc.*, 2006, **128**, 10840-10846.

98. A. J. Rossini, A. Zagdoun, F. Hegner, M. Schwarzwalder, D. Gajan, C. Coperet, A. Lesage and L. Emsley, *J. Am. Chem. Soc.*, 2012, **134**, 16899-16908.

99. O. Lafon, A. S. L. Thankamony, T. Kobayashi, D. Carnevale, V. Vitzthum, Slowing, II, K. Kandel, H. Vezin, J. P. Amoureux, G. Bodenhausen and M. Pruski, *Journal of Physical Chemistry C*, 2013, **117**, 1375-1382.

100. T. V. Can, M. A. Caporini, F. Mentink-Vigier, B. Corzilius, J. J. Walish, M. Rosay, W. E. Maas, M. Baldus, S. Vega, T. M. Swager and R. G. Griffin, *The Journal of Chemical Physics*, 2014, **141**, 064202.

101. O. Haze, B. Corzilius, A. A. Smith, R. G. Griffin and T. M. Swager, *J. Am. Chem. Soc.*, 2012, **134**, 14287-14290.

102. T. V. Can, Q. Z. Ni and R. G. Griffin, *Journal of Magnetic Resonance*, 2015, **253**, 23-35.

103. M. Abraham, R. W. Kedzie and C. D. Jeffries, *Physical Review*, 1957, **106**, 165-166.

104. K.-N. Hu, H.-h. Yu, T. M. Swager and R. G. Griffin, *J. Am. Chem. Soc.*, 2004, **126**, 10844-10845.

105. K. N. Hu, H. H. Yu, T. M. Swager and R. G. Griffin, *J. Am. Chem. Soc.*, 2004, **126**, 10844.

106. Y. Matsuki, T. Maly, O. Ouari, H. Karoui, F. Le Moigne, E. Rizzato, S. Lyubenova, J. Herzfeld, T. Prisner, P. Tordo and R. G. Griffin, *Angew. Chem. Int. Ed.*, 2009, **48**, 4996-5000.

107. Y. Hovav, A. Feintuch and S. Vega, *Journal of Magnetic Resonance*, 2010, **207**, 176-189.

108. K.-N. Hu, G. T. Debelouchina, A. A. Smith and R. G. Griffin, *The Journal of Chemical Physics*, 2011, **134**, 125105.

109. Y. Hovav, A. Feintuch and S. Vega, *Journal of Magnetic Resonance*, 2012, **214**, 29-41.

110. Y. Matsuki, T. Maly, O. Ouari, H. Karoui, F. Le Moigne, E. Rizzato, S. Lyubenova, J. Herzfeld, T. Prisner, P. Tordo and R. G. Griffin, *Angew. Chem., Int. Ed.*, 2009, **48**, 4996.

111. Y. Hovav, A. Feintuch and S. Vega, *J. Chem. Phys.*, 2011, **134**, 074509.

112. K. N. Hu, *Solid State Nucl. Magn. Reson.*, 2011, **40**, 31-41.

113. D. Shimon, A. Feintuch, D. Goldfarb and S. Vega, *PCCP*, 2014, **16**, 6687-6699.

114. A. Abragam and M. Goldman, *Rep. Prog. Phys.*, 1978, **41**, 395-467.

115. M. M. Hoffmann, S. Bothe, T. Gutmann, F.-F. Hartmann, M. Reggelin and G. Buntkowsky, *The Journal of Physical Chemistry C*, 2017, **121**, 2418-2427.

116. D. Daube, V. Aladin, J. Heiliger, J. J. Wittmann, D. Barthelmes, C. Bengs, H. Schwalbe and B. Corzilius, *J. Am. Chem. Soc.*, 2016, **138**, 16572-16575.

117. S. Bothe, M. M. Hoffmann, T. Gutmann and G. Buntkowsky, *The Journal of Physical Chemistry C*, 2017, **121**, 27089-27097.

118. M. M. Hoffmann, S. Bothe, T. Gutmann and G. Buntkowsky, *The Journal of Physical Chemistry C*, 2017, **121**, 22948-22957.

119. J. S. Higgins, A. H. Hodgson and R. V. Law, *J. Mol. Struct.*, 2002, **602-603**, 505-510.

120. P. M. Macdonald and R. Soong, *Journal of Magnetic Resonance*, 2007, **188**, 1-9.

121. B. Grünberg, T. Emmler, E. Gedat, I. Shenderovich, G. H. Findenegg, H.-H. Limbach and G. Buntkowsky, *Chemistry – A European Journal*, 2004, **10**, 5689-5696.

122. K. Hu, Y. Zhou, J. Shen, Z. Ji and G. Cheng, *The Journal of Physical Chemistry B*, 2007, **111**, 10160-10165.

123. L. D. Gelb and K. E. Gubbins, *Phys. A*, 1997, **244**, 112.

124. W. T. Gozdz, K. E. Gubbins and A. Z. Panagiotopoulos, *Mol. Phys.*, 1995, **84**, 825.

125. M. Sliwinska-Bartkowiak, R. Sikorski, S. L. Sowers, L. D. Gelb and K. E. Gubbins, *Fluid Phase Equilib.*, 1997, **136**, 93.

126. M. Sliwinska-Bartkowiak, S. L. Sowers and K. E. Gubbins, *Langmuir*, 1997, **13**, 1182.

127. G. E. Brown, *Science*, 2001, **294**, 67.

128. A. Leo, C. Hansch and D. Elkins, *Chem. Rev.*, 1971, **71**, 525-616.

129. P. Ball, *Chem. Rev.*, 2008, **108**, 74.

130. K. L. Prime and G. M. Whitesides, *Science*, 1991, **252**, 1164.

131. S. A. Best, K. M. Merz and C. H. Reynolds, *The Journal of Physical Chemistry B*, 1999, **103**, 714-726.

132. J. M. Bolts and M. S. Wrighton, *The Journal of Physical Chemistry*, 1976, **80**, 2641-2645.

133. B. Chen and J. I. Siepmann, *J. Am. Chem. Soc.*, 2000, **122**, 6464-6467.

134. N. M. Garrido, A. J. Queimada, M. Jorge, E. A. Macedo and I. G. Economou, *Journal of Chemical Theory and Computation*, 2009, **5**, 2436-2446.

135. A. P. Lyubartsev, S. P. Jacobsson, G. Sundholm and A. Laaksonen, *The Journal of Physical Chemistry B*, 2001, **105**, 7775-7782.

136. B. Chen and J. I. Siepmann, *The Journal of Physical Chemistry B*, 2006, **110**, 3555-3563.

137. J. L. MacCallum and D. P. Tieleman, *J. Am. Chem. Soc.*, 2002, **124**, 15085-15093.

138. P. Sassi, M. Paolantoni, R. S. Cataliotti, F. Palombo and A. Morresi, *The Journal of Physical Chemistry B*, 2004, **108**, 19557-19565.

139. C. Hansch, J. P. Björkroth and A. Leo, *J. Pharm. Sci.*, 1987, **76**, 663-687.

140. M. N. Martinez and G. L. Amidon, *The Journal of Clinical Pharmacology*, 2002, **42**, 620-643.

141. R. N. Smith, C. Hansch and M. M. Ames, *J. Pharm. Sci.*, 1975, **64**, 599-606.

142. M. Vogel, *Eur. Phys. J.: Spec. Top.*, 2010, **189**, 47.

143. G. Buntkowsky, H. Breitzke, A. Adamczyk, F. Roelofs, T. Emmler, E. Gedat, B. Grünberg, Y. Xu, H.-H. Limbach, I. Shenderovich, A. Vyalikh and G. Findenegg, *PCCP*, 2007, **9**, 4843-4853.

144. M. Werner, N. Rothermel, H. Breitzke, T. Gutmann and G. Buntkowsky, *Isr. J. Chem.*, 2014, **54**, 60-73.

145. G. Buntkowsky, H. Breitzke, A. Adamczyk, F. Roelofs, T. Emmler, E. Gedat, B. Grunberg, Y. P. Xu, H. H. Limbach, I. Shenderovich, A. Vyalikh and G. Findenegg, *PCCP*, 2007, **9**, 4843-4853.

146. B. J. van Rossum, C. P. de Groot, V. Ladizhansky, S. Vega and H. J. M. de Groot, *J. Am. Chem. Soc.*, 2000, **122**, 3465.

147. J. Trebosc, J. W. Wiench, S. Huh, V. S. Y. Lin and M. Pruski, *J. Am. Chem. Soc.*, 2005, **127**, 7587.

148. G. Paul, S. Steuernagel and H. Koller, *Chem. Commun.*, 2007, 5194.

149. J. W. Wiench, Y. S. Avadhut, N. Maity, S. Bhaduri, G. K. Lahiri, M. Pruski and S. Ganapathy, *J. Phys. Chem. B*, 2007, **111**, 3877.

150. I. Ben Shir, S. Kababya and A. Schmidt, *J. Phys. Chem. C*, 2012, **116**, 9691.

151. T. Kobayashi, K. Mao, S. G. Wang, V. S. Y. Lin and M. Pruski, *Solid State Nucl. Magn. Reson.*, 2011, **39**, 65.

152. J. L. Rapp, Y. L. Huang, M. Natella, Y. Cai, V. S. Y. Lin and M. Pruski, *Solid State Nucl. Magn. Reson.*, 2009, **35**, 82.

153. M. Nayeri, M. T. Aronson, D. Bernin, B. F. Chmelka and A. Martinelli, *Soft Matter*, 2014, **10**, 5618.

154. T. Ukmar, T. Cendak, M. Mazaj, V. Kaucic and G. Mali, *J. Phys. Chem. C*, 2012, **116**, 2662.

155. M. Werner, N. Rothermel, H. Breitzke, T. Gutmann and G. Buntkowsky, *Isr. J. Chem.*, 2014, **54**, 60.

156. R. Schmitz, N. Müller, S. Ullmann and M. Vogel, *The Journal of Chemical Physics*, 2016, **145**, 104703.

157. X.-Y. Guo, T. Watermann and D. Sebastiani, *The Journal of Physical Chemistry B*, 2014, **118**, 10207-10213.

158. S. M. Melnikov, A. Höltzel, A. Seidel-Morgenstern and U. Tallarek, *Anal. Chem.*, 2011, **83**, 2569-2575.

159. J. Rodriguez, M. D. Elola and D. Laria, *The Journal of Physical Chemistry B*, 2009, **113**, 12744-12749.

160. A. Phan, D. R. Cole and A. Striolo, *Langmuir*, 2014, **30**, 8066-8077.

161. A. Vyalikh, T. Emmler, E. Gedat, I. Shenderovich, G. H. Findenegg, H. H. Limbach and G. Buntkowsky, *Solid State Nucl. Magn. Reson.*, 2005, **28**, 117.

162. A. Vyalikh, T. Emmler, I. Shenderovich, Y. Zeng, G. H. Findenegg and G. Buntkowsky, *Phys. Chem. Chem. Phys.*, 2007, **9**, 2249.

163. K. Elamin, H. Jansson, S. Kittaka and J. Swenson, *PCCP*, 2013, **15**, 18437-18444.

164. K. Elamin, H. Jansson and J. Swenson, *PCCP*, 2015, **17**, 12978-12987.

165. G. Schirò, A. Cupane, S. E. Pagnotta and F. Bruni, *J. Non-Cryst. Solids*, 2007, **353**, 4546-4551.

166. J. Swenson, K. Elamin, G. Chen, W. Lohstroh and V. G. Sakai, *The Journal of Chemical Physics*, 2014, **141**, 214501.

167. J. Swenson, K. Elamin, H. Jansson and S. Kittaka, *Chem. Phys.*, 2013, **424**, 20-25.

168. A. Vyalikh, T. Emmler, B. Grunberg, Y. Xu, I. Shenderovich, G. H. Findenegg, H. H. Limbach and G. Buntkowsky, *Z. Phys. Chem.*, 2007, **221**, 155.

169. J. Zang, S. Konduri, S. Nair and D. S. Sholl, *ACS Nano*, 2009, **3**, 1548-1556.

170. M. Fioroni, M. D. Diaz, K. Burger and S. Berger, *J. Am. Chem. Soc.*, 2002, **124**, 7737-7744.

171. T. Yamaguchi, S. Imura, T. Kai and K. Yoshida, *Zeitschrift Fur Naturforschung Section a-a Journal of Physical Sciences*, 2013, **68**, 145-151.

172. D. A. Bonhommeau, A. Perret, J. M. Nuzillard, C. Cilindre, T. Cours, A. Alijah and G. Liger-Belair, *Journal of Physical Chemistry Letters*, 2014, **5**, 4232-4237.

173. D. Zhao, J. Feng, Q. Huo, N. Melosh, G. H. Fredrickson, B. F. Chmelka and G. D. Stucky, *Science*, 1998, **279**, 548-552.

174. WilfriedC, Temperature - dependent LLE in the non - miscible binary system octanol / water, https://de.wikipedia.org/wiki/Octanol-Wasser-Verteilungskoeffizient).

175. K. Albert and E. Bayer, *J. Chromatogr.*, 1991, **544**, 345-370.

176. S. Björklund and V. Kocherbitov, *Scientific Reports*, 2017, **7**, 9960.

177. in *eMagRes*, DOI: 10.1002/9780470034590.emrstm1003.

178. J. Senker, L. Seyfarth and J. Voll, *Solid State Sciences*, 2004, **6**, 1039-1052.

179. J. Sehnert and J. Senker, *Chemistry – A European Journal*, 2007, **13**, 6339-6350.

180. C. Martineau and F. Taulelle, *EPJ Web of Conferences*, 2012, **30**.

181. S. Macholl, D. Tietze and G. Buntkowsky, *CrystEngComm*, 2013, **15**, 8627-8638.

182. J. A. Ripmeester and R. E. Wasylishen, *CrystEngComm*, 2013, **15**, 8598-8598.

183. B. Kumari, M. Brodrecht, T. Gutmann, H. Breitzke and G. Buntkowsky, *Appl. Magn. Reson.*, 2019, DOI: 10.1007/s00723-019-01156-2.

184. L. Sattlegger, T. Haider, C. Volker, H. Kerber, J. Kramm, L. Zimmermann and F. R. Wurm, *Chem. unserer Zeit*, DOI: 10.1002/ciuz.201900875.

185. F. Welle, *Resources Conservation and Recycling*, 2011, **55**, 865-875.

186. C. Bach, X. Dauchy, M. C. Chagnon and S. Etienne, *Water Res.*, 2012, **46**, 571-583.

187. Q. Y. Wang, D. C. Yang, Y. Qiu, X. T. Zhang, W. B. Song and L. Z. Hu, *Appl. Phys. Lett.*, 2018, **112**.

188. R. L. Fleischer, P. B. Price, R. M. Walker and R. M. Walker, *Nuclear Tracks in Solids: Principles and Applications*, University of California Press, 1975.

189. J. Duan, J. Liu, Y. Zhang, C. Trautmann and D. Y. Lei, *Journal of Materials Chemistry C*, 2016, **4**, 3956-3962.

190. I. Schubert, L. Burr, C. Trautmann and M. E. Toimil-Molares, *Beilstein Journal of Nanotechnology*, 2015, **6**, 1272-1280.

191. Z. Ezzeddine, I. Batonneau-Gener, Y. Pouilloux, H. Hamad, Z. Saad and V. Kazpard, *Microporous Mesoporous Mater.*, 2015, **212**, 125-136.

192. Q. Wen, D. Yan, F. Liu, M. Wang, Y. Ling, P. Wang, P. Kluth, D. Schauries, C. Trautmann, P. Apel, W. Guo, G. Xiao, J. Liu, J. Xue and Y. Wang, *Adv. Funct. Mater.*, 2016, **26**, 5796-5803.

193. M. Tagliazucchi and I. Szleifer, *Chemically Modified Nanopores and Nanochannels*, Elsevier Science, 2016.

194. A. Spende, N. Sobel, M. Lukas, R. Zierold, J. C. Riedl, L. Gura, I. Schubert, J. M. M. Moreno, K. Nielsch, B. Stühn, C. Hess, C. Trautmann and M. E. Toimil-Molares, *Nanotechnology*, 2015, **26**, 335301.

195. N. Sobel, C. Hess, M. Lukas, A. Spende, B. Stühn, M. E. Toimil-Molares and C. Trautmann, *Beilstein Journal of Nanotechnology*, 2015, **6**, 472-479.

196. J. Blümel, *Coord. Chem. Rev.*, 2008, **252**, 2410-2423.

197. J. L. Rapp, Y. Huang, M. Natella, Y. Cai, V. S. Y. Lin and M. Pruski, *Solid State Nucl. Magn. Reson.*, 2009, **35**, 82-86.

198. J. W. Wiench, Y. S. Avadhut, N. Maity, S. Bhaduri, G. K. Lahiri, M. Pruski and S. Ganapathy, *The Journal of Physical Chemistry B*, 2007, **111**, 3877-3885.

199. T. Gutmann, A. Grünberg, N. Rothermel, M. Werner, M. Srour, S. Abdulhussain, S. Tan, Y. Xu, H. Breitzke and G. Buntkowsky, *Solid State Nucl. Magn. Reson.*, 2013, **55–56**, 1-11.

200. M. Geppi, S. Borsacchi, G. Mollica and C. A. Veracini, *Appl. Spectrosc. Rev.*, 2008, **44**, 1.

201. W. R. Grüning, A. J. Rossini, A. Zagdoun, D. Gajan, A. Lesage, L. Emsley and C. Copéret, *PCCP*, 2013, **15**, 13270-13274.

202. T. Kobayashi, O. Lafon, A. S. L. Thankamony, I. I. Slowing, K. Kandel, D. Carnevale, V. Vitzthum, H. Vezin, J. P. Amoureux, G. Bodenhausen and M. Pruski, *PCCP*, 2013, **15**, 5553-5562.

203. E. Pump, J. Viger-Gravel, E. Abou-Hamad, M. K. Samantaray, B. Hamzaoui, A. Gurinov, D. H. Anjum, D. Gajan, A. Lesage, A. Bendjeriou-Sedjerari, L. Emsley and J.-M. Basset, *Chemical Science*, 2017, **8**, 284-290.

204. M. P. Conley, R. M. Drost, M. Baffert, D. Gajan, C. Elsevier, W. T. Franks, H. Oschkinat, L. Veyre, A. Zagdoun, A. Rossini, M. Lelli, A. Lesage, G. Casano, O. Ouari, P. Tordo, L. Emsley, C. Copéret and C. Thieuleux, *Chemistry – A European Journal*, 2013, **19**, 12234-12238.

205. T. Gutmann, J. Liu, N. Rothermel, Y. Xu, E. Jaumann, M. Werner, H. Breitzke, S. T. Sigurdsson and G. Buntkowsky, *Chemistry*, 2015, **21**, 3798-3805.

206. A. Zagdoun, A. J. Rossini, M. P. Conley, W. R. Grüning, M. Schwarzwälder, M. Lelli, W. T. Franks, H. Oschkinat, C. Copéret, L. Emsley and A. Lesage, *Angew. Chem. Int. Ed.*, 2013, **52**, 1222-1225.

207. A. R. Mouat, T. Kobayashi, M. Pruski, T. J. Marks and P. C. Stair, *The Journal of Physical Chemistry C*, 2017, **121**, 6060-6064.

208. O. Lafon, A. S. L. Thankamony, T. Kobayashi, D. Carnevale, V. Vitzthum, Slowing, II, K. Kandel, H. Vezin, J. P. Amoureux, G. Bodenhausen and M. Pruski, *Journal of Physical Chemistry C*, 2013, **117**, 1375-1382.

209. D. Lee, G. Monin, N. T. Duong, I. Z. Lopez, M. Bardet, V. Mareau, L. Gonon and G. De Paëpe, *J. Am. Chem. Soc.*, 2014, **136**, 13781-13788.

210. D. Gajan, M. Schwarzwälder, M. P. Conley, W. R. Grüning, A. J. Rossini, A. Zagdoun, M. Lelli, M. Yulikov, G. Jeschke, C. Sauvée, O. Ouari, P. Tordo, L. Veyre, A. Lesage, C. Thieuleux, L. Emsley and C. Copéret, *J. Am. Chem. Soc.*, 2013, **135**, 15459-15466.

211. A. S. Lilly Thankamony, O. Lafon, X. Lu, F. Aussenac, M. Rosay, J. Trébosc, H. Vezin and J.-P. Amoureux, *Appl. Magn. Reson.*, 2012, **43**, 237-250.

212. G. S. Foo, J. J. Lee, C.-H. Chen, S. E. Hayes, C. Sievers and C. W. Jones, *ChemSusChem*, 2017, **10**, 266-276.

213. E. Ravera, V. K. Michaelis, T.-C. Ong, E. G. Keeler, T. Martelli, M. Fragai, R. G. Griffin and C. Luchinat, *ChemPhysChem*, 2015, **16**, 2751-2754.

214. T. Kobayashi, D. Singappuli-Arachchige, Z. Wang, I. I. Slowing and M. Pruski, *PCCP*, 2017, **19**, 1781-1789.

215. J. Liu, P. B. Groszewicz, Q. Wen, A. S. L. Thankamony, B. Zhang, U. Kunz, G. Sauer, Y. Xu, T. Gutmann and G. Buntkowsky, *The Journal of Physical Chemistry C*, 2017, **121**, 17409-17416.

216. E. F. Vansant, *Journal of Liquid Chromatography & Related Technologies*, 1996, **19**, 2723-2752.

217. M. F. P. Wagner, F. Völklein, H. Reith, C. Trautmann and M. E. Toimil-Molares, *physica status solidi (a)*, 2016, **213**, 610-619.

218. K. Albert and E. Bayer, *J. Chromatogr. A*, 1991, **544**, 345-370.

219. K. Albert, R. Brindle, J. Schmid, B. Buszewski and E. Bayer, *Chromatographia*, 1994, **38**, 283-290.

220. N. Nath and A. Chilkoti, *Adv. Mater.*, 2002, **14**, 1243-1247.

221. C. G. Schäfer, M. Biesalski, G. P. Hellmann, M. Rehahn and M. Gallei, *Journal of Nanophotonics*, 2013, **7**, 070599.

222. C. Ruettiger, S. Mehlhase, S. Vowinkel, G. Cherkashinin, N. Liu, C. Dietz, R. W. Stark, M. Biesalski and M. Gallei, *Polymer*, 2016, **98**, 429-436.

223. A. Conti, G. Poggi, P. Baglioni and F. De Luca, *PCCP*, 2014, **16**, 8409-8417.

224. M. Paci, C. Federici, D. Capitani, N. Perenze and A. L. Segre, *Carbohydr. Polym.*, 1995, **26**, 289-297.

225. C. Casieri, S. Bubici, I. Viola and F. De Luca, *Solid State Nucl. Magn. Reson.*, 2004, **26**, 65-73.

226. N. koProietti, D. Capitani, E. Pedemonte, B. Blumich and A. L. Segre, *Journal of Magnetic Resonance*, 2004, **170**, 113-120.

227. B. Bluemich, S. Anferova, S. Sharma, A. L. Segre and C. Federici, *Journal of Magnetic Resonance*, 2003, **161**, 204-209.

228. I. Viola, S. Bubici, C. Casieri and F. De Luca, *Journal of Cultural Heritage*, 2004, **5**, 257-261.

229. D. Capitani, M. C. Emanuele, J. Bella, A. L. Segre, D. Attanasio, B. Focher and G. Capretti, *Tappi J.*, 1999, **82**, 117-124.

230. D. Capitani, A. L. Segre, D. Attanasio, B. Blicharska, B. Focher and G. Capretti, *Tappi J.*, 1996, **79**, 113-122.

231. P. Samyn, *J. Mater. Sci.*, 2013, **48**, 6455-6498.

232. C. J. Garvey, I. H. Parker, G. P. Simon and A. K. Whittaker, *Holzforschung*, 2006, **60**, 409-416.

233. E. L. Perkins and W. J. Batchelor, *Carbohydr. Polym.*, 2012, **87**, 361-367.

234. W. R. Gruening, A. J. Rossini, A. Zagdoun, D. Gajan, A. Lesage, L. Emsley and C. Coperet, *PCCP*, 2013, **15**, 13270-13274.

235. A. Zagdoun, G. Casano, O. Ouari, G. Lapadula, A. J. Rossini, M. Lelli, M. Baffert, D. Gajan, L. Veyre and W. E. Maas, *J. Am. Chem. Soc.*, 2012, **134**, 2284-2291.

236. A. S. L. Thankamony, C. Lion, F. Pourpoint, B. Singh, A. J. P. Linde, D. Carnevale, G. Bodenhausen, H. Vezin, O. Lafon and V. Polshettiwar, *Angew. Chem.-Int. Edit.*, 2015, **54**, 2190-2193.

237. F. Blanc, L. Sperrin, D. A. Jefferson, S. Pawsey, M. Rosay and C. P. Grey, *J. Am. Chem. Soc.*, 2013, **135**, 2975-2978.

238. F. A. Perras, U. Chaudhary, I. Slowing and M. Pruski, *Journal of Physical Chemistry C*, 2016, **120**, 11535-11544.

239. F. A. Perras, T. Kobayashi and M. Pruski, *J. Am. Chem. Soc.*, 2015, **137**, 8336-8339.

240. M. Werner, A. Heil, N. Rothermel, H. Breitzke, P. B. Groszewicz, A. S. Thankamony, T. Gutmann and G. Buntkowsky, *Solid State Nucl. Magn. Reson.*, 2015, **72**, 73-78.

241. T. Wang, Y. B. Park, M. A. Caporini, M. Rosay, L. H. Zhong, D. J. Cosgrove and M. Hong, *Proc. Natl. Acad. Sci. U. S. A.*, 2013, **110**, 16444-16449.

242. H. Takahashi, I. Ayala, M. Bardet, G. De Paepe, J. P. Simorre and S. Hediger, *J. Am. Chem. Soc.*, 2013, **135**, 5105-5110.

243. C. Ruttiger, S. Vowinkel, N. Herzog, K. Hofmann, E. Ionescu and M. Gallei, *Coatings*, 2018, **8**, 13.

244. B. M. Fung, A. K. Khitrin and K. Ermolaev, *Journal of Magnetic Resonance*, 2000, **142**, 97-101.

245. A. E. Bennett, C. M. Rienstra, M. Auger, K. V. Lakshmi and R. G. Griffin, *J. Chem. Phys.*, 1995, **103**, 6951-6958.

246. A. B. Mabrouk, M. C. B. Salon, A. Magnin, M. N. Belgacem and S. Boufi, *Colloids and Surfaces A: Physicochemical and Engineering Aspects*, 2014, **448**, 1-8.

List of Abbreviations

AFM	Atomic Force Microscopy
AMUPol	Water soluble nitroxyl based biradical developed
ATRP	Atom Transfer Radical Polymerization
BET	Brunauer−Emmett−Teller
BJH	Barrett, Joyner, and Halenda
bTbK	bis-TEMPO-bis-ketal
CE	Cross Effect
CIDNP	Chemically Induced Dynamic Nuclear Polarization
CPMAS	Cross Polarisation Magic Angle Spinning
d-DNP	Dissolution-DNP
DNP	Dynamic Nuclear Polarisation
DQ	Double Quantum
FSLG	Frequency Switched Lee Goldgerg
HETCOR	Heteronuclear Correlation
MD	Molecular Dynamics
MAS	Magic-Angle Spinning
MRI	Magnetic Resonance Imaging
OE	Overhauser Effect
PBEMA	Poly Benzyl Methacrylate
PET	PolyEthylene Terephthalate
PHIP	Para-hydrogen induced polarization
SE	Solid Effect
SEM	Scanning Electron Microscopy
SEOP	Spin Exchange Optical Pumping
SNR	Signal to Ratio
SQ	Single Quantum
TCE	Tetrachloroethane
TEKPol	TCE soluble biradical
TM	ThermalMixing
TOTAPOL	1-(TEMPO-4-oxyl)-3-(TEMPO-4-amino)-propan-2-ol
TPPM	Two-pulse phase-modulated
TSP	Trimethylsilylpropanoic acid
ZQ	Zero Quantum

List of Publications

1. B. Kumari, M. Brodrecht, T. Gutmann, H. Breitzke and G. Buntkowsky, The Journal of Applied Magnetic Resonance, **2019**, APMR-D-19-00062R1 (just accpted)

2. T. Gutmann, B. Kumari, L. Zhao, H. Breitzke, S. Schöttner, C. Rüttiger and M. Gallei, *The Journal of Physical Chemistry C*, 2017, **121**, 3896-3903.

3. M. Brodrecht, B. Kumari, H. Breitzke, T. Gutmann and G. Buntkowsky, *Journal*, **2018**, 232, 1127.

4. B. Kumari, M. Brodrecht, H. Breitzke, M. Werner, B. Grünberg, H.-H. Limbach, S. Forg, E. P. Sanjon, B. Drossel, T. Gutmann and G. Buntkowsky, *The Journal of Physical Chemistry C*, 2018, **122**, 19540-19550.

5. B. Kumari, D. John, P. Hoffmann, A. Spende, E. Toimil-Molares Maria, C. Trautmann, C. Hess, P. Ruff, M. Schulze, R. Stark, G. Buntkowsky, A. Andrieu-Brunsen and T. Gutmann, *Journal*, **2018**, 232, 1173.

6. M. Brodrecht, B. Kumari, A. S. S. L. Thankamony, H. Breitzke, T. Gutmann and G. Buntkowsky, *Chemistry – A European Journal*, 2019, **25**, 5214-5221.

Curriculum Vitae

Personal Information

Name	: Bharti Kumari
Place of Birth	: Agra, Uttar Pradesh, India
Date of Birth	: 14 Nov 1993
Nationality	: Indian

Education

May 2016- Present	: Dr. rer. nat. Department of chemistry Technische Universität Darmstadt, Germany
June 2015-Feb 2016	: Project Assistant TIFR centre for Interdisciplinary Science (TCIS) Mumbai-Hyderabad, India
Aug 2010-May 2015	: BS-MS dual degree Indian Institute of Science Education and Research (IISER) Mohali, India
Jul 2007-May 2009	: Intermediate in Science Agra, India
Aug 2006-May 2007	: High-School Agra, India

Darmstadt,

Erklärung

Ich erklare hiermit, dass ich meine Dissertation selbststandig und nur mit den angegebenen Hilfsmitteln angefertigt und noch keinen Promotionsversuch unternommen habe.

_____

Bharti Kumari

Darmstadt,

Erklärung

Ich erklare hiermit, dass die elektronische Version der Doktorarbeit mit der schriftlichen Version ubereinstimmt. Die elektronische Version liegt dem Prufungssekretariat vor.

_____

Bharti Kumari